Finite-element modelling of the human middle ear based on X-ray micro-computed tomography and Doppler optical coherence tomography in the same ear

Xuan Wang

Department of BioMedical Engineering

McGill University, Montréal

April 2019

A thesis submitted to McGill University

in partial fulfillment of the requirements of the degree of

Master of Engineering

Finite-element modelling of the human middle ear based on X-ray micro-computed tomography and Doppler optical coherence tomography in the same ear

Abstract

The middle ear plays a critical role in transferring sound into the inner ear. The vibration patterns of the tympanic membrane (TM) and ossicles have been investigated by many groups but, particularly at high frequencies, are still not well understood. Computational modelling of the middle ear offers a pathway toward a better understanding of the mechanical function of these structures. The tuning and validation of such models require accurate anatomical and mechanical experimental data, but such data usually come from populations of ears and little is known about how differences in individual anatomy and material properties affect middle-ear function. In this study we created a finite-element (FE) numerical model of a middle ear and validated it against vibration measurements from the same ear.

A real-time phase-sensitive Doppler optical coherence tomography (OCT) system was used to measure the vibrations of both the TM and the ossicles of a human temporal bone at a stimulation frequency of 500 Hz. The measured vibration pattern of the TM showed a maximal displacement in the posterior region and a smaller maximum in the anterior region. The experimental data also showed smaller displacements on the ossicles, while the cochlear promontory appeared immobile as expected.

A 3-D X-ray micro-computed tomography (microCT) scan was acquired for the same ear. A FE model of the middle ear was built using a combination of locally developed and other free and open-source software. The geometry was based on semi-automatic segmentation of the microCT images, and material properties were based on previous studies. A sensitivity analysis was performed to analyze the relative importance of the various parameters. The Doppler OCT images, masked by B-mode OCT images to reduce noise, were also segmented and the resulting 3-D model was transformed to Cartesian coordinates and aligned with the microCT-based model.

Two FE solvers (Code_Aster and SAP IV) were used as part of the verification process. The simulated vibration patterns from the different solvers were compared with the measured Doppler-mode OCT velocity data and with data from the literature. The simulation results match well with the shape of the measured vibration pattern of the TM at 500 Hz.

Co-registration of OCT and microCT for individual ears is a viable approach for building and validating FE models. If extended to clinical CT scans, this process could lead to patient-specific models and improved diagnosis of pathological changes in the middle ear. The process of creating FE models for the middle ear would need to be streamlined for clinical applications.

Modélisation par éléments finis de l'oreille moyenne humaine basée sur la tomographie par micro-tomodensitométrique et la tomographie par cohérence optique Doppler dans la même oreille

Résumé

L'oreille moyenne joue un rôle crucial dans le transfert du son dans l'oreille interne. Les schémas de vibration du tympan (membrane tympanique, MT) et des osselets ont été étudiés par de nombreux groupes mais, en particulier aux hautes fréquences, ils ne sont toujours pas bien compris. La modélisation numérique du MT et de l'oreille moyenne ouvre la voie à une meilleure compréhension de la fonction mécanique de ces structures, mais le réglage et la validation de tels modèles nécessitent des données expérimentales anatomiques et mécaniques précises. Ces données proviennent généralement des populations d'oreilles et on connaît mal la manière dont les différences individuelles d'anatomie et de propriétés matérielles affectent la fonction du MT et de l'oreille moyenne. Dans cette étude on a créé un modèle numérique par la méthode des éléments finis (EF) et l'a validé contre les mesures de vibration dans la même oreille.

Un système de tomographie par cohérence optique (OCT) Doppler sensible à la phase en temps réel a été utilisé dans cette étude pour mesurer les vibrations du MT et des osselets dans un os temporal humain à une fréquence de stimulation de 500 Hz. Le schéma de vibration mesuré du MT à 500 Hz montre un déplacement maximal dans la région postérieur et un plus petit maximum dans la région

antérieur. Les données expérimentales montrent également de plus petits déplacements sur les osselets, et le promontoire cochléaire apparaît immobile comme attendu.

Un scan 3-D micro-tomodensitométrique (microCT) a été réalisé pour la même oreille. Un modèle EF de l'oreille moyenne a été construit à l'aide d'une combinaison de logiciels développés localement et d'autres logiciels libres et open-source. La géométrie était basée sur une segmentation semi-automatique des images microCT et les propriétés des matériaux étaient basées sur des études précédentes. Une analyse de sensibilité a été réalisée pour analyser l'importance relative des différents paramètres. Les images OCT Doppler, masquées par les images OCT en mode luminosité ('brightness', mode B) pour réduire le bruit, ont également été segmentées et le modèle 3-D résultant a été transformé en coordonnées cartésiennes et aligné avec le modèle à base de microCT.

Deux solveurs EF (Code_Aster et SAP IV) ont été utilisés dans cette étude dans le cadre du processus de vérification. Les résultats pour les vibrations simulés des différents solveurs ont été comparés aux données de vélocité mesurées par OCT en mode Doppler et aux données des études précédentes.

Les résultats de la simulation correspondent bien à la forme du patron de vibration mesuré du TM à 500 Hz.

La mise en correspondence des images OCT et microCT pour les oreilles individuelles est une approche viable pour la construction et la validation des modèles de EF. Si elle était adaptée aux scans CT cliniques, ce processus pourrait conduire à des modèles spécifiques au patient et à un meilleur diagnostic des changements pathologiques dans l'oreille moyenne. Le processus de création de modèles EF pour l'oreille moyenne devrait être simplifié pour les applications cliniques.

Acknowledgements

When looking back on my master's study, I have to say that without the help, support and encouragement from several people I would never have been able to finish this work.

I would like to express my deep appreciation and sincere gratitude to my supervisor Dr. W. Robert J. Funnell for accepting me into his group and his guidance throughout the years of my master's. His broad knowledge and logical way of thinking have made this thesis possible. I appreciate his trust and fairness, and his understanding and unfailing support to me when there were some emergency circumstances in my family. I deeply appreciate his willingness and effort to review multiple drafts of this manuscript at short notice and late hours.

I must also acknowledge Dr. Robert Adamson of Dalhousie University, Halifax, for providing the data used in this study. Also, I would like to thank him for his generosity in giving me the opportunity of visiting his SSENCE lab and doing data acquisition using the Doppler OCT system built by his lab. His comments and valuable feedback on my work were of great assistance when analyzing my results. I also want to thank the other researchers in the SSENCE laboratory. Thanks go to Dan McDougall for his kindness in sharing his knowledge in Doppler OCT data processing and setting up the Doppler OCT system during the data acquisition; to Thomas Landry for his careful guidance in cadaver bone preparation and experimental set up; and to Josh Farrell for explaining the right data format to be able to display the middle-ear vibrometry using CUDA.

I want to acknowledge Sahar, the previous master's student in our lab, for her kindness in providing constructive advice and help on solving the challenges in my work; she was always there to help. I also thank Orhun and Majid for their help in explaining some concepts to me and for other valuable input.

I am deeply indebted to my parents Qing and Yuerong, who always enabled me to withstand challenges and back me up both at work and in life. I dedicate my work to them.

My sincere thanks also go to Pina Sorrini, Daniel Caron, and Trang Q. Tran. Their guidance and support during my studies have been precious.

My gratitude also goes to all those others who, formally and informally, gave me the benefit of their knowledge, views, and experience. A few lines are too short to make a complete account of my sincere appreciation for the people who helped me. Thanks!

Financial aid has been provided in part by the Canadian Institutes of Health Research, the Natural Sciences and Engineering Council of Canada and the BioMedical Engineering Department.

Table of Contents

Chapter 1
Introduction

1.1 Motivation

The middle ear plays a critical role in transferring sound into the inner ear through vibrations of the tympanic membrane (TM) and ossicles. The vibration patterns of the TM and ossicles have been investigated by many groups but, particularly at high frequencies, are still not well understood. Computational modelling of the middle ear offers a pathway toward a better understanding of the mechanical function of these structures, and potentially may help in diagnosis. The tuning and validation of such models require accurate anatomical and experimental mechanical data, but such data usually come from populations of ears and little is known about how differences in individual anatomy and material properties affect middle-ear function. Therefore, it is a useful first step to create a numerical model, such as a finite-element (FE) model, of a middle ear and to validate it against vibration measurements from the same ear. High-resolution imaging techniques provide virtual slices of middle-ear structures, and these images can be used as input to FE modelling software. Doppler optical coherence tomography (OCT) is a new imaging tool based on low-coherence interferometry. It is useful for the spatially resolved measurement of middle-ear shape and vibrations. It is also capable of providing real-time in-vivo measurements for clinical use. X-ray micro-computed tomography (microCT) provides higher resolution (micrometer range) imaging which can be used to segment the middle-ear structures and do 3-D model building.

1.2 Objectives

The goal of this research was to simulate human middle-ear mechanics taking advantage of OCT experimental shape and vibration measurements together with microCT imaging of the same ear. The specific objectives were to build a FE model based on the microCT images, to adopt material properties from the literature, to run simulations for a sound stimulus at 500 Hz, and to validate the model performance againts the OCT vibration measurement. A secondary objective was to examine the effects of the material properties of each structure through sensitivity analysis, to provide a better understanding of the importance of those values in building the model. An additional objective was to reconstruct the shape of the TM from the OCT images and compare it with the shape derived from microCT.

1.3 Thesis outline

Chapter 2 of the thesis is a basic overview of the auditory system with emphasis on the anatomy of the middle ear. Chapter 3 reviews the mechanics of the human middle ear, previous numerical modelling studies, and experimental measurements of middle-ear vibration patterns. Chapter 4 presents the history of FE modelling, and describes the building of FE models and the FE modelling software used in this thesis. The methods are presented in Chapter 5, followed by the model definition and verification in chapter 6. Chapter 7 presents the results. A summary of our findings, a discussion of potential future work and the significance of our research are presented in Chapter 8.

Chapter 2

Human ear anatomy

2.1 Introduction

The human ear consists of three parts – outer ear, middle ear and inner ear (Fig. 2-1). The external ear comprises the pinna and the external auditory canal. The outer ear is separated by the tympanic membrane (TM, also known as the eardrum) from the middle-ear cavity. The chain of small bones (ossicles) in the middle ear conducts the sound from the TM to the cochlea in the inner ear. The inner ear consists of two parts: the cochlea, which transforms acoustical energy to neural signals, and the vestibular system. Detailed descriptions of the anatomy of the human ear can be found in standard

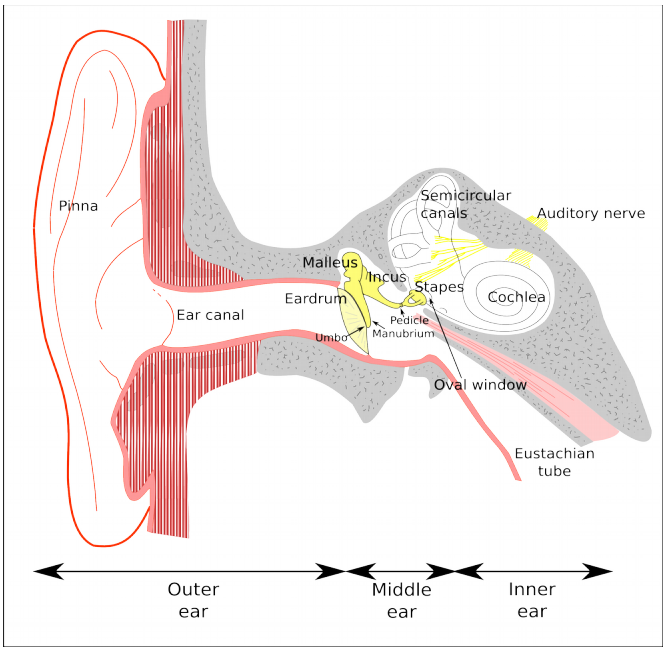

Fig. 2-1: Schematic diagram of the human ear, including the outer, middle and inner ear. (Adapted from Cull,1989)

anatomy textbooks (e.g., Standring and Gray, 2008). In this chapter we include further descriptions of the parts of the human middle ear only, since it is the main focus of this thesis.

The middle ear is an air-filled chamber housing the TM, three ossicles (malleus, incus and stapes in that order) and their suspensory attachments. The stapes is connected to the oval window of the cochlea. The middle-ear air cavity is connected to the back of the nasopharynx by the Eustachian tube, which equalizes the pressures on the two sides of the TM.

2.2 Tympanic membrane

2.2.1 Shape

The TM is divided into a small superior portion, the pars flaccida (PF), and the larger pars tensa (PT) which amounts to about 90% of the TM (Fig. 2-2). The PT is thinner and stiffer than the PF, and it has a roughly conical shape pointing inward, with the deepest part being called the umbo. The TM is coupled to the lateral surface of the manubrium ('handle') of the malleus by soft tissue, as described in Section 2.5. The TM is often described as having four quadrants: posterior-superior, posterior-inferior, anterior-inferior and anterior-superior. These four quadrants are defined by drawing an imaginary straight line

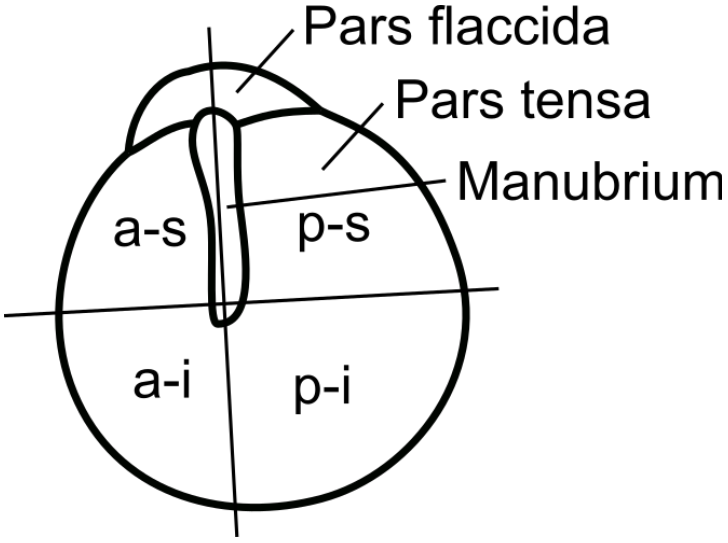

Fig. 2-2: Lateral view of TM. The TM is composed of two regions: the pars flaccida and pars tensa. The TM is often described as having four quadrants: posterior-superior (p-s), posterior-inferior (p-i), anterior-inferior (a-i) and anterior-superior(a-s). These four quadrants are defined by drawing an imaginary straight line along the manubrium of the malleus, and a second line going through the umbo perpendicular to the first line.

along the manubrium, and a second line going through the umbo perpendicular to the first line (Fig. 2-2). The periphery of the TM is surrounded by a bony ring called the tympanic annulus. A thickened fibrocartilaginous ring connects the TM to the tympanic annulus.

The TM has a roughly conical shape, with an apex angle of approximately 120^{o} (Fumagalli, 1949). Following early studies measuring the conical shape in different mammalian species (e.g. Kojo, 1954; Kirikae, 1960), Khanna and Tonndorf (1975) introduced shadow-moiré topography to study the three-dimensional shape of the cat TM. Dirckx & Decraemer (1989, 1997) introduced an improved phase-shift moiré technique for precise full-field shape measurements of the TM. This imaging technique utilizes a grating image which is projected onto the TM and modulated by the TM topography; the resulting moiré interference results in a pattern of moiré fringes. The fringe shifts can be used to calculate a shape matrix with the column and row numbers proportional to the *x* and *y* coordinates. The shape map is displayed with a grey scale proportional to depth (Fig. 2-3).

MicroCT and magnetic-resonance (MR) microscopy techniques have also been used in measuring the 3-D shape of the TM. MicroCT allows scanning of the entire TM as well as the temporal bone at the same time. The boundary of the TM can be determined by pressurizing the TM (Decraemer & Funnell, 2008). However, this method requires a longer measuring and post-processing time than the moiré method. Thus it is not appropriate for real-time applications. MR imaging provides better contrast for soft tissues but it generally has lower resolution than microCT and it provides no contrast between bone and air (Decraemer & Funnell, 2008).

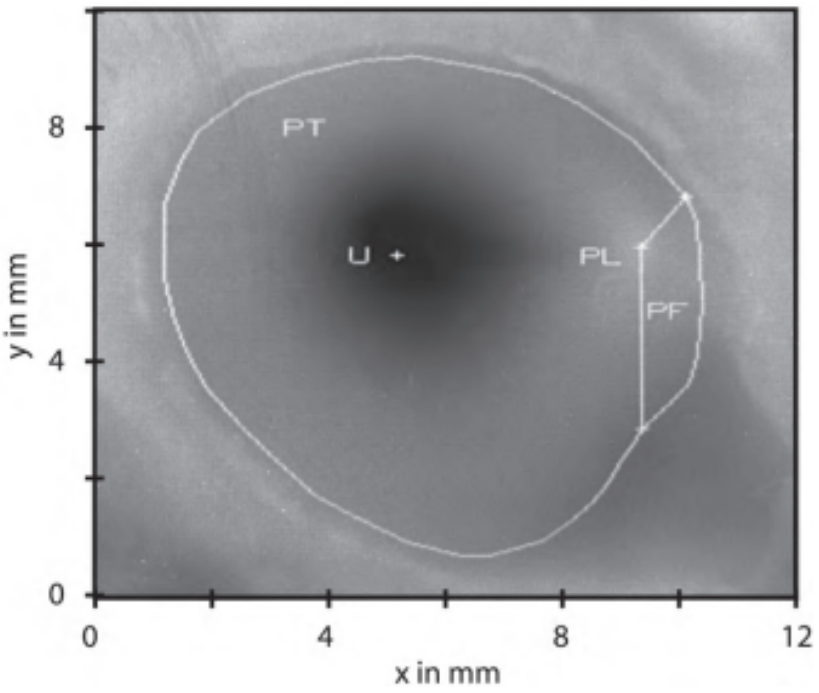

Fig. 2-3: A grey-level shape image of a human TM, obtained by attributing to each pixel with coordinates (x,y) a grey level proportional to the local depth z(x,y). (Decraemer & Funnell, 2008)

As with the shape and the curvature, the TM thickness shows considerable inter-specimen variability but in general the thinnest part is in the central region between the umbo and the annular ring, and the thickness increases steeply over a small distance when moving from the central region either toward the peripheral rim of the PT or toward the manubrium. Kojo (1954) reported that the thickness ranges from 30 to 120 μm, with mean values from 55 to 90 μm. Lim (1970) reported that the thickness of the TM varies from 30 to 90 μm.

Kuypers et al. (2006) used confocal laser microscopy to measure the thickness distribution of the TM. Measurements were performed on fresh TMs to avoid shrinkage and damage of the sample. The thickness was measured along a set of lines crossing the membrane. The values could be interpolated between the lines and thickness distribution maps could be generated (Fig. 2-4). Although the relative

thickness variations were quite similar for all three samples, large variations of the thickness values were found among the three specimens they studied, with mean thickness values of 120, 50 and 40 μm, respectively. They also found large variations in TM thickness values found in the literature.

Van der Jeught et al. (2013) studied five normal TMs and one pathological TM with optical coherence tomography (OCT). They reported that the mean thickness values across the PT ranged between 79 and 97 μm. The thinnest central region between umbo and annular ring was around 50–70 μm, with the thickness increasing to approximately 100–120 μm around the manubrium. They also observed a "local thickening in the antero–inferior quadrant region, and a strong linear correlation between inferior–posterior length and mean thickness of the TM".

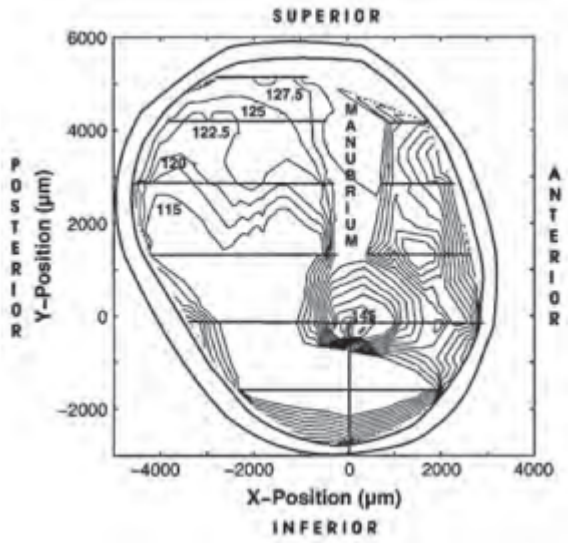

Fig. 2-4: Contour plot of the thickness distribution of an entire human left TM. Contours are shown for thicknesses between 115 and 145 μm, with a step of 2.5 μm. The positions of the scanning lines and the positions of the manubrium and annulus are indicated. (Kuypers et al., 2005).

2.2.2 Microscopic structure

The TM is composed of three layers: an outer epidermal layer; the lamina propria; and an inner mucosal layer. The epidermis is continuous with the epidermis of the external ear canal. It grows and migrates outward from the centre of the TM toward the cartilaginous part of the ear canal. This

function contributes to the self-cleaning ability of the ear canal (e.g. Magnoni, 1938; Funnell & Laszlo, 1978). The mucosal layer of the TM is a continuation of the mucosal lining of the middle-ear cavity.

The main structural component of the TM is the lamina propria. The lamina propria represents the main difference between the PT and the PF. It has four distinct parts in the PT: subepidermal connective tissue, radial fibres, circular fibres, and submucosal connective tissue. Collagen types II and IV are the major constituents of the fibres in the fibrous layer of the PT. The radial fibres generally run more or less straight from the manubrium to the annular ligament. The fibres become more closely packed as they converge on the manubrium. The circular fibres start from the manubrium, curve around below the umbo, and insert again on the opposite side of the manubrium. In the PF, the lamina propria consists mostly of loose connective tissue with elastin and collagen fibres.

2.3 Ossicles

The ossicles include the three smallest bones of the human body. The first ossicle is the malleus (Latin for “hammer”, because of its shape). It is composed of a head, neck, lateral (or short) process, anterior process and manubrium (Fig. 2-5). The head of the malleus is connected to the body of the incus by the incudomallear joint. The lateral face of the manubrium of the malleus is attached to the medial surface of the TM by soft tissue along the entire length of the manubrium. This soft-tissue connection will be discussed in more detail in Section 2.5.

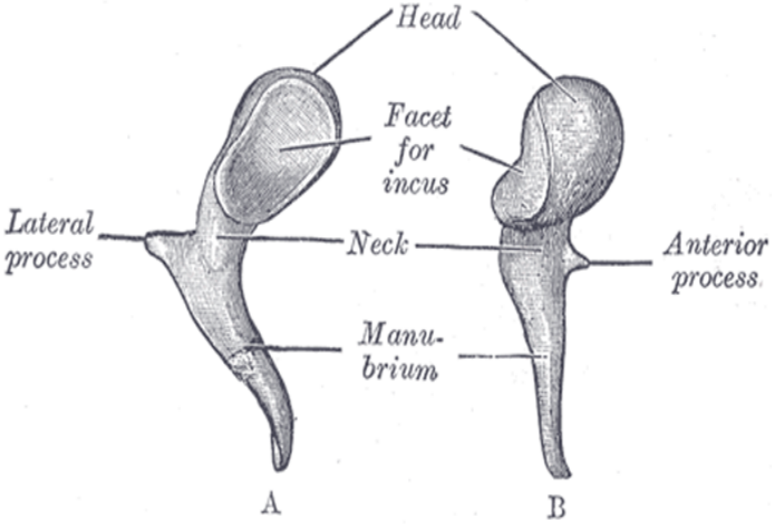

Fig. 2-5: Left malleus. A. Posterior view. B. Medial view. (Gray's Anatomy (1918), from http://www.bartleby.com/107/)

The incus (Latin for "anvil", because of its relationship to the malleus) lies between the malleus and the stapes. It is composed of a body, short process, long process (or "crus") and lenticular process (Fig 2-6). The body forms a joint with the head of the malleus. The long process ends in the lenticular process, which is composed of a very thin pedicle and the lenticular plate (Funnell et al., 2005). The medial face of the lenticular process forms the incudostapedial joint with the head of the stapes. The short process is attached to the wall of the middle-ear air cavity by the posterior incudal ligament.

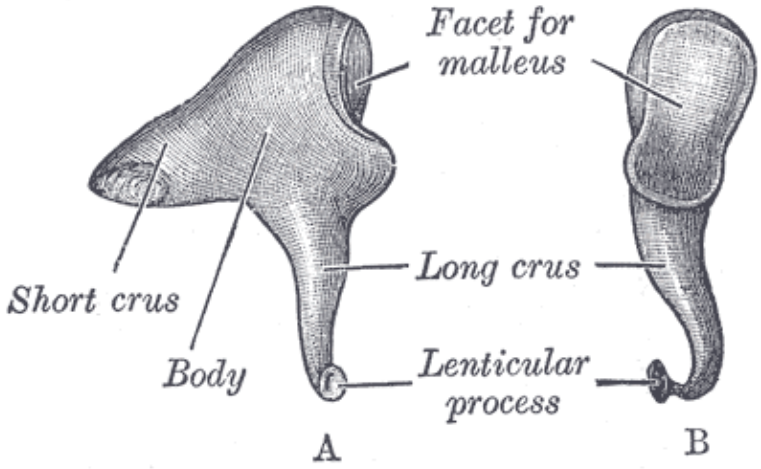

Fig. 2-6: Left Incus. A. Medial view. B. Anterior view. (Gray's Anatomy (1918), from http://www.bartleby.com/107)

The stapes (Latin for "stirrup", for its shape) has a head, a neck, two branches known as the anterior and posterior crura, and a footplate. The stapes footplate fits in the oval window, an opening in the wall of the bony labyrinth of the inner ear, and is held in place by the annular ligament (Fig. 2-7).

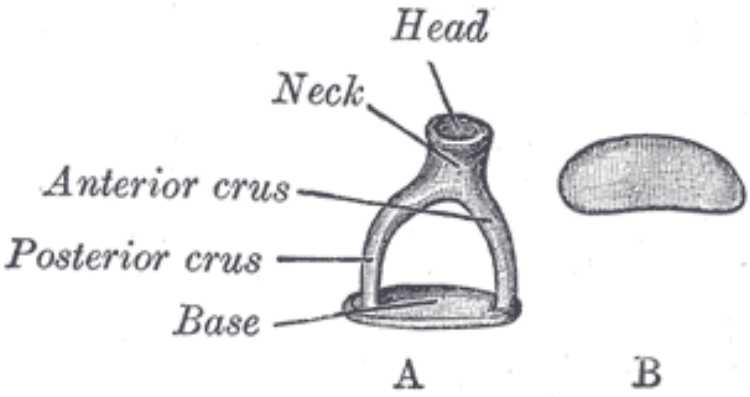

Fig. 2-7: Frontal view of stapes (A), and view from below (B). (Gary's anatomy (1918), from http://www.bartleby.com/107/)

2.4.1 Ossicular ligaments

The ossicles are held in place in the middle-ear cavity by suspensory ligaments. The anterior mallear ligament (AML) extends from the head of the malleus to the anterior epitympanic wall. The lateral

mallear ligament (LML) fans out laterally from the neck of the malleus to the bony rim of the notch of Rivinus. The incus is attached to the tympanic cavity wall by the posterior and superior ligaments (Fig. 2-8). There is some controversy about the existence of some of these ligaments and whether they make any significant mechanical contribution (Mikhael, 2005; Rosowski, 2010).

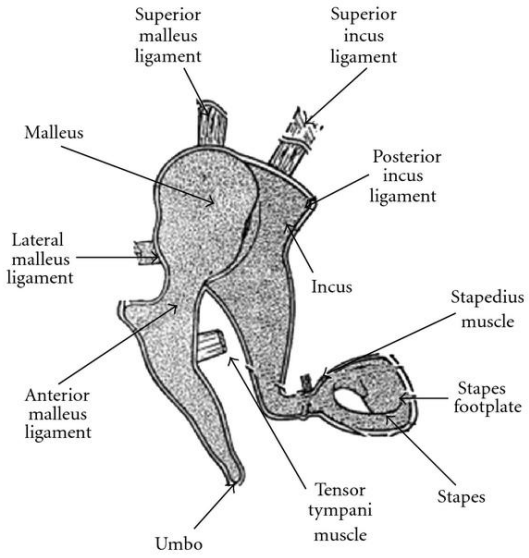

Fig. 2-8: Sketch of the middle-ear structures with the ligaments and the muscle tendons (Ferris & Prendergast, 2000)

2.4.2 Ossicular muscles and tendons

The movement of the ossicles is influenced by two striated skeletal muscles in the middle-ear cavity: the stapedius muscle, innervated by the VIIth (facial) nerve, and the tensor tympani muscle, innervated by the Vth (trigeminal) nerve. Moderate to loud sounds of 60–100 dB sound pressure level (SPL) in conscious humans (Feeney & Keefe, 1999) produce reflex contractions of the stapedius muscle that lead to increases in the impedance of the annular ligament (Pang & Peake, 1986) and decreases in middle-ear sound transmission (Møller, 1974). Louder sounds can also generate reflex contractions of the tensor tympani muscle (Rosowski, 2010).

These two muscles control the ossicles independently (Møller, 1974). For example, slippage in the incudostapedial joint allows contractions of the stapedius muscle to cause changes in the position of the stapes head by several hundred micrometers (Pang & Peake, 1986) without generating large movements of the incus. Similarly, the incudomallear joint allows the tensor tympani muscle to cause TM movement by 100–500 μm without generating similar motions of the stapes (e.g. Marquet, 1981). The contractions of these muscles are also associated with body motion (Carmel & Starr, 1963), vocalization (Borg & Zakrisson, 1975) and chewing (Djupesland, 1965). Contraction of the muscles reduces low-frequency sound transmission through the middle ear (e.g. Irvine, 1976; Pang & Guinan, 1997).

2.5 Attachment between tympanic membrane and malleus

The TM and malleus are connected by soft tissue that extends along the entire length of the manubrium, as described in detail by Graham et al. (1978). The nature of this TM–malleus connection (TMMC) varies along the manubrium and can be divided into three regions: the region around the umbo, the mid-manubrium region, and the upper third of the manubrium below the lateral process. The TMMC is composed of three layers: a fibrous layer covering the manubrium; a fine layer of mucosa medially; and an epithelial layer laterally (Fig. 2-9). The connection in the umbo region is the strongest. It gradually gets thinner and longer, becoming a mere “stalk” in the third region. The connection becomes tight and fibrous again at the lateral process (Graham et al., 1978). The width and thickness of the TMMC vary among individuals by almost an order of magnitude (De Greef et al., 2016).

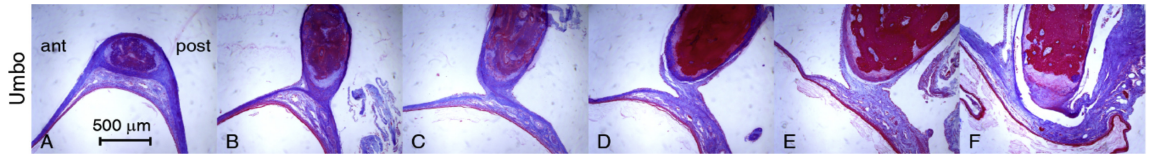

Fig. 2-9: Attachment between manubrium and TM. A-F are transverse histological sections at different positions along the manubrium, from the umbo region (A) to the lateral process (F). (De Greef et al., 2016)

2.6 Incudomallear joint and incudostapedial joint

The incudomallear joint (IMJ) and incudostapedial joint (ISJ) are synovial joints. The IMJ is "saddle-shaped"; the articular surfaces are "covered with articular cartilage, and each joint is enveloped by "a capsule rich in elastic tissue and lined by synovial membrane" (Standring and Gray, 2008).

A more detailed description of the IMJ is omitted here since it is not included in our finite-element model. Previous studies usually considered that at low frequencies the malleus and incus move as a single body (e.g., Kirikae, 1960), and the IMJ is often omitted from both circuit and finite-element models as a first approximation (Funnell et al., 2013).

On the other hand, the ISJ represents the place where the rotational motions of the malleus and incus are converted into the translational motion of the stapes, so it is important to include it in the modelling, since a rigid connection "would cause a very unphysiological constraint" (Funnell et al., 2013).

As described by Karmody et al. (2009), the capsule of the ISJ complex is attached to the full length of the lenticular process. The plate of the lenticular process forms a convex shape perpendicular to the pedicle. It is a thin layer of bone with calcified and uncalcified layers of cartilage that extend to its articular surface. The other side of the articulating surface, on the head of the stapes, is concave to fit the convex lenticular plate (Fig. 2-10). Karmody et al. (2009) concluded that the synovial joint space is unequally divided into two chambers (lateral (incudal) and medial (stapedial)) by a fibrocartilaginous

articular disk (meniscus). The capsule of this joint is mostly composed of elastic fibres (Kawase et al., 2012) and encloses the synovial fluid.

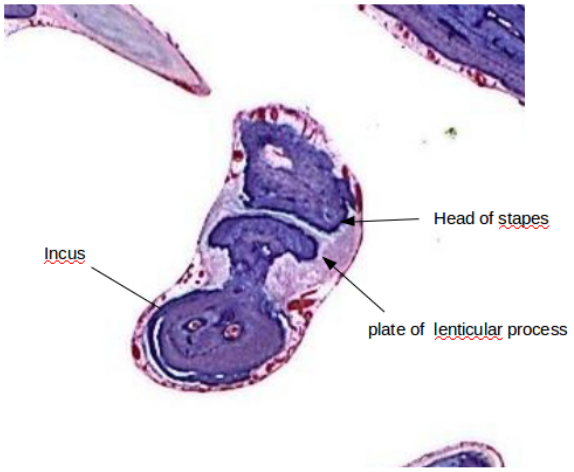

Fig. 2-10: Histological section through the ISJ complex demonstrates the stem (pedicle) and cap (plate) of the lenticular process, and the head of the stapes (courtesy: C. Northrop).

Chapter 3

Mechanics of the human middle ear

3.1 Introduction

In this Chapter we introduce the mechanics of the human middle ear, with Section 3.2 first introducing the mechanism by which the middle ear matches the low and high impedances of the media in the outer ear and the inner ear. Many modelling studies have investigated the vibrations of the tympanic membrane and ossicles in humans, and the simulation results can be validated with experimental data. Section 3.3 reviews previous experimental results on middle-ear vibration patterns, and then Section 3.4 reviews previous FE models of the human middle ear.

3.2 Impedance-matching mechanism

The middle ear transmits vibrations from the TM through the ossicles to the cochlea. The design of the three-bone ossicular chain, with flexible joints between the ossicles, can be considered as one of the defining characteristics of the mammalian middle ear, in contrast to non-mammalian species (Saunders & Johnstone, 1972). One advantage of the design of the typical mammalian middle ear is that the ossicles can be considered to form a lever system which enhances the efficiency of the sound transmission.

The sound is transmitted from the air-filled outer ear to the liquid-filled cochlea. Acoustical impedance (Z), which is defined as the ratio of acoustical pressure P to acoustical volume flow U, can be used to calculate the acoustical transmission and reflection at the boundary between two materials with different acoustical impedances. The acoustical impedance is much greater in a liquid (as in the inner ear) than in air (as in the outer ear). When sound waves travel from a lower-impedance medium to a

much higher-impedance medium, much of the sound energy is reflected. A major function of the middle ear is to match the low-impedance air in the external ear to the high-impedance liquid in the cochlea. The impedance transformation mechanism is often described in terms of three mechanisms: (1) an area ratio, (2) a mechanical lever ratio and (3) membrane curvature. The following paragraphs briefly introduce the concept of each mechanism.

The middle-ear transformer ratio is largely produced by the area ratio between the TM and the stapes footplate. The effective surface area of the TM is much larger than that of the footplate. After transformation, the pressure of the sound waves increases in proportion to the ratio of the two areas. The eardrum area which is directly involved in forming a link between the outer and middle ears (the effective area) is often taken to be about 2/3 of its total area, or about 55 mm^2, while the effective area of the stapes footplate, if moving in a piston-like fashion, is approximately 3.2 mm^2 (von Békésy, 1960, p. 102). This means that the pressure at the stapes footplate is about 17 times that at the eardrum.

A force exerted on the umbo is transferred to the stapes through a mechanical lever system. The lever arms comprise the manubrium of the malleus and the long crus of the incus. The manubrium can be considered as the force arm, spanning the perpendicular distance between the umbo and the rotation axis, and the incudal long crus can be seen as the resistance arm, spanning the perpendicular distance between the tip of the crus and the rotation axis (Fig. 3-1). The lever action is caused by the fact that the lever arm of the incus is shorter than the manubrial lever arm. The ratio of the two is reported to be from 0.50 to 0.77 (Guinan & Peake, 1967; Yost & Nielsen, 1977; as cited by Ghosh, 1996).

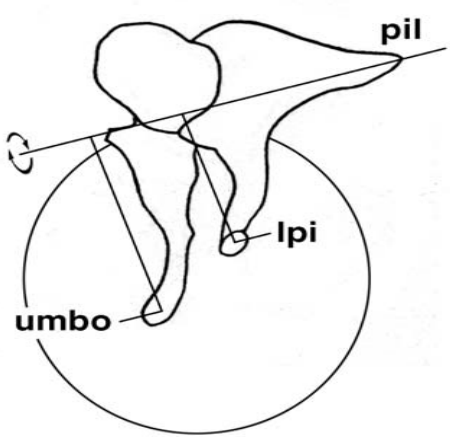

Fig. 3-1: Rotation axis and lever arms of the ossicular lever: The axis goes through the posterior incudal ligament and the anterior mallear process (Adapted from: Dahmann, 1930).

Helmholtz (1895) suggested that the eardrum's curvature was one of the causes of the transformer ratio of the middle ear. "The curved resting shape of the [TM], in the absence of any acoustical stimulus, was assumed [by Helmoltz] to be determined by the tension resulting from forces applied to it by the distributed coupling of the TM to the manubrium" (Funnell, 1996). Based on modelling, Funnell (1996) found that "certain regions of the TM are more effective in driving the manubrium than can be explained on the basis of their distance from the axis of rotation". This phenomenon was found to depend on the curvature of the eardrum, but was not related to tension or anisotropy of the TM as Helmholtz proposed.

Although various studies have investigated the effects of the three mechanisms, it is difficult to meaningfully separate the force-transformation behaviour into these distinct lever mechanisms. They are all involved in determining the overall transformation from pressure to force. The effective surface area of the TM and the curvature-related lever mechanism "both depend on the geometry and material properties of the [TM] in interrelated ways", and the lever-arm mechanism depends on the nature of the

distributed coupling of the TM to the manubrium" (Funnell, 1996). It is therefore difficult to evaluate separately how much each mechanism contributes, especially at higher frequencies where the motions of the middle ear are more complicated.

3.3 Experimental observations of middle-ear vibrations

3.3.1 Vibration patterns of theTM

The vibration patterns of the TM are highly frequency dependent. At frequencies below 2 kHz, the motion of the TM assumes simple mode shapes (e.g., Tonndorf & Khanna, 1972). At higher frequencies the motion of the TM becomes more complex, showing many peaks and valleys above 4 kHz, and the movement of the umbo is drastically reduced (e.g., Volandri et al., 2011).

Many studies have been carried out focusing on measurements of human TM vibrations. Early measurements of vibrations of the TM were reviewed by Funnell and Laszlo (1982). This section presents only a few key studies that were mentioned in that article and then reviews measurements that were done more recently. Detailed reviews of the studies were made by Volandri et al. (2011) and Maftoon (2014).

Von Békésy (1960, p. 101) used a capacitive probe to measure vibrations of the human TM and concluded that the central part of the TM vibrates with almost no bending in the direction perpendicular to the manubrium. He also claimed that the maximum vibration magnitude occurs inferior to the manubrium at low frequencies (up to 2 kHz). At higher frequencies, "the conical portion of the eardrum loses its stiffness" and "the manubrium lags behind the pars tensa portions adjacent to the manubrium above 2.4 kHz". Von Békésy's results are contradicted by more recent studies. Some possible reasons for the discrepancy were summarized by Funnell and Laszlo (1982).

Time-averaged laser holography has been used to measure the vibration of the human TM (e.g., Tonndorf & Khanna, 1972). This method gave iso-amplitude contours on the vibrating TM. They found that the TM did not move as a stiff surface at lower frequencies (e.g., 525 and 600 Hz). The posterior and anterior regions were the two areas on the TM with higher magnitudes of displacement, with the posterior side having the highest magnitudes. The different parts of the TM moved in phase until about 2 kHz. When the frequency rose above 3 kHz, the pattern became more complex. Fritze et al. (1979) also used holography to study vibration patterns of the human TM. Von Bally (1982) developed a fibre endoscope with double-pulsed laser holography to study the human TM *in vivo*. Løkberg et al. (1979, 1980) used time-averaged electronic speckle pattern interferometry with phase modulation *in vivo*. The later studies showed good agreement with the results from Tondorf & Khanna (1972).

Point-by point laser Doppler vibrometry (LDV) provides more precise vibration measurements and better frequency resolution than holographic methods. Decraemer et al. (1989) used a homodyne laser interferometer on the cat PT and manubrium, with reflective objects to increase the signal to noise ratio. Decraemer et al. (1999) improved the laser interferometer so it had higher sensitivity and so that the measurement could be done without reflective objects. They concluded that the TM motion "looks more like a travelling wave than like a standing wave" at 5 kHz.

Taking advantage of recent technology advances, Rosowski et al. (2009) used computer-assisted time-averaged holographic measurements in chinchilla, cat and human. They classified the TM motions into three regimes. At low frequencies (400-500 Hz), the entire TM showed a motion pattern with up to three displacement maxima. At 4 kHz the human TM showed more complex patterns, composed of areas of high-magnitude motions separated by lines of low-magnitude motions. This finding is in good agreement with the results reported by Tonndorf & Khanna (1972). At higher frequencies (above 8 kHz in human) they observed an "ordered pattern" which is composed of a multitude of displacement

maxima alternating with displacement minima. These features were distributed in the radial and circumferential directions. Cheng et al. (2010) used a stroboscopic holography system on human TMs and reported a combination of standing waves with a larger amplitude and some superimposed smaller travelling waves.

Optical coherence tomography (OCT) has recently been used for measuring vibrations of the TM. Chang et al. (2013) measured the 3-D shape and motions of the TM and ossicles using OCT vibrography in chinchilla ears. They also reported that the vibration pattern becomes more complex when the frequency increases. The TM vibrations were travelling-wave-like at 1910 and 3050 Hz. Recent advances in OCT of the middle ear have demonstrated its ability to simultaneously capture anatomical image data and Doppler-mode vibration data of the ear in response to sound. In 2016 February, both brightness-mode (B-mode) OCT and Doppler-mode OCT images with a 500-Hz sound stimulus were acquired in a human temporal bone by Professor Adamson and his lab at Dalhousie University. The details of this data acquisition will be elaborated on in Chapter 7. To extend this work and streamline the process, in 2017 June, similar datasets for two additional human temporal bones were collected by me and members of Dr. Adamson's lab. The TM vibration patterns were acquired at 500, 1000 and 2000 Hz. The TM moved in phase at 500 Hz and the maximum displacement appeared in the posterior region. At 1 kHz and 2 kHz there were more complex vibration patterns on the TM.

3.3.2 Vibration patterns of the ossicles

The motions of the ossicles change with frequency. Several studies based on 1-D measurements have indicated that the lever ratio is frequency dependent. Gyo et al. (1987) reported that the lever ratio was nearly constant in the low-frequency region below 1 kHz but that between 1 and 2 kHz the lever ratio increased as the frequency increased and achieved a peak at 2 kHz. When frequencies increased above

2 kHz, the lever ratio decreased. The changes of the lever ratio corresponding to the higher frequencies could be interpreted as a change of the malleus and incus rotation axis.

Decraemer and Khanna (1999), making 3-D measurements, found that at low frequencies (300 Hz) the malleus and incus moved in phase, with the tips of the anterior mallear process and posterior incudal process fixed, corresponding to a stationary rotation axis. The stapes moved in a piston-like way in the direction perpendicular to the oval window. The inward motion of the umbo produced an inward motion of the footplate. However, at higher frequencies (e.g., 5 kHz), while the malleus and incus started moving out of phase, the stapes motion retained its piston-like motion. They concluded that "the anatomical connection between the incus and stapes is almost a point-to point contact", which allows the complex malleus and incus motions to result in a simple stapes motion. It was reported that at 10 kHz, however, an inward motion of the umbo producesd an outward motion of the footplate. A later study by Decraemer et al. (2004) used interferometry and microCT to measure the spatial motion of the middle ear. They observed a large slippage in the malleus-incus joint. Further measurements of 3-D vibration motions of the ossicular chain were done by Decraemer et al. (2011, 2014) in living gerbils.

3.4 Mathematical models of the middle ear

3.4.1 Introduction

The most common modelling approaches for the middle ear include lumped-parameter models and FE models. An introduction to the fundamentals of modelling middle-ear mechanics is presented in Funnell et al. (2012). Volandri et al. (2011) reviewed FE models of the TM, and Funnell et al. (2013) reviewed models of the whole middle ear. A brief review of previous models of the TM and middle ear is provided in this section. FE theory will be introduced in the next chapter.

3.4.2 Non-finite-element models of the middle ear

Early mathematical models of the middle ear included lumped-parameter models where each middle-ear structure is lumped as an equivalent ideal electrical circuit element (e.g., Zwislocki, 1957), with the variables dependent only on time and not on space. Later on, analytical models (Wada & Kobayashi, 1990) and semi-analytical models (Rabbitt & Holmes, 1986) were formulated to provide the solution in both time and space domains. Some hybrid models have been used (e.g., Eiber & Kauf, 1994) in which the ossicles are represented by rigid bodies and the ligaments and joints are represented by lumped-parameter springs and dashpots. Hudde and Weistenhofer (1997) described what they referred to as a 3-D circuit model. However, such models cannot fully represent the complex 3-D geometry and distributed nature of the middle ear, which contains many irregular, asymmetrical and non-uniform interconnected parts. On the other hand, the FE method is capable of modelling irregular spatially distributed structures. In addition, the FE method has parameters that are less dependent on assumptions about modes of vibration.

Lumped and hybrid models are still useful in certain cases because of their lower computational cost (Funnell et al., 2013). For example, Calero et al. (2018) describe a multi-body model obtained by simplifying a FE model into a hybrid model. The ossicles were assumed to be rigid bodies, the ligaments and tendons were replaced by lumped spring-damper elements, and the joints were represented as kinematic joints with reduced degrees of freedom (DOFs). The geometry, mesh, mechanical properties and boundary conditions were taken from their previous FE model (Lobato et al., 2017). They concluded that the hybrid model has an acceptable response compared with the FE model and that the reduced number of DOFs at the joint is an acceptable representation of the human middle-ear dynamics.

3.4.3 Finite-element models of the middle ear

Funnell and Laszlo (1978) used a 3-D FE model to investigate the low-frequency behaviour of the cat TM within the range of linear vibration amplitudes. The eardrum geometry was approximated by circular arcs based on previous coarse shape measurements from the literature. The combined ossicular and cochlear load was represented at an assumed fixed axis of rotation by a frequency-independent rotational stiffness. Funnell (1983) extended this model to higher frequencies. The dynamic response of the model to a uniform sound pressure was presented as the modes at natural frequencies. Later on, damping effects were added to the model, represented as mass-proportional Rayleigh damping (Funnell et al., 1987). All of the mechanical parameters except damping were based on *a priori* estimates.

Williams and Lesser (1989, 1990) presented linear dynamic FE models of the human TM and ossicles but the models were only 2-D. Wada et al. (1992) presented a 3-D linear dynamic FE model of the human TM and ossicles. Vibration patterns of the eardrum and ossicles were in approximate agreement with the experimental results of Tonndorf and Khanna (1972).

The earlier studies assumed that the anterior mallear process and the posterior incudal process defined a fixed axis of rotation (Funnell & Laszlo, 1978; Wada et al., 1992). However, the complexity of the 3-D motion of the ossicular chain and the variation of the position of the ossicular axis with frequency makes it necessary to model the ossicles and their suspension as well (Decraemer et al., 1991). Various imaging modalities have been used for FE model building (Decraemer et al., 2003). A recent review of image segmentation methods used for 3-D reconstruction of the ear can be found in Ferreira et al. (2012).

Previous measurements of TM shape were improved using moiré topography (Dirckx & Decraemer, 1989), and Funnell and Decraemer (1996) incorporated the measurements directly into FE models of the cat TM. They used TM deformations in response to large static pressures to facilitate the

determination of the boundaries of the PF, PT and manubrium. This study indicated the importance of the accuracy of the shape measurement and of models that reflect those measurements.

Serial histological sections have also been used for creating FE models. Funnell et al. (1992) described a FE model of the cat middle ear with the manubrium reconstructed from histological sections. Gan's group built a series of complete models of a human middle ear based on 780 histological sections of 20-μm thickness taken from a left temporal bone (Gan et al., 2004, 2007). Funnell et al. (2005) used very thin (1 μm) histological sections for reconstructing just the ISJ of a middle-ear model.

MR microscopy was used by Van Wijhe et al. (2000) to reconstruct the middle-ear structures of the bat. Prendergast et al. (1999) and Ferris & Prendergast (2000) used low-resolution MR imaging (what they called NMR spectroscopy) to create a middle-ear FE model with and without an ossicular replacement prosthesis. X-ray microCT has also been used in building FE models (e.g., Decraemer et al., 2003; Mikhael, 2005). Several studies have used multiple types of data for reconstructing different structures. For example, microCT can be used for identifying some small bony features, MR images can be used for looking at soft-tissue structures, histological data can be used to validate even smaller features, and moiré data are good for measuring the shape of the TM (Daniel et al., 2001; Elkhouri et al., 2006).

The limited resolution of MR and microCT images cannot provide the thickness distribution of the TM. Therefore, full-field high-resolution thickness distribution maps of the TM have been developed using confocal microscopy (Kuypers et al., 2006) and optical coherence tomography (Van der Jeught et al., 2013).

In early FE models, the cochlear damping was not modelled explicitly and its effect was included in the damping of the TM and ossicles (e.g., Funnell et al., 1987; Ladak & Funnell, 1996). Koike et al. (2002) represented the cochlear damping in their middle-ear model by one dashpot connected to the footplate of the stapes, based on experimental observations that the cochlear impedance is primarily damping.

Sun et al. (2002) modelled the cochlear load with 49 spring-dashpot elements oriented in the direction normal to the footplate plane based on the model used by Ladak et al. (1996). Maftoon et al. (2014) modelled the cochlear load with 4 spring-dashpot elements in his gerbil middle-ear model.

Although the ear canal and middle-ear cavity are often either omitted or modelled as lumped acoustical elements, their geometries are sometimes explicitly included in order to model their acoustical effects at higher frequencies. Prendergast et al. (1999) presented a model that included the ear canal. Koike et al. (2002) and Gan et al. (2004) integrated the ear canal and middle-ear cavity in their FE models of the human ear. Motallebzadeh et al. (2017a) included a fairly detailed representation of the ear canal and middle-ear cavities in their model of the newborn ear.

Chapter 4

Finite-element analysis

4.1 Introduction

The FE method is a robust numerical method for simulating middle-ear vibrations. The advantage of using FEM is that it can incorporate the detailed anatomical and biomechanical properties of individual structures, so that the parameters can be directly connected to the physiological characteristics of the system.

According to Cerrolaza et al. (2017, p. 306), the concept of the FE method was initially introduced in the work of Hrennikoff (1941) and Courant (1943). Although they had different approaches, they shared a common concept: to discretize the continuous domain into a set of discrete sub-domains. Later on, Strang and Fix (1973) founded the mathematical basis for FE analysis. As advances have been made in imaging technologies like CT and MR imaging, manual and semi-automatic meshing gradually evolved. Biomedical engineers took advantage of FE approaches with emphasis on modelling and predicting the bio-performance of certain organs including the middle ear.

In this chapter we discuss the FE method and some concepts that are important for the generation of our FE model of the middle ear. The basic principles of the FE method are summarized in Section 4.2. The important factors in building a FE model are discussed in Section 4.3. Some results from previous middle-ear FE models are presented in Section 4.4. The FE modelling software used in this study is introduced in Section 4.5.

4.2 Principles of the finite-element model

4.2.1 Introduction

In a ‘continuum’ the matter in the body is treated as being continuous in the space it occupies. This assumption means that the body can be continually sub-divided into an infinite number of elements. The FE method uses a finite number of elements to represent the continuum approximately. Although the specific formula derivations and the solutions may be different, the basic process of FE analysis is usually composed of four steps: (1) problem definition, (2) domain discretization, (3) determination of equations and state variables, and (4) solution. The following section discusses these four steps briefly, and then Section 4.2.3 discusses dynamic linear analysis specifically.

4.2.2 Basic steps of finite-element analysis

Step 1: Problem definition

This includes defining the domain, the geometry, the material properties and the boundary conditions, etc. based on the problem.

Step 2: Domain discretization

The defined domain is divided into finite discrete components called elements. Each element has a specific geometric shape (i.e., triangle, tetrahedron, quadrilateral etc.) with a specific internal strain function. The finer the elements, the more accurate the degree of approximation to the real problem, but this always comes with a trade-off with the required computing resources and time. It is always recommended to test the mesh convergence to determine the optimal mesh resolution based on the computing resources available and the requirements for model accuracy.

Step 3: Determination of sets of equations and state variables

When the model mesh has been built for the structure being investigated, the partial differential equations (PDE’s) associated with the physical phenomena can be identified based on the fundamental laws of physics:

I. Equilibrium: The external forces acting on an element will cause displacements of its nodes. Equilibrium is the state of a body at rest or in uniform motion in which the resultant of all forces on it is zero.

II. Continuity: The physical problem must present continuity and valid boundary conditions.

III. Constitutive relations: The physical problem must obey a stress/strain law.

For a linear static problem, for example, the equilibrium condition governs the relationship between the force, stiffness and displacement, which can be expressed in the equation

$$\boldsymbol{Ku}=\boldsymbol{f}$$

where $\boldsymbol{K}$ is the stiffness matrix, $\boldsymbol{u}$ is the displacement vector and $\boldsymbol{f}$ is the load vector. The overall stiffness matrix relates the forces on the structure to the displacements at all the nodes. A sufficient number of boundary conditions must be known to properly solve the equations. The compatibility condition ensures that the displacements of the elements are continuous across edges shared between elements. The basic principle is that if two of these elements share a common edge or face, then their individual force-displacement matrices can be combined to give the total relationship for the joined shape. The strains and the stresses of each element can be calculated from the displacements and the known material properties.

For a dynamic mechanics problem, the equilibrium force-displacement equation of the FE model is

$$\boldsymbol{M}\ddot{\boldsymbol{u}}+\boldsymbol{C}\dot{\boldsymbol{u}}+\boldsymbol{Ku}=\boldsymbol{f}(\boldsymbol{t})$$

where $\boldsymbol{M}$ is the mass, $\boldsymbol{C}$ is damping, $\boldsymbol{K}$ is stiffness, $\boldsymbol{u}$ is displacement and $\boldsymbol{f}$ is external force.

Step 4: Solution

Linearity means that, when the structure deforms, the forces and displacements (and the stresses and strains) always follow linear relationships. Non-linearity means that the force-displacement relationship changes with the current state of the displacements, forces, stresses and strains (e.g., Zienkiewicz &

Taylor, 1991). This thesis considers small middle-ear vibration amplitudes, which are linear, so the problem can be considered to be linear.

4.2.3 Dynamic linear analysis

When subjected to a transient force, a system will exhibit a reduction in the amplitude of its movement as a result of energy being drained from the system to overcome frictional or other dissipative forces. This phenomenon is called damping. The damping of a mechanical system is more difficult to understand than its mass or stiffness since it deals with processes that are difficult to isolate and measure. Therefore, several different models have been proposed for describing damping in a mechanical system. One of the more common models for damping, and the one that is used throughout this research, is Rayleigh damping.

Rayleigh damping assumes for convenience that the damping matrix is a linear combination of the mass and stiffness matrices, where α and β are the mass and stiffness damping parameters (e.g., Bathe, 2016, p. 797):

$$\boldsymbol{C} = \alpha \times \boldsymbol{M} + \beta \times \boldsymbol{K}\,.$$

However, these two damping parameters do not have real physical meanings and cannot be measured through experiments. In order to estimate the values of these parameters for a specific system, they can be linked to a physically relevant parameter, the damping ratio (ζ), which can be computed from α and β:

$$\zeta = 0.5 \times (\alpha/\omega + \beta \times \omega)$$

where ω is the angular frequency (radians/sec), and ζ is the damping ratio. The damping ratio is a measure of how rapidly oscillations decay from one cycle to the next. The value of ζ can vary from undamped ($\zeta = 0$), through underdamped ($\zeta < 1$) and critically damped ($\zeta = 1$), to overdamped ($\zeta > 1$). The damping ratio for given Rayleigh coefficients changes with the angular frequency, as illustrated in

Fig. 4-1. The effect of α is dominant at the lower frequencies and quickly decreases as the frequency increases. The effect of β starts from 0 and linearly increases as the frequency increases.

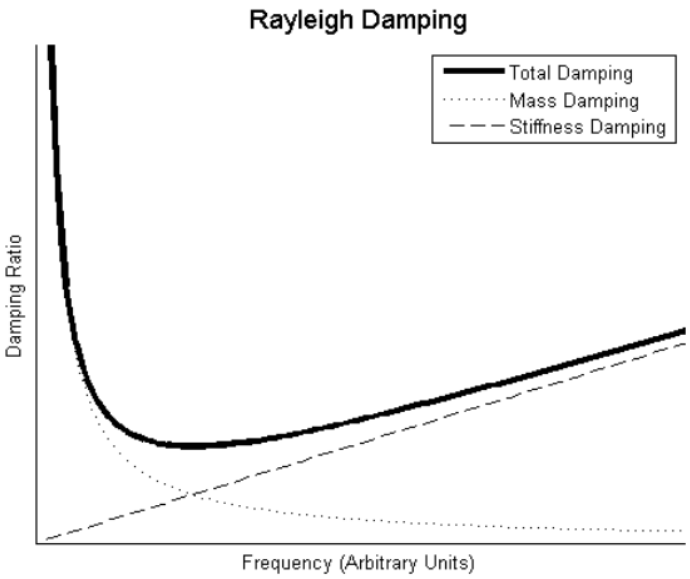

Fig. 4-1: The dependence of the damping ratio on frequncy in Rayleigh damping. The effect of the mass damping (α) and the stiffness damping (β) are presented. The total damping ratio is the sum of the mass-proportional and stiffness-proportional damping ratios (Gariepy, 2011).

4.3 Important factors in building a finite-element model

When building a FE model, there are four main factors that should be carefully considered to ensure a thorough and accurate representation of reality: (1) the geometry, (2) the nodes and the element types and sizes, (3) the boundary conditions of the object to be modelled, and (4) the material properties.

4.3.1 Model geometry

In this study, to represent the geometry of an object that is being modelled using the FE method, the modelling started with structure segmentation by tracing and segmenting the structure outlines from imaging data (i.e., microCT or OCT). Such segmentation is available in many image-based 3-D model

building software packages and can be done manually, semi-automatically or automatically. The 3-D segmentation software used in this study is Fie (Funnell, 2018a), which has been evolving in our lab to meet the demands of our research. It is discussed in Chapter 5.

4.3.2 Nodes and elements

A FE node is a coordinate location in space with associated DOFs defined. A DOF can represent either translational or rotational motion of a node. An element is the basic building block of FE analysis. It can be described in terms of a mathematical relation that defines how the DOFs of a node are related to those of other nodes. Elements can be classified based on their family, order, and topology. These three characteristics are discussed in the following paragraphs. Which type of element is used for FE analysis depends on the type of object that is to be modelled.

The family refers to the dimension and type of the element. A single element can be 1-D (e.g., a line), 2-D (e.g., plane stress and plane strain), or 3-D (Fig. 4-2). In 2-D models, the elements are generally either triangular or quadrilateral. In 3-D solid models, the elements are usually either tetrahedra or hexahedra (bricks). The shell element is sometimes used for thin 3-D structures because using solid elements could either require a very fine mesh, which greatly increases the computational requirements, or involve poor element aspect ratios.

The order of an element refers to the order of the interpolation functions. There are linear (first-order), quadratic (second-order) element and biquadratic elements. (Higher-order elements are also possible.) Linear elements have two nodes along each edge. Quadratic elements have an additional node in the middle of each edge. Bi-quadratic elements (as used in Code_Aster) have an additional node in the middle of the element. Each unconstrained node of a shell element has six DOFs: three translations (x,

y, and *z*) and three rotations (around *x, y*, and *z*). In contrast, each unconstrained node in a 3-D solid element has only three DOFs, all of them translational.

Element topology is the general shape of an element (for example, a triangle or a quadrilateral). Elements of different topologies are used according to the characteristics of the structures to be modelled. In this study, triangular elements were used since they are more appropriate for the geometrically irregular structures in the middle ear.

In this study, the TM is modeled as a thin shell, while the ossicles, the TMMC and the ISJ are all modelled as solid elements.

The element aspect ratio can affect the quality of the mesh. It is a measure of an element's deviation from having all sides of equal length. A high aspect ratio occurs with long, thin elements. Elongated elements which have high aspect ratios sometimes cause numerical problems. The locally developed software Fad can detect elements with high aspect ratios which could possibly contribute to numerical problems.

4.3.3 Boundary conditions and loads

FE models include the boundary conditions and loads imposed on the structures. The boundary conditions define the interaction of elements with surrounding structures.

Loads are external forces acting on a body. Depending on the area the loads are imposed on, they can be classified into distributed loads (applied on lines, surfaces or volumes) and concentrated loads (applied on nodes). Volume loads are related to characteristics such as weight (gravity) or electromagnetic effects. Volume loads are not used in this study because we do not need to simulate gravity. Regardless of their nature or source, the distributed loads must be converted to consistent nodal forces for FE analysis.

4.3.4 Material properties

The stresses and strains in a structure are partially derived from the material properties, so proper material properties are essential to ensure accuracy. Material properties can be linear or non-linear. Materials behave linearly up to a certain strain before becoming stiffer (e.g., Holzapfel, 2000). Gariepy (2011) mentioned that the results of Qi (2008) indicated that the onset of the non-linearity in the middle ear seems to occur at an applied static pressure of approximately 1000 Pa in the middle ear. In this study, the sound pressure used is 2 Pa and will certainly not cause a large enough deformation of the tissues to drive the system into the non-linear range. Therefore, in all of the simulation of this research, the material properties are assumed to be linear.

Material properties can be isotropic, transversely isotropic, orthotropic or fully anisotropic. For an isotropic model, the properties are defined to be the same in all directions. An anisotropic material is one with different properties in different directions. A transversely isotropic material has a single axis of symmetry that is normal to a plane of isotropy. An orthotropic material has three orthogonal planes of symmetry. The middle-ear structures are considered for simplicity to be composed of isotropic and uniform materials in this study.

4.4 Results from previous middle-ear finite-element models

Volandri et al. (2011) summarized the differences among eight models from eight previously published studies (Ferris & Prendergast, 2000; Koike et al., 2002; Sun et al., 2002; Ferrazzini, 2003; Gan et al., 2004; Mikhael, 2005; Lee et al., 2006; Liu et al., 2009). They evaluated and compared the previous models and reran the simulations with a modified middle-ear geometry of their own. Material properties, damping parameters and constraint representations were implemented based on the previous reports. Volandri et al. (2011) performed modal and harmonic analyses. They recorded resonance frequencies as the main modal analysis result, evaluated in the 0–6 kHz frequency range. The

displacements of the node corresponding to the umbo location were also recorded and compared. In addition, a uniform harmonic input pressure stimulus of 80 dB SPL (Ferris & Prendergast, 2000; Koike et al., 2002; Lee et al., 2006) or 90 dB SPL (Ferrazzini, 2003; Gan et al., 2004; Mikhael et al., 2004) at the TM was used and the results were normalized for comparison. Other values (in the range 80–120 dB SPL corresponding to 0.2 and 20 Pa, respectively) were applied as input sound pressure at the opening of the ear canal in Sun et al. (2002). Liu et al. (2009) did not report the input sound pressure. The model results were compared by Volandri et al. (2011) in terms of the first resonance frequencies and the maximum displacement values at the umbo at those frequencies.

Volandri et al. (2011) reported that the first resonance frequency could be observed at approximately 0.9–1.5 kHz for all of the models reviewed except for the models of Ferrazzini (2003), Sun et al. (2002), Gan et al. (2006) and Liu et al. (2009). The first resonance frequency of Ferrazzini's model occurred at 247 Hz. A possible reason suggested by Volandri et al. (2011) for such a low resonance frequency is that the values used by Ferrazzini were obtained by performing an iterative fitting process during the model validation process but the effectiveness of the fitting procedure was not clearly presented and such a process is dependent on the number of parameters involved and on the comparison criteria. For the models from Sun et al. (2002), Gan et al. (2006) and Liu et al. (2009), a low resonance frequency (about 600–650 kHz) was also reported. Volandri (2011) observed that a fully clamped TM, or one suspended by stiff springs, results in a higher first resonance frequency, as presented by Mikhael (2005), Koike et al. (2002), Ferris & Prendergast (2000) and Kelly et al. (2003), compared with a TM suspended by a fibrocartilaginous ring as proposed by Sun et al. (2002), Gan et al. (2004), Lee et al. (2006) and Liu et al. (2009). In our study, the TM is fully clamped, and the first resonance frequency appears at 1200 Hz.

4.5 Finite-element software

The FE software used in this study, Code_Aster and SAP IV, are discussed in the following sections.

4.5.1 Code_Aster

Code_Aster (www.code-aster.org) is free/libre and open-source (FLOSS) software for numerical simulation of materials and mechanical structures, developed by the "Analyses Mécaniques et Acoustiques" department of the "Recherche et Développement" service of Électricité de France. It is a complex package developed since 1989. It was made available under the GNU GPL licence in October 2001. It is mainly written in Fortran, with some add-ons written in Python. Its source code can be freely downloaded from the project Web site. A version for Microsoft Windows is available, having about the same functionality as the Linux version. The documentation is mainly written in French, with machine-translated versions in English. It is used to solve different types of mechanical, thermal, acoustical and other problems, and can be applied in solving both linear and non-linear problems and both static and dynamic problems. Code_Aster supports linear, quadratic and bi-quadratic elements. It is considered to be one of the best available FLOSS approximations of commercial FE software, in terms of its general workflow which features a full integration of all steps of the analysis beginning with the geometry definition and ending with the post-processing step (Velten, 2009, p. 276).

4.5.2 SAP IV

SAP IV is a FE analysis program for static and dynamic linear structural analysis. It supports only linear (first-order) elements. The program was originally developed in the 1970's at UC Berkeley in the Fortran language. The source code and documentation are currently available under a non-free licence from NISEE at UC Berkeley (https://nisee.berkeley.edu/elibrary/getpkg?id=SAP4). The original software was freely distributed in source form and was modified for various platforms by various

people. Professor Funnell has modified it to accommodate middle-ear FE analysis over the years. A brief list of local modifications to SAP IV, in approximate decreasing order of importance, can be found at http://audilab.bme.mcgill.ca/~funnell/AudiLab/sw/sap.html.

Fad (Funnell, 2018b) is used to read a .sap file from Fie, modify it and write a new one to be used in SAP IV. The input .sap file defines what type of simulation is desired, which can be a static problem, eigenvalue problem or direct step-by-step time-domain response (also used for computing frequency responses). For static analysis, Fad will allow you to specify the magnitude of the applied pressure even if it has already been defined. For eigenvalue cases, Fad will ask you how many eigenvalues you wish to solve for. The dynamic analysis features include modal analysis to obtain mode shapes and frequencies, as well as time-domain and response-spectrum analysis. In dynamic analysis, Fad will allow you to choose the α and β damping coefficients, the total time to be simulated, the time step to use, and the specification of a pressure or of concentrated-force loads, if not already defined in Fie. The simulation is then run from the command line. Fod (Funnell, 2016) is used for displaying the results of 3-D finite-element simulations. It takes the simulation-result files created by SAP IV as input, which include the .res plain-text file and (for time-domain simulations) the .hist binary file. It has options to display the results in both time and frequency domain. It also has the option of exporting a VRML file containing a 3-D model with displacement vectors added or to export to different graphics output types as specified by the user.

Chapter 5
Methods

5.1 Introduction

For the present study, we obtained B-mode OCT images of a human temporal bone for which simultaneous Doppler-mode OCT images were collected. The Doppler OCT images, masked by the B-mode OCT images to reduce noise, are also segmented and the resulting 3-D model is transformed to Cartesian coordinates and aligned with the microCT-based model. For the same ear, we also received X-ray microCT images. The microCT data provide a higher spatial resolution than OCT and are free from the shadowing and multiple-scattering artifacts which are present in the OCT image. The microCT images are manually segmented to create a FE model of the middle ear. The simulated vibration patterns from this FE model are compared with the measured Doppler-mode OCT velocity data to validate the finite-element model.

The imaging techniques used in this thesis, including microCT and OCT, are introduced in Sections 5.2 to 5.4. Section 5.5 talks about the application of the Doppler OCT in our experimental measurements. Section 5.6 covers image acquisition and pre-processing. The process of building the middle-ear models and the challenges in the model-building process are described in Section 5.7.

5.2 Micro-computed tomography

CT is a non-destructive imaging technology which has served as the basis for several modalities, including X-ray CT, MR imaging and positron emission tomography (PET). They are capable of imaging internal structures including soft tissues and bones. Only X-ray CT will be discussed here since it is the one used for this work.

The data of X-ray CT are acquired from detectors that are placed on one side of the object to be scanned while the X-ray tube is placed on the opposite side of the object. The X-ray tube sends X-rays toward the detectors, through the object. As these rays pass through the object, they are absorbed to different degrees, due to the variations in composition of the structure. Therefore, when received by the detectors placed on the other side, the system creates an array of pixels with attenuation coefficients to produce a radiograph (known as a projection image). Either the source and detectors or the sample is then rotated by a small angle and another projection image is taken at the new position. This procedure is iterated until the sample has rotated 180 or 360 degrees, producing a series of projection images.

The rotation is necessary in order to have data representing the volume of interest. The projection images are used to reconstruct a 3-D image. There are many factors that can affect the image quality, including the rotation speed and the numbers of projections being acquired. X-ray microCT imaging technology has proven capable of imaging middle-ear structures (Decraemer et al., 2003). For this project, we chose to use microCT data to create a moderately realistic 3-D model of a human middle ear, with image resolution at the micrometer level. The microCT scan of a human cadaver left ear was made available to us by Professor Robert Adamson at Dalhousie University, Halifax, in 2016 February. The data were acquired using a Triumph II PET/SPECT/CT scanner (TriFoil Imaging, Chatsworth, California). The scanned specimen was reported to have no pathological changes in the middle ear. The X-ray energy was set to 70 kVp. The image set contains 512 sections of 512×512 pixels each. The size of the image was set to 53.25×53.25mm, with the isotropic voxel size being 104 μm. The original format of the dataset is individual DICOM files. This format needs to be converted to a format that Fie (Funnell, 2018a) can recognize (i.e., 8-bit TIFF, JPEG or PNG). The original DICOM images for this research have more than 8 bits/channel, so post-processing is required to examine histograms and

determine a good grey-level range to collapse the pixel data down to 8 bits/channel (i.e., 8 bits/pixel for grey-level images, which have a single channel).

For example, if there is a separate DICOM file for each slice of a stack, the ranges of minimum and maximum values can be obtained with 2 commands in ImageMagick (http://imagemagick.org/script/index.php) that dump the values into text files:

```
identify -define dcm:display-range=reset -verbose *.dcm | grep -A 2
"Overall:" | grep min > min.txt
identify -define dcm:display-range=reset -verbose *.dcm | grep -A 2
"Overall:" | grep max > max.txt
```

The overall range can then be determined by examining the .txt files, possibly sorting them. The files can then be converted to JPEG by giving a command like the following:

```
mogrify -define dcm:display-range=reset -level min%,max% -quality 95
-format jpg *.dem
```

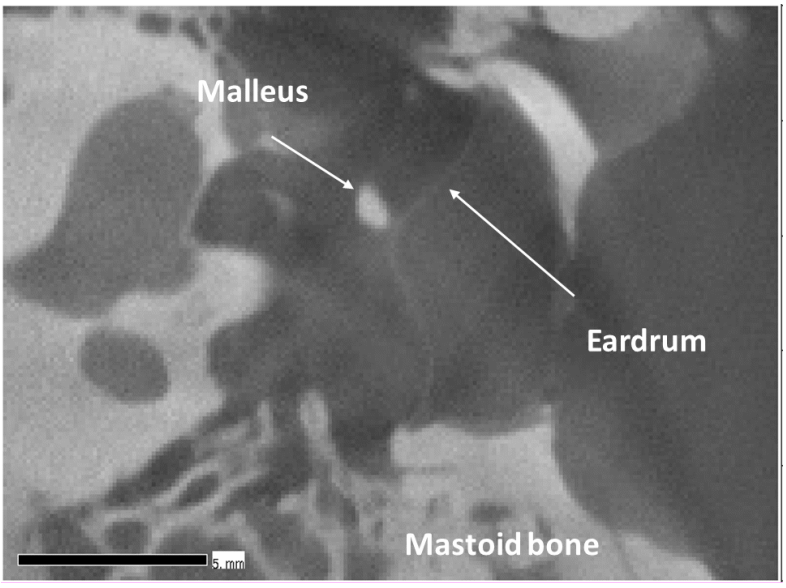

Fig. 5-1: Sample microCT image of the middle ear. The isotropic voxel size is 104 µm.

Some trial and error may be required to determine the best levels. The minimum and maximum levels were set to 48 and 55.5 in this study. These values were found visually to generate the best image quality. The value of 95 for quality (which has a maximum value of 100) specifies the amount of lossy JPEG compression and has been found to result in negligible information loss for our application, especially given that the reduction to 8 bits has already thrown away a lot of information (http://audilab.bme.mcgill.ca/~funnell/swil.html#bitmap). A sample image after post processing is presented in Fig. 5-1. The cross-section of the middle-ear cavity, TM (eardrum), malleus (manubrium) and the mastoid bone can be clearly identified in this image. This microCT dataset was used to generate the complete middle-ear FE model, as discussed in Section 5.4.

5.3 Optical coherence tomography

OCT is an interferometric optical imaging technique which can produce non-invasive, *in vivo*, high-resolution depth-resolved images in biological specimens (e.g., MacDougall et al., 2015a). The OCT system sends a spatially coherent light beam (typically near-infrared light) through the tissue sample and the back-scattered light will interfere with a reference light beam to form the interference patterns. OCT is suitable to be used in diagnosing middle-ear pathological changes since the eardrum is thin and translucent, which allows easy penetration of the light. Depending on the properties of the light source and the specimen, OCT has achieved sub-micrometer resolution.

Different from time-domain OCT, in frequency-domain OCT the broadband interference is acquired by encoding the optical frequency in time with a frequency-scanning source in swept-source (SS) OCT, or by encoding spatially in spectral-domain (SD) OCT. The light source in SD-OCT is a super-luminescent diode, the broad-wavelength light of which is divided into a spectrum by diffraction and then projected onto a spectroscope where light interference is generated. The light source in SS-OCT,

on the other hand, is already divided into a spectrum by a tunable laser, so no spectroscope is needed. This simplified setting contributes to a faster data acquisition compared to SD-OCT and it also returns a clearer image (e.g., Kishi, 2016).

For the OCT image acquisition, spatial scanning of the sample can be accomplished by either moving the light source with respect to the sample, or moving the sample while keeping the light fixed. One axial depth scan along the laser beam is called an A-scan (*z* axis only, the *x* and *y* axes defining the plane perpendicular to the laser beam). A linear scan will yield a two-dimensional data set corresponding to a cross-sectional (*x*-*z*) image, while an area scan achieves a three-dimensional data set corresponding to a volumetric (*x*-*y*-*z*) image.

5.4 Doppler optical coherence tomography

For Doppler OCT, the structural B-mode images of the sample are generated from the magnitudes of the *x*-*z* scans. Doppler-mode OCT imaging relies on the Doppler effect induced by tissue motion to measure the vibration patterns of the tissue. The Doppler shift of light waves scattered from a moving target is proportional to the frequency of the interrogating wave, and proportional to the velocity of the target.

The relationship between observed frequency f and the emitted frequency f_0 is given by:

$$f = \left(\frac{c + v_r}{c + v_s}\right) f_0$$

where c is the velocity of waves in the medium; v_r is the velocity of the receiver relative to the medium, positive if the receiver is moving toward the source, and vice versa; and v_s is the velocity of the source relative to the medium, positive if the source is moving away from the receiver, and vice versa.

The Doppler-mode images record the proportional phase shifts which are generated from the changes in the position of the reflecting structure. The Doppler shift can be detected by analyzing the time-domain OCT data in frequency space. The mean velocity of the moving structure as a function of depth can be estimated from the computed centroid frequency of the local interferometric reflectance, by using overlapped short-time Fourier transforms. This allows an estimation of Doppler shifts along each A-scan (MacDougall et al., 2016).

On the other hand, the depth-resolved phase changes of OCT Doppler imaging can also be acquired by comparing sequential or adjacent depth scans in the frequency domain. One way is to perform a Hilbert transform on the OCT signal, and then obtain the Doppler shift by dividing the phase difference between two adjacent scans by the time between line acquisitions (MacDougall et al., 2016).

5.5 Applications of Doppler optical coherence tomography

Recent advances in Doppler OCT of the middle ear have demonstrated its ability to simultaneously capture anatomical image data and Doppler-mode vibration data of the ear in response to sound.

There are many other techniques that have been used for studying middle-ear structures and vibrations, but each of them has certain limitations. Laser Doppler vibrometry (LDV), for example, provides a way to directly measure TM vibrations, but it cannot provide vibration measurement of the ossicular chain through the intact TM. The real advantage of using OCT to image the human middle ear is that the thin and translucent TM allows the laser light to penetrate to the deeper middle-ear structures and provide non-invasive imaging.

The use of OCT for anatomical middle-ear imaging in humans was first suggested by Pitris et al. (2001). Since then, it has been used as a diagnostic tool for examination of the TM, the ossicles and

cochlea (e.g. Heermann et al., 2002; Djalilian et al., 2008; Just et al., 2009). It has also been successfully applied to study ear anatomy in several animal models over the last decade (Wong et al., 2000; Choudhury et al., 2006; Hong & Freeman, 2006; Sepehr et al., 2008; Gao et al., 2011). More recently, Doppler OCT was used to provide both shape and vibration information for chinchilla (Chang et al., 2013) and cadaveric human middle ears (Subhash et al., 2012).

The Doppler OCT system used in this study was built by Professor Robert Adamson and his lab at Dalhousie University, Halifax. Their objective is to build an *in vivo*, real-time phase-sensitive SS-OCT imaging system with Doppler vibrometry capabilities, which can provide the clinician with efficient and accurate images for diagnosis. Detailed information about the system can be found in McDougall et al. (2015b). A diagram of the system design is shown in Fig. 5-2. The laser light source is an akinetically-tuned swept-frequency laser (SLE-101, Insight Photonics, 1528.8 to 1570 nm bandwidth centred at 1550 nm). 'Akinetic' means that there are no mechanically moving parts to generate the sweep. The laser is based on an integrated semiconductor design which enables a fully electronic control of laser operation. This design overcomes the limitations of unstable or drifting mechanical movements of a conventional source which can result in overall degradation of the system's performance. This light source represents a key technological element for the system, specifically in terms of imaging speed and resolution. A Mach-Zehnder fibre interferometer directs most of the light to the sample and recombines the collected backscatter with the remainder (MacDougall et al., 2016). The linear optical-frequency sweeps are sent at a repetition rate of 100 kHz. The interference pattern generated during each sweep is sampled at 400 Msamples/s at 12-bit resolution. In the measurement, the light source is moved to scan the sample in the x and y directions. The sample is fixed throughout the measurement.

The controller board, based on a field-programmable gate array (FPGA), synchronizes all timing aspects of the system, as well as the generation of a pure-tone acoustic stimulus with the desired frequency. The sound pressure is delivered to the middle ear through a speaker and causes the middle-ear structures to vibrate. The sound energy used in the data acquisition for this thesis was a continuous 500-Hz sinusoidal sound wave with a sound pressure level of 100 dB SPL re 20 µPa.

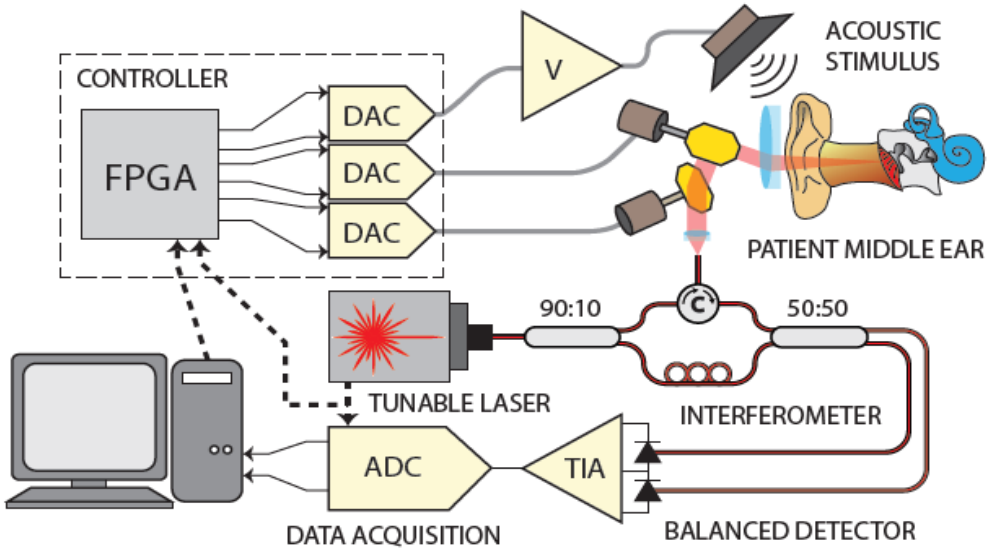

Fig. 5-2: Diagram of the swept-source OCT system designed and built for real-time clinical imaging of middle-ear anatomy and function (MacDougall et al., 2015b)

To achieve the display and control needed for clinical use, a graphical user interface (GUI) using the Qt framework was developed to operate the system hardware and manage patient data (MacDougall et al., 2015a). Real-time signal processing of the interferometric data was implemented on a GPU with NVIDIA's parallel programming platform, CUDA (MacDougall et al., 2015a), and several custom-written execution kernels perform raw-data conditioning, windowing, dispersion compensation, B-mode averaging, and Doppler-mode calculations.

5.6 Image acquisition and pre-processing

The Doppler OCT images include a lot of background noise so a pre-processing step is required. The B-mode image is used to define the region of interest in the Doppler-mode images. This was done by looping through pixels in the B-mode image and setting the corresponding pixel in the Doppler-mode magnitude or phase image to zero if the corresponding B-mode pixel is below a minimum desired level. Fig. 5-3 shows an example of the Doppler-mode image magnitude with the background noise removed by masking with the corresponding B-mode image.

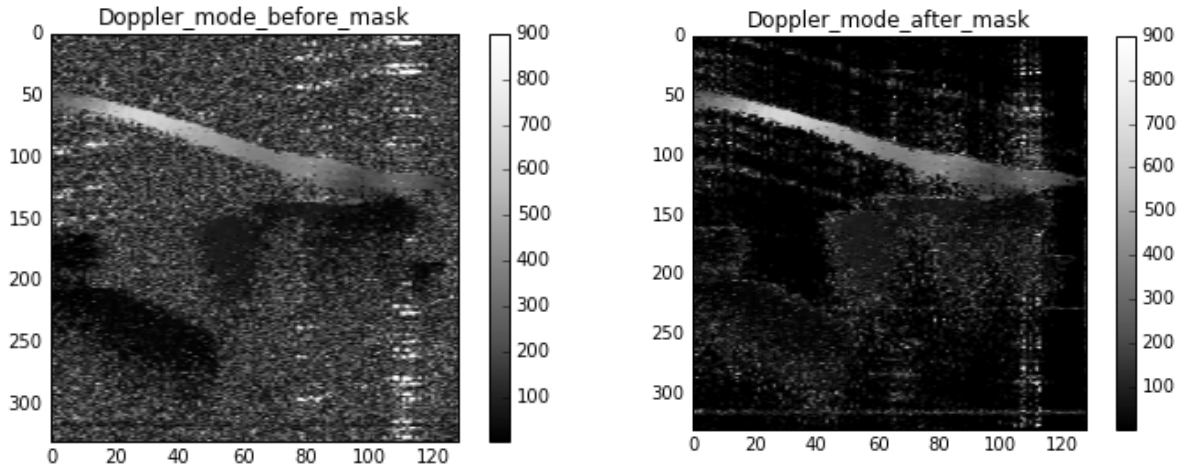

Fig. 5-3: The same cross-section of Doppler-mode imaging before (left) and after (right) "masking" by B-mode imaging. The images are displayed with the same grey scales to emphasize both the shape of the middle ear on the left and the magnitude of vibrations on the right.

5.7 Model building

5.7.1 Introduction

The building of a 3-D FE model involves segmentation; mesh generation; model pre-processing and quality control; simulation; and post-processing. A number of programs (Fie, Tr3 and Fad) have been developed by Funnell (2018) in AudiLab for FE modelling and simulation of complex biomedical structures. These programs and others are used in the pipeline illustrated in Fig. 5-4. Fie is a program to

segment contours in a stack of images; segmentation of each image is performed. Tr3 is a program for triangulating 3-D surface meshes from a series of cross-sectional contours produced by Fie. Gmsh, developed elsewhere, is used for the 3-D volume mesh generation to create tetrahedral elements from the triangulated surface meshes. Fad is a program for pre-processing finite-element models and has the option of exporting the models in different file formats for simulation in different FE software. These various steps will be discussed in more detail in the following sections.

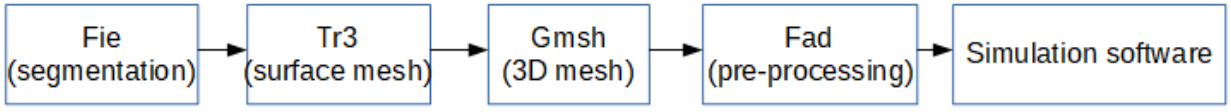

Fig. 5-4: Finite-element modelling and simulation pipeline.

5.7.2 Image segmentation

The aim of image segmentation is to delineate the structures of interest in the anatomical images. Segmentation can be realized by manual, semi-automated and automated methods. Each of these segmentation approaches has different advantages and disadvantages. Manual segmentation is usually tedious and irreproducible, but is often required to delineate subtle structures in areas with low contrast or inadequate image resolution. Automatic segmentation, on the other hand, is faster but usually needs to be checked and edited afterwards. The semi-automated approach combines the advantages of manual and automated segmentation, employing an algorithm to detect contour shapes while permitting user supervision and guidance. The semi-automated approach is used in this study for the segmentation.

The semi-automatic approach includes using manual segmentation first in Fie to delineate the TM carefully, then using the flood-fill tool followed by the snake (active contour) tool for segmenting solid structures, which greatly improves the efficiency and works well for structures with good

contrast. The flood function traces a line around a closed region based on a range of pixel intensities. It allows the user to adjust the range of intensities to change the line shape. It also allows the user to accept only part of the line by using a 'cut' function.

The snake method (Lobregt & Viergever, 1995) is a useful line-fitting function. It can be used in several ways: to refine the lines added manually with only a few points, or to clean up the lines generated from the flood method. The snake function offers a number of settings that can be adjusted. Detailed documentation for how to use the various adjustments can be found at http://audilab.bme.mcgill.ca/~funnell/AudiLab/sw/fie.html#snake.

The actual fitting is done by using the 'slither ahead' function which executes a specified number of iterations of the snake algorithm. If the snake algorithm is having trouble getting part of the line to fit the desired boundary, then manual adjustment can be used to repair the line.

Once a sketch of a contour is drawn using the snake algorithm or manual editing, a special spline-fitting line-smoothing algorithm is used. Spline fitting smooths a line by fitting cubic spline segments (Schneider, 1990), using one user-specified error limit to decide how many segments are required, and then resampling recursively (Foley, 1990) using a second user-specified error limit to decide how many points are required (Funnell, 2018a). The error limits can be changed repeatedly until the desired results are obtained. All the contours are smoothed within their slices before 3-D surface smoothing. Then the function "Points across slices" in Fie is used to provide a way of smoothing a surface across slices. It is done by adjusting the points of a set of lines so that they form smooth curves as seen in the side views. The surface-smoothing function requires that the line has the same number of points in all slices, so the "Resample line" to "Linearly interpolated uniform sampling" option can be used to specify the number of points wanted for all the slices for each line. The resampling will result in points that are very

closely spaced in slices where the line is very short, so the results are usually resampled again after smoothing. The contours on the slices may be distorted by the surface-smoothing algorithm, so one should review the results slice by slice to make sure the results make sense. Several iterations of line smoothing followed by resampling and surface smoothing may be required to achieve a good result. Fig. 5-5 displays a zoomed microCT image with an example of the middle-ear segmentation.

Some special features in Fie were used in the segmentation process to ensure topological continuity and integrity for certain lines across different slices. One of the features is that the connectivity across slices is provided by specifying 'joins' when the topology changes from slice to slice. Caps can also be defined to close the beginnings and ends of 3-D surfaces.

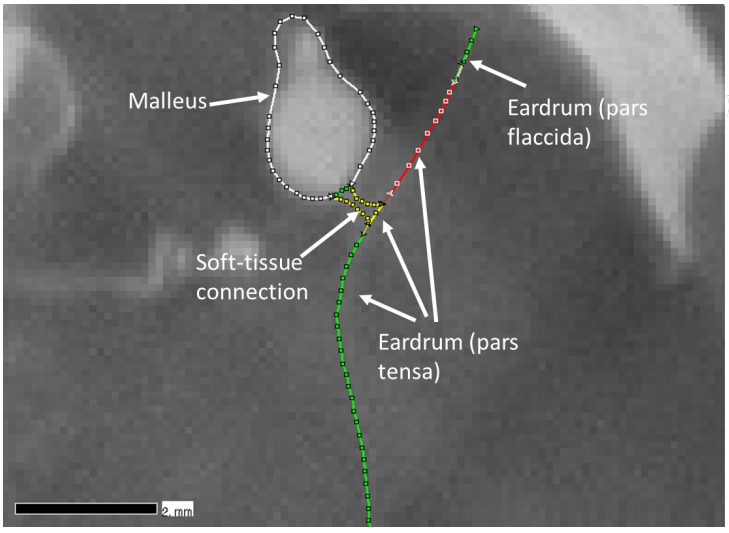

Fig. 5-5: A zoomed microCT image with examples of segmentation.

Segmentation has also been done on the OCT images. One challenge encountered in segmenting the OCT images was that it was hard to define the exact boundaries between the TM and connected temporal bone based solely on the B-mode images. In this case, Doppler-mode images provide a valuable reference where the boundary can be easily identified due to the motion contrast between the vibrating TM and the static temporal bone. In Fig. 5-6, the image on the left is a B-mode image with a

cross-section view of the TM and part of the malleus. The image on the right is the same cross-section in a Doppler-mode image, where the contrast between "in-motion" and "less-moving" structure can be identified from the contrast of the grey scale. The unmoving temporal bone can be identified as well. The end point of the segmentation line of the TM (the green line with the dots) therefore can be determined. After the manual segmentation, both line smoothing and surface smoothing followed as well, as for the microCT segmentation, to ensure a reasonable surface geometry of the structures.

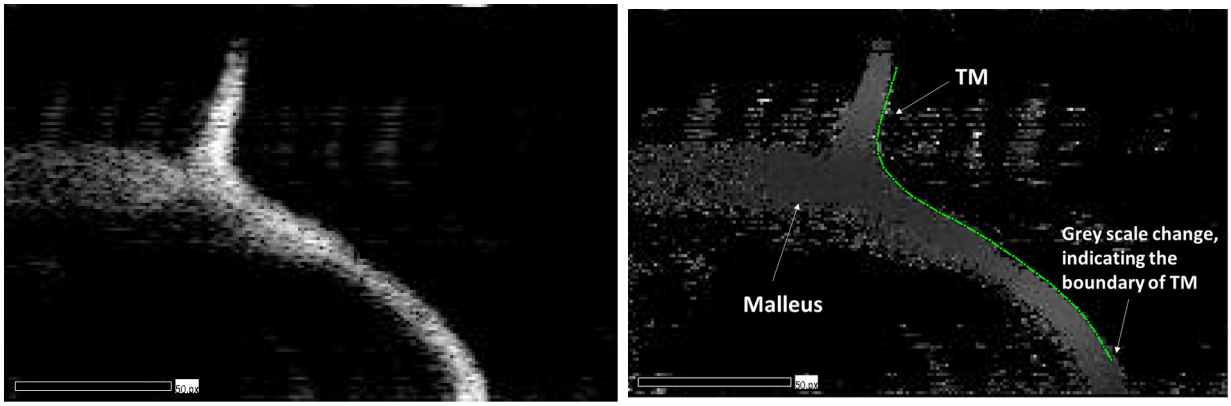

Fig. 5-6: B-mode image with middle-ear structures (left) and Doppler-mode image of the same cross-section. The intensity contrast between the structure in motion (TM), the less-moving structures (ossicles) and the non-moving temporal bone can be identified from the Doppler-mode image.

5.7.3 Mesh generation

The Tr3 program was used for surface mesh generation. This program, given the plain-text (.tr3) model-definition file produced by Fie, triangulates 3-D surfaces between contours in adjacent slices of a dataset (Funnell, 1984a, 1984b). The output .sap file includes the information about the mesh's nodes and elements — such as their coordinates, boundary conditions, and material properties — that will be needed for the FE simulation.

In Fie, the mesh resolution can be defined with the mesh-resolution parameters *ires_xy* (measured in elements/diameter) and *ires_z* (measured in slices). These parameters are read by Tr3 and determine the fineness of the triangular mesh that will be generated. For *ires_xy* =10, for example, the triangle sizes

will be chosen to be approximately 1/10 of an estimated overall diameter of the model; and for *ires_z*=2, every second slice will be used in generating triangles. Different lines can use different *ires_xy* and *ires_z* values, but problems may be caused by using different *ires_z* values for lines which are interconnected.

For the solid structures, 3-D tetrahedral volume meshes are generated using the free and open-source software Gmsh (http://gmsh.info/), which is available as binaries for Linux, MS Windows, and Mac OS X, and also as source code. Fad is used to export the model as a Gmsh .geo file. The exported .geo file contains specifications of the meshing algorithm to be used (Netgen) and the number of optimization passes to be performed (default is 3), and contains computed characteristic lengths. Gmsh generates a .msh file which can be imported into Fad again. Since Gmsh does not modify the original surface nodes or create new surface nodes, Fad can establish a one-to-one correspondence between the original surface shell elements and the surface facets of the tetrahedral mesh produced by Gmsh. Fad can also retrieve boundary conditions and other mechanical properties from the .sap surface-model file that led to the .geo file that led in turn to the .msh file.

For two objects sharing a surface, Tr3 produces the same triangulation for that surface for both objects, and Gmsh does not alter either surface mesh, which allows connections between the two objects.

For the middle-ear model which contains multiple connected components, the tetrahedral mesh has to be generated separately for each component first, and all the components can be joined together in sequence. Two of the components were joined first using Fad, then a third component was added to the combination, and so on. The joined model is exported from Fad in the format required for further processing.

5.7.4 Coordinate conversion

It is important to validate the shapes of the models built from microCT and OCT images. However, due to the fan-shaped acquisition geometry of the OCT images, the resulting 3-D model needs to first be transformed to Cartesian coordinates before aligning with the microCT-based model.

Fig. 5-7 (upper panel) displays the original OCT acquisition geometry. The laser source scans 128 times through one single frame (composed of 128 A-lines) and the total volume consists of 128 frames. The boundary lines represent the shape of the acquired image volume, which can be imagined as the rind of a watermelon wedge. The OCT images consist of voxels identified by row/column/slice numbers that do not take into account the fan shape. This results in a stack of rectangular images which together form a cuboid image volume (Fig. 5-7, lower panel). The 3-D model is segmented from this cuboid image volume which carries the distorted shape information. This 3-D model will be converted to its actual shape point by point by applying the correct transformation algorithm.

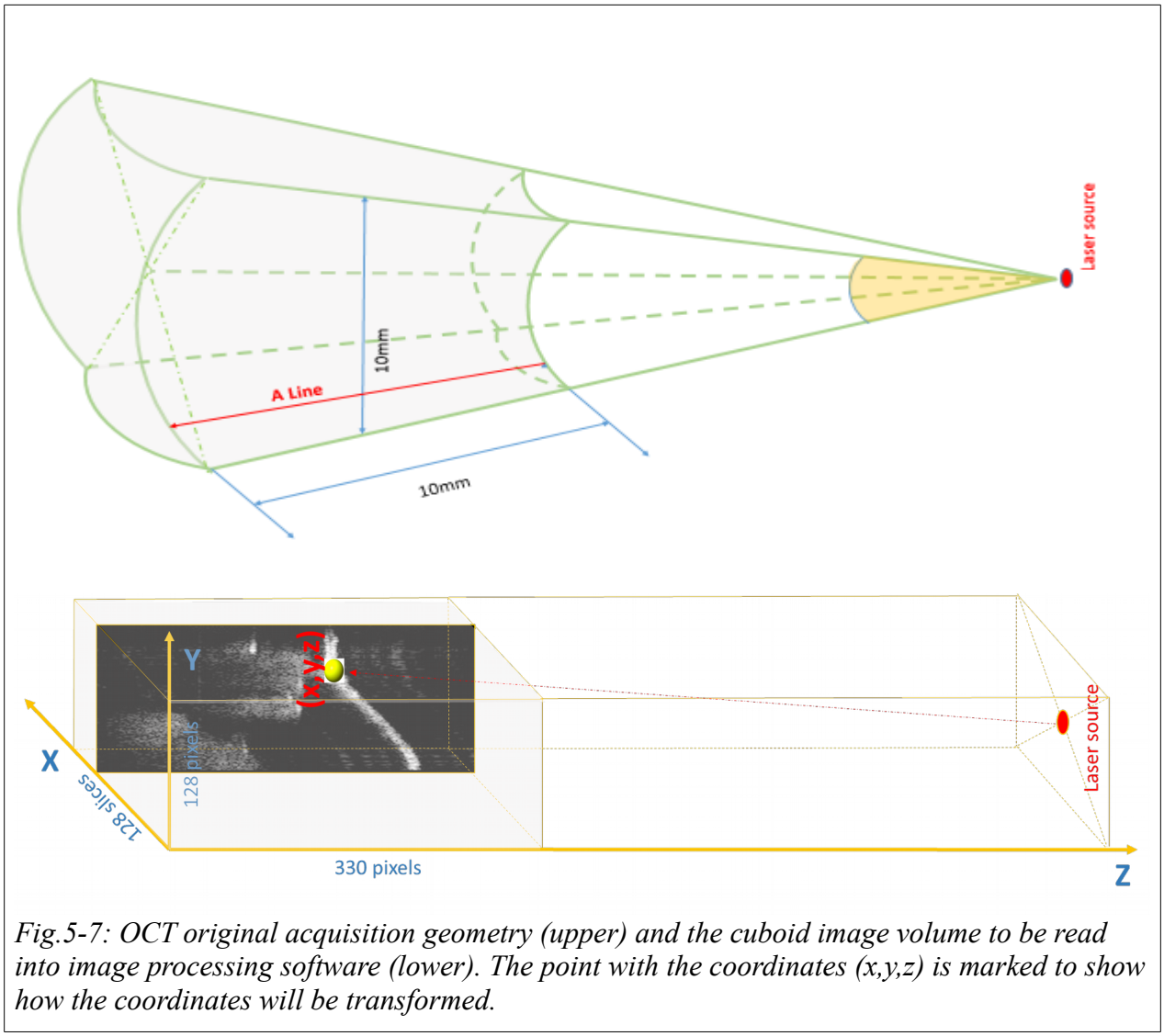

Fig.5-7: OCT original acquisition geometry (upper) and the cuboid image volume to be read into image processing software (lower). The point with the coordinates (x,y,z) is marked to show how the coordinates will be transformed.

The basic idea of the transformation is to map the Cartesian coordinates (x, y, z) to the spherical coordinates (α, θ, r) to represent the relationship between the mapped point (green dot in Fig. 5-7 lower panel) and the laser source (red dot in Fig. 5-7). The cuboid image volume is composed of 128×128×330 pixels, the full swept angle of the scanning setting is 28.6°, and the original acquisition is spherically symmetrical about the laser origin. Thus, the line and slice angular spacing can be calculated. θ is the angle between the line formed by the laser origin and the point (x, y, z), and the line,

presented in Fig. 5-8 (lower panel), is the angle between the line formed by the laser origin and the point (*x, y, z*), and the line formed by projecting the previous line to the yellow plane in Fig. 5-8 (upper panel). The radius r can be calculated as the distance from the laser source to (*x, y, z*)

The left panel of Fig. 5-9 shows the 3-D model with shape outlines segmented from the cuboid image volume; the panel on the right shows the transformed 3-D model with its real shape. The shape and size were changed substantially by the coordinate transformation.

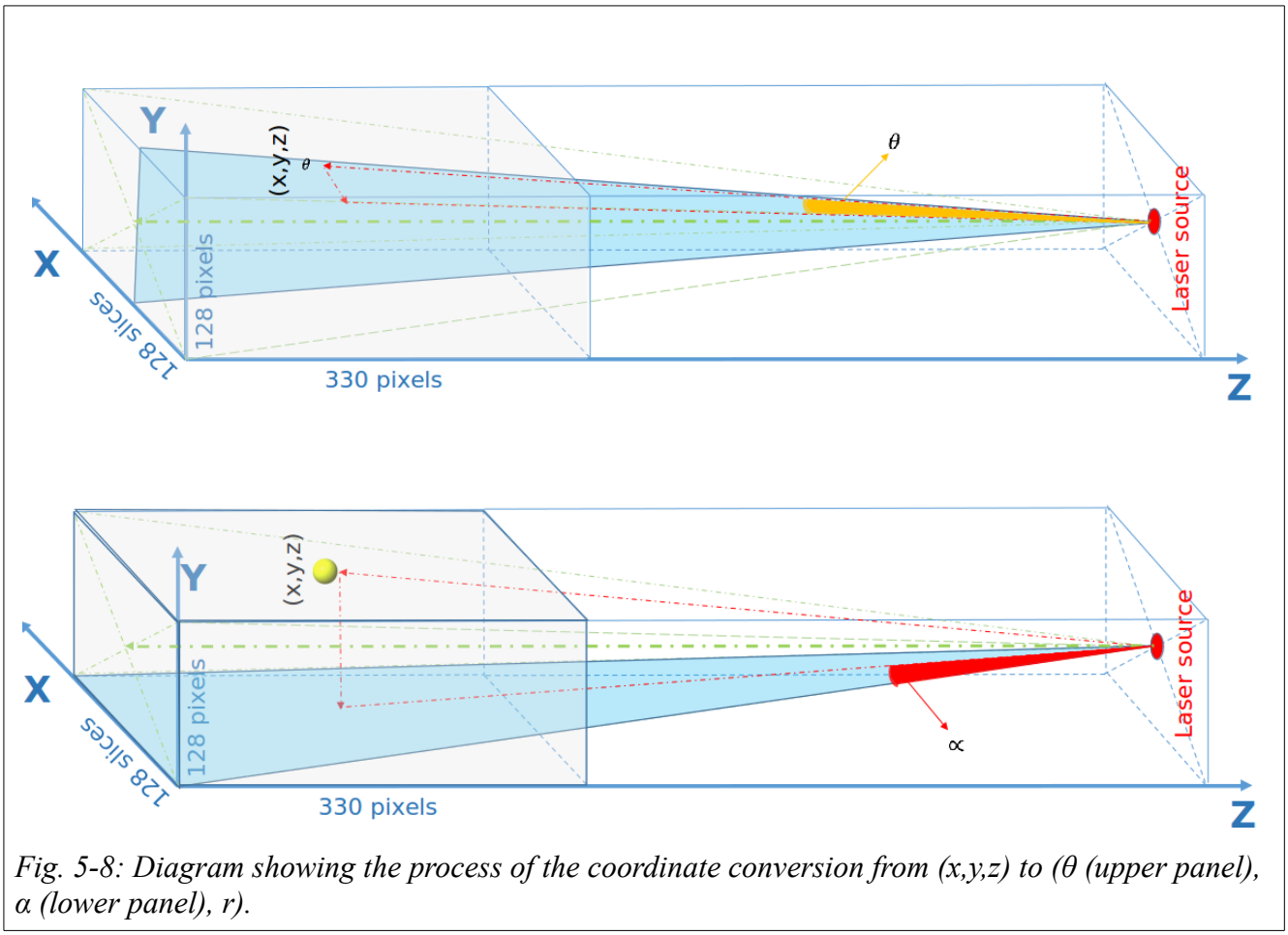

Fig. 5-8: Diagram showing the process of the coordinate conversion from (x,y,z) to (θ (upper panel), α (lower panel), r).

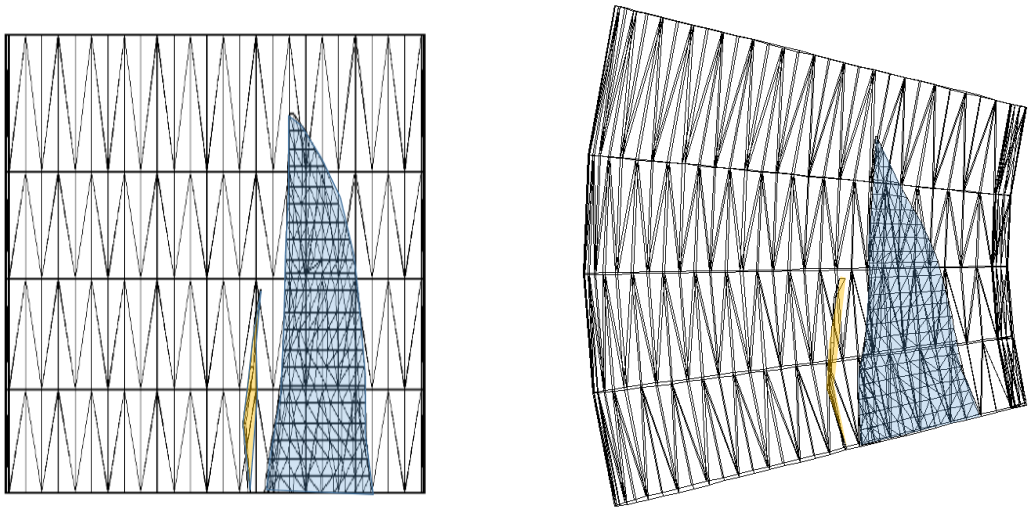

Fig. 5-9: Transformation of the model. (Left panel) 3-D model with shape outlines segmented from the cuboid image volume. (Right panel) Transformed 3-D model with outlines representing the real shape. The blue structure is part of the TM, and the yellow structure is part of the malleus.

5.7.5 Other challenges

One issue is that the original OCT acquisition does not cover the whole middle ear. Only about half of the TM is imaged (Fig. 5-10), which presents a challenge when registering the incomplete 3-D model from Doppler OCT images with the 3-D model segmented from the microCT images, which include the complete middle ear.

A second issue is that the TM in the OCT images appears to have an abnormally large thickness. Fig. 5-11 shows an example of B-mode cross-section of the TM. The original acquisition setting has 330 pixels in its 10 mm length, so one pixel is 0.03 mm. The thickness of the TM appears to be ~15 to 20 pixels by visual estimation in the OCT images, which corresponds to ~450 to 600 μm. Considering the refractive index of the soft tissue to be 1.4, the corrected thickness becomes 300 to 400 μm, which is still about three times thicker than the average TM. This issue is presumed by Dr. Adamson to be

related to certain settings in the Doppler OCT system or to the state of the TM, but the actual reason is not yet clear.

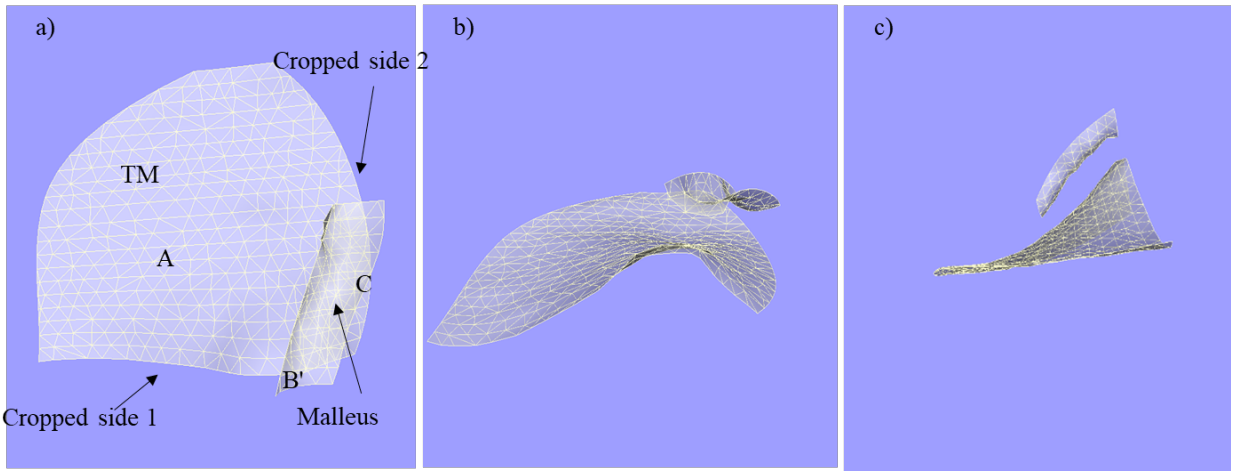

Fig. 5-10: The 3-D model reconstructed from OCT images. The model only includes part of the TM and part of the malleus.

Fig. 5-11: Zoomed-in Doppler OCT B-mode image with a cross-section view of the TM and part of the malleus.

Chapter 6

Model definition and verification

6.1 Introduction

In this chapter, the approximations made in our middle-ear model are presented in Section 6.2. Section 6.3 introduces the creation of models of the human middle ear for different FE solvers and the resulting comparison between the solvers. The boundary conditions, material properties and mesh resolution are defined in Sections 6.4 and 6.5, respectively. Section 6.6 presents the baseline material properties. Convergence testing is presented in Section 6.7. The software performance is summarized in Section 6.8.

6.2 Model approximations

The human middle ear is a very complex system. Therefore certain model approximations have been made in this study to derive tractable models:

1) The TM is represented by a single layer, composed of shell elements, which is considered to have uniform thicknesses within the PT and within the PF.

2) The soft tissue connecting the TM and malleus (TMMC) is represented as a solid structure with uniform material properties.

3) The ossicles are assumed to have uniform material properties.

4) The malleus and incus are assumed to rotate around a fixed axis of rotation.

6.3 Finite-element software

In this study, different models of the human middle ear were created for two FE solvers, SAP IV and Code_Aster (version 12.7). Once the original model is built, it can be output to different formats using Fad as described in Section 5.7 for simulation in the different FE solvers. The formats for which Fad exports tetrahedra include .sap (SAP IV), and .mail (Code_Aster).

Certain adjustments were required after exporting from Fad. This was done using the Mesh module for Code_Aster. The pre-processing for SAP IV was done by editing the .sap text file directly. For this thesis, the adjustments included modifying the boundary conditions of the spring connection which represent the connection between the footplate and oval window, and defining the damping and the dynamic sound pressure input. This step ensures that the model inputs to Code_Aster and SAP IV have the same geometry, material properties, boundary conditions and loading conditions. In that case we can evaluate whether our assumptions were correctly implemented in our models and check the consistency of our model responses from the two different solvers. These solvers were used in several previous studies in our group for static and dynamic analysis of middle-ear mechanics (e.g., Code_Aster by Maftoon et al. (2015); Motallebzadeh et al. (2017b) and Choukir (2017); and SAP IV by Mikhael (2005) and Elkhouri et al. (2006)).These solvers have proven to be generally robust and well supported. FE solver performance will be discussed further in Section 6.8.

6.4 Geometry and model components

The FE model developed in this study is depicted in Fig. 6-1. The mesh visualization and modification were done in Salome_Meca V2016. This model includes shell representations of the TM (PF and PT) and solid representations of the ossicles, TMMC and ISJ.

The TM was modelled with the seven-node second-order triangle shell elements (TRIA7) in Code_Aster. Each triangle element has three nodes at the vertices, three nodes at the middles of the

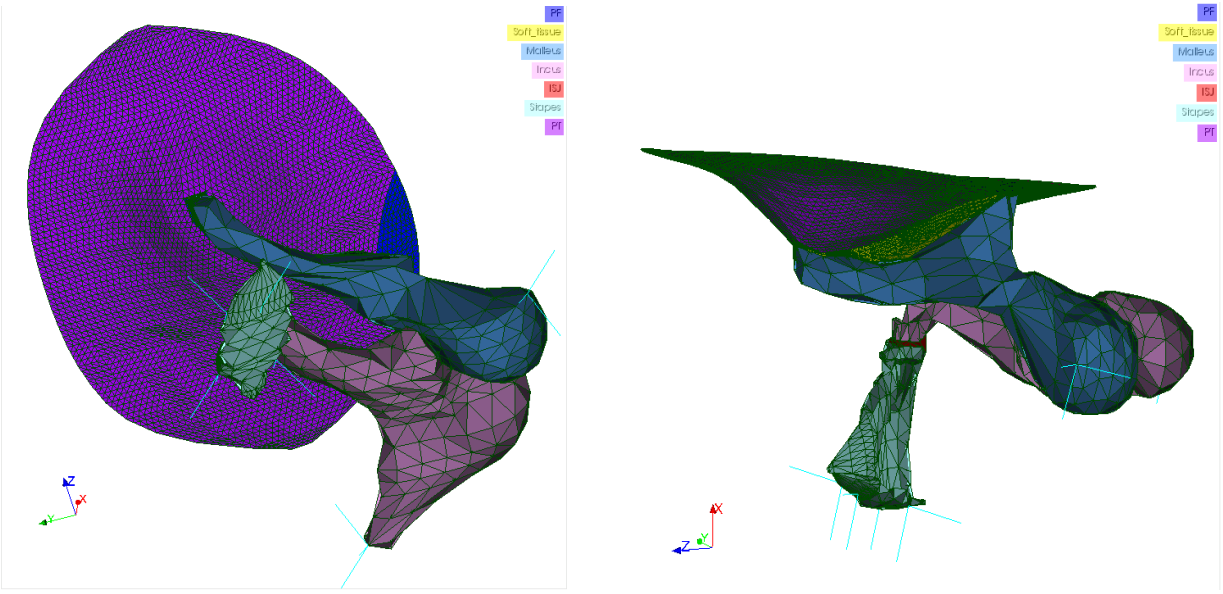

Fig. 6-1: Reconstructed 3-D model of human middle ear used in finite-element analysis (Salome_Meca). Left: Lateral view of FE model. Right: Medial view of FE model. The different structures are colour coded. The yellow lines represent spring elements corresponding to the soft tissues and the cochlear load. (Dark blue: PF; yellow: TMMC; light blue: Malleus; pink: Incus; red: ISJ; light blue: Stapes; purple: PF)

three edges, each of the six nodes having three translational and three rotational DOFs. There is a seventh node in the centre of the triangle which has only three rotational DOFs. In SAP IV, only linear elements are available, with each of the three nodes possessing six DOFs. The solid structures were modelled in Code_Aster with the ten-node tetrahedral elements (TETRA10). This element type has only three translational DOFs for each node. In SAP IV, only four-node linear tetrahedral elements are available, with three DOFs for each node.

In our model, a shared surface between the shell elements of the TM and the 3-D solid elements of the TMMC creates the correct coupling between the shell elements and the 3-D solid elements. In this case, the load as a uniform pressure can be applied to the shell elements.

6.5 Boundary conditions

The boundary between the PF and the PT was determined by observation of the thickness change on the cross-section microCT images. There is ambiguity due to the limited image resolution. It is also difficult to determine where the exact boundaries are between the TM and the surrounding annular ring based on the microCT images. Since the annular ring was omitted from our model, the TM was set to be fully clamped (i.e., all of the six DOFs were set to zero) at its endpoints to represent the boundary condition of the annular ring.

The anterior mallear ligament (AML) and the posterior incudal ligament (PIL) are each attached to the cavity wall to form the suspension of the malleus and incus in the middle-ear cavity. For simplicity, each ligament is modelled here as three very stiff springs in orthogonal directions. This formulation causes the malleus-and-incus block to rotate about an almost-fixed rotation axis.

The stapes annular ligament was modelled with eight springs, shown as yellow lines in Fig. 6-1. Four springs (again, two at the ends of the footplate long axis and two at the ends of the footplate short axis) were aligned parallel to the footplate. The other four springs were aligned parallel to the piston-motion direction (again, two at the ends of the footplate long axis and two at the ends of the footplate short axis). There are four dashpots, attached to the footplate in the same locations as the springs, which serve as the cochlear load. For the eight springs and four dashpots, the endpoints which do not have physical connections to the structures are fully clamped. This method of modelling the annular

ligament and the cochlear load was previously described by Maftoon et al. (2015) for a gerbil middle-ear model.

6.6 Baseline material properties

To choose the baseline material-property values for the model, a detailed survey of published models was conducted. After selecting the starting baseline values, each value was changed within a defined range to determine the impact on the simulation results. Such a sensitivity analysis helps us develop a better understanding of the importance of those values in building the model.

When looking at material properties, the first distinction that has to be made is whether or not the materials are behaving linearly. As discussed in Section 4.4.4, in our study the applied pressure is 2 Pa (100 dB SPL) and would certainly not cause large enough deformations to push the system into the non-linear range. Therefore, in this study the material properties are assumed to be linear.

A Poisson ratio of 0.3 has been chosen as used in many previous studies (e.g., Funnell & Laszlo, 1982; De Greef et al., 2017). It has been suggested that the soft tissue should have a higher Poisson ratio, approximately 0.5, because it is nearly incompressible. However, Maftoon et al. (2015) showed in sensitivity analyses that the Poisson ratio had quite small effects on the behaviour of their model of the middle ear. Therefore 0.3 was chosen as the Poisson ratio baseline value for all the components of the model in this study.

6.6.1 Pars tensa and pars flaccida

The baseline material properties of the TM were taken from a previous human middle-ear model (De Greef et al., 2017). The PF was given a Young's modulus of 6.7 MPa and a uniform thickness of 200 μm. For the PT, the Young's modulus and thickness were set to 20 MPa and 81 μm, respectively.

6.6.2 Ossicles

In this study, the material properties of the malleus, incus and stapes were taken from De Greef et al. (2017). The Young's modulus was set to 14.1 GPa. This value is considered as typical for bones and makes them practically rigid.

6.6.3 Soft tissue and joints

The Young's modulus of the soft-tissue TMMC was taken to be 2 MPa, assuming that the composition of this structure is similar to those of other middle-ear ligaments and that the material properties of this connection are uniform (Funnell, 1996; De Greef et al., 2017). The Young's modulus of the ISJ was taken to be 6 MPa (De Greef et al., 2017).

6.6.4 Annular ligament

There have been many studies measuring the material properties of the annular ligament. Gan et al. (2011), for example, measured the mechanical properties of the human stapedial annular ligament using a micro-material testing system combined with digital image correlation. The results demonstrated that the stapedial annular ligament is a viscoelastic material with a nonlinear stress-strain relationship. However, this study focuses on the linear case and the nonlinearity is not relevant here.

For simplicity, this model used springs to represent the annular ligament and the stiffness of the springs is required. One way to estimate the spring stiffness is to use the formula

$$K = \frac{AE}{l}$$

where A represents the approximate surface area of the ligament, E is Young's modulus, and l is the approximate thickness of the ligament. Hagr et al. (2004), for example, used this method to estimate the stiffness by dividing the annular footplate ligament into different bundles and measuring the sizes of the bundles to get the stiffness values. For each bundle, the stiffness was represented by two spring

elements (perpendicular and parallel to the footplate). However, due to the image resolution, it was hard to estimate the size and the boundary of the annular ligament in this study. Another approach is to measure the stiffness of the annular ligament through experiment. Kwacz et al. (2015), for example, used atomic force microscopy to measure the elastic properties of annular ligaments in two cadavers. The measurements represent the elastic properties of the annular ligament in the direction perpendicular to the footplate. They found that the stiffness of one annular ligament was 115.8 N/m and that of the other one was 124.6 N/m. We have assumed a stiffness of 120 N/m in both directions (parallel and perpendicular to the footplate). Therefore, each of the horizontal and the vertical springs was set to 30 N/m (four springs for each direction).

6.6.5 Cochlear load

Gan et al. (2004) implemented the cochlear load with ten dashpots attached between the stapes footplate and the fixed bony wall. The damping coefficient of each dashpot was calculated as 0.02 Ns/m. Their assumption of the cochlear load was based on a circuit-model calculation for effective mass of the cochlear fluid (e.g., Zwislocki, 1957; Lutman & Martin, 1979) and experimental studies of cochlear impedance in human temporal bones (Merchant et al., 1996; Aibara et al., 2001). Measurements in gerbil ears (e.g., Decraemer et al., 2007; Ravicz et al., 2008) suggest that the cochlear load generates purely viscous damping over most of the frequency range from 0.2 to 20 kHz. De La Rochefoucauld et al. (2008) derived an average cochlear input impedance of about 4×10^{10} Pa·s/m³ for frequencies less than 30 kHz with a stapes footplate area of 0.62 mm² in gerbil. This corresponds to a viscous damping coefficient of 15.4×10^{-3} N·s/m³. Maftoon et al. (2014) uniformly distributed this value to four dashpots perpendicularly attached to the stapes footplate to represent the cochlear load. In our convergence test and sensitivity analysis, we defined the cochlear load in the same way as in Maftoon's

gerbil model in Code_Aster. SAP does not have the ability to define the cochlear load in this way. However, for the simulations at low frequencies, it does not matter whether there is a cochlear load or not.

6.7 Convergence test

In Fie, the original mesh-resolution parameter *ires_xy* was chosen to be 20 elements/diameter, and the z-resolution (*ires_z*) was chosen to be 1 (i.e., every slice included). The same values were chosen for the TM, ossicles and joints.

As mentioned in Section 4.2, once the model with baseline material properties and boundary conditions is built, a mesh-convergence test is essential to understand the relationship between the mesh resolution, the computing time and accuracy. Increasing the mesh resolution should result in an asymptotic increase in the accuracy, but also in an increase in the computing time.

The first model, with *ires-xy* = 20 elements/diameter, contains 500 triangular elements and 3132 tetrahedral elements. For validation, the displacement of certain fiducial nodes were chosen from each model for comparison. The fiducial nodes included the umbo, a node from the posterior TM with maximal displacement, and a node on the stapes. It is important to make sure the fiducial nodes are taken from the same locations on each model.

Starting with the first model, we used the Homard utility (https://www.code-aster.org/V2/outils/homard/en/) to further refine the mesh. Homard is a built-in module in Salome-Meca which is designed to refine or coarsen the meshes of a FE model without changing the geometry of the model. Homard splits one triangle shell element into four sub-triangles and a tetrahedral element into eight sub-tetrahedra. Homard can refine a mesh iteratively based on a user-defined “hypothesis”, or strategy. Three types of hypothesis can be used: (1) uniform refinement over the whole mesh; (2) refinement

according to a field which can be pre-defined to include certain components that need to be refined; and (3) refinement according to the geometrical zone such that the user can define whether or not to refine each component within the model. In this study, we used the third hypothesis to refine our models. Homard does not change the positions or numbering of the existing nodes. For two joined objects with a shared surface, the surface will be refined for both objects to ensure the right connection. These two features keep the consistency between the original and refined models. The convergence analysis was conducted by refining the meshes until a less-than-2% variation of displacements of the three fiducial nodes was obtained from one iteration to the next, or until the simulation reached a computational limit (e.g., running out of memory).

For comparison, both linear and bi-quadratic meshes were used. Fig. 6-2 presents the simulation results for the three fiducial nodes located in the posterior region of the TM, at the umbo and on the stapes. The first two models generated using the Homard function had only the elements on the TM and TMMC refined while the mesh resolution on the other structures stayed the same. At the third iteration, the computational limits were exceeded so finally we only refined the TMMC on the third iteration while keeping the mesh resolution of the TM and the rest of the structures unchanged. The dashed lines show the results for the models composed of linear elements and the solid lines show the results of the models composed of bi-quadratic elements. The horizontal axis corresponds, from left to right, to the initial model generated in Fad and to the models with different numbers of Homard refinement iterations. When comparing the models with the same mesh resolution, the models with linear elements always generated smaller displacements than the models with bi-quadratic elements did. The models with bi-quadratic elements converged faster than the linear-element models. For the point on the TM, the bi-quadratic model has a difference of less than 0.3% between the second and third iterations, while the linear mesh model continues to increase substantially, with a difference of 2.9%. Based on the

convergence test, for the final model, the TM was refined by two iterations in Homard and the soft-tissue connection was refined by one iteration. The mesh resolution of other structures (ossicles and joints) were also tested but the influences were negligible so the rest of the structures use the initial resolution with *ires-xy* = 20.

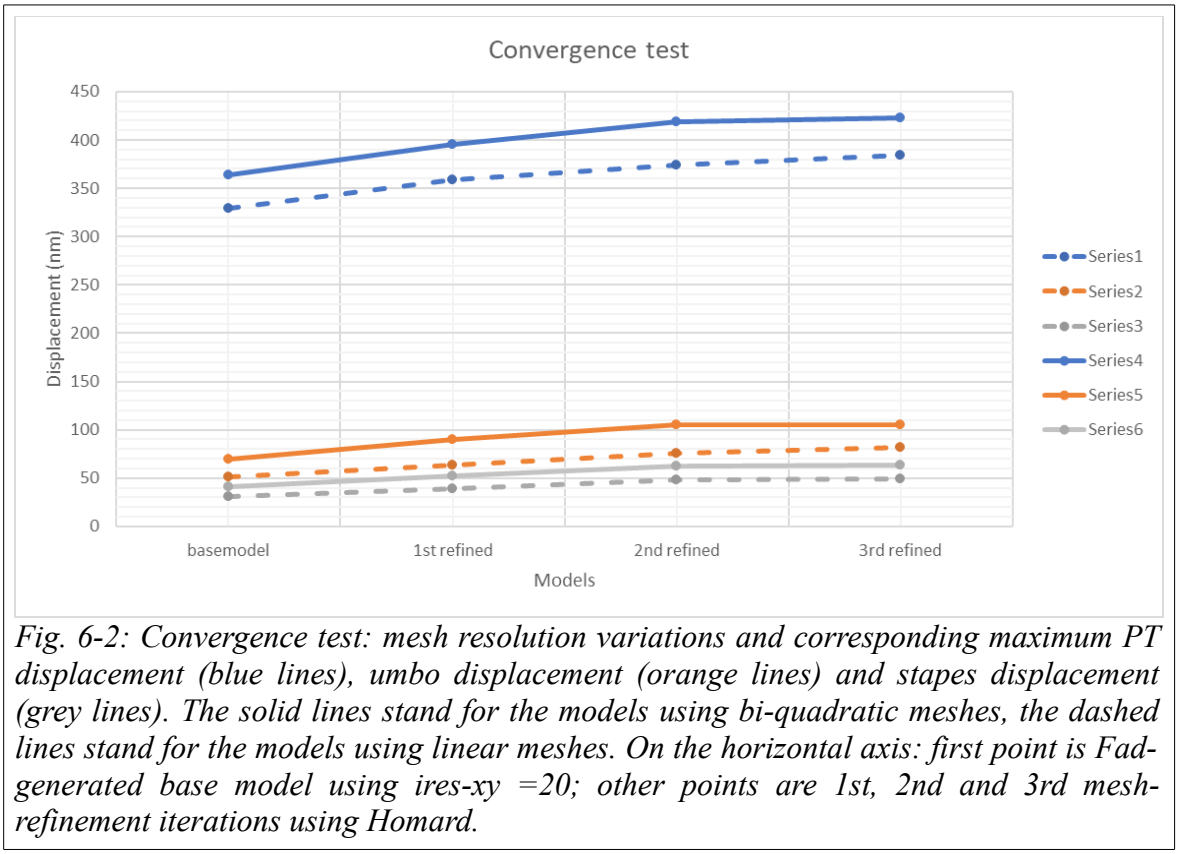

Fig. 6-2: Convergence test: mesh resolution variations and corresponding maximum PT displacement (blue lines), umbo displacement (orange lines) and stapes displacement (grey lines). The solid lines stand for the models using bi-quadratic meshes, the dashed lines stand for the models using linear meshes. On the horizontal axis: first point is Fad-generated base model using ires-xy =20; other points are 1st, 2nd and 3rd mesh-refinement iterations using Homard.

6.8 Finite-element software performance

For model verification, two different FE solvers, SAP IV and Code_Aster, were tested and the results were compared. This step ensures that different solvers provide the same results for the same material properties and loading conditions, to increase our confidence that the software implements our model correctly. The results of different solvers can be validated against analytical solutions by using structures with simple geometry (e.g., a flat rectangular plate) and boundary conditions (fully clamped

(FC) or simply supported (SS)). The square plate was generated in Fad using triangular shell elements. The dimension was 10×10 mm and the thickness was 75 μm. The plate was isotropic elastic (E = 40 MPa, υ = 0.3) with a uniform pressures of 1 Pa applied. Fad outputs the plate with linear elements as the input for SAP IV and Code_Aster. The linear shell elements were then converted to bi-quadratic elements in Code_Aster. Homard was used for refining the bi-quadratic elements with 2 iterations. The simulation results are summarized in Table 6-1.

Boundary condition	FE solvers	Element Type	Displacement (m)	Mesh refinement
FC	SAP		8.13E-06	
	Code_Aster	Linear element	8.53E-06	
			8.28E-06	Homard iteration 1
			7.81E-06	Homard iteration 2
		Bi-quadratic element	7.81E-06	
			8.14E-06	Homard iteration 1
			8.19E-06	Homard iteration 2
	Analytical solution		8.18E-06	
SS	SAP		2.59E-05	
	Code_Aster	Linear element	2.631E-05	
			2.629E-05	Homard iteration 1
			2.628E-05	Homard iteration 2
		Bi-quadratic element	2.57E-05	
			2.63E-05	Homard iteration 1
			2.65E-05	Homard iteration 2
	Analytical solution		2.62E-05	

Table 6-1: Square-plate convergence test results compared with analytical solutions.

Fig. 6-3 and Fig. 6-4 show the magnitudes of the maximum displacements of the FC and SS plates, respectively. For the FC plate, the displacements of the linear-element model in Code_Aster were about 4% higher than the analytical solution with the original mesh resolution. When the mesh resolution was increased, the displacements decreased. After the second iteration of Homard, the displacement was ~4.9% lower than the analytical solution. The bi-quadratic model approached the analytical solution when the mesh resolution was increased; the difference started from 4% and decreased to 0.1% with the

second iteration. SAP IV came within 4.9% of the analytical solution even with its linear elements and the coarsest mesh.

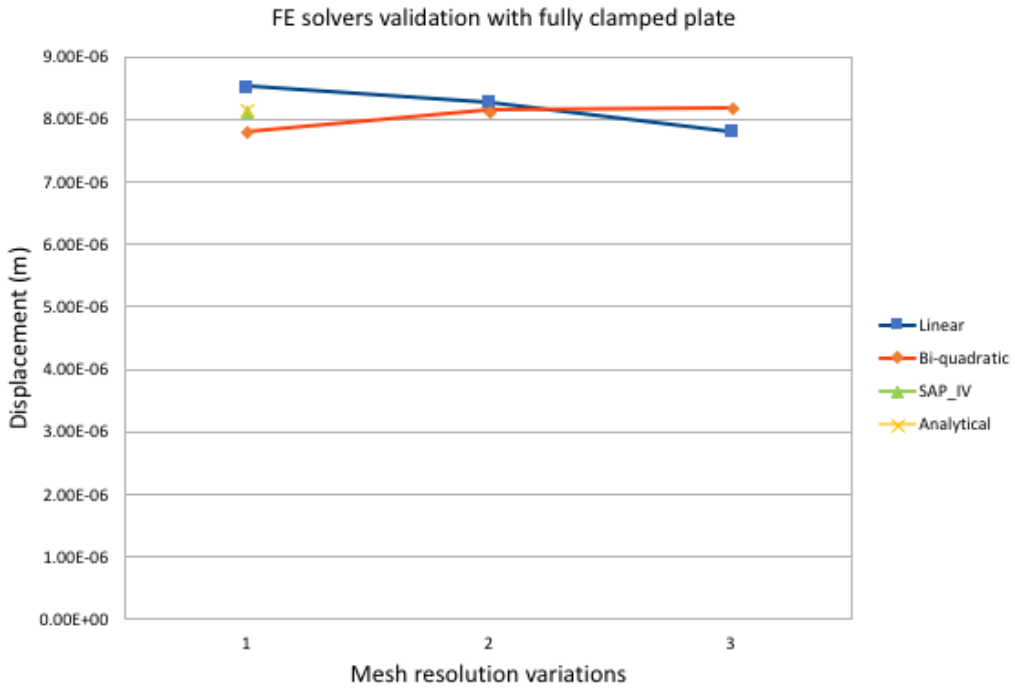

Fig. 6-3: Convergence of displacement of fully clamped square plate. For the x axis, 1 stands for original model, and 2 and 3 stand for 1st and 2nd iterations of mesh refinement using Homard. The blue and red lines are for the models using linear and bi-quadratic elements, respectively, in Code_Aster. The yellow point is the result from SAP IV, and the green point is the analytical solution.

For the SS plate, in Code_Aster the bi-quadratic model approached the analytical solution when the mesh resolution was increased and the result with the second iteration was different by 1.2% from the analytical solution. The displacement for the linear-mesh model is 0.3% higher than the analytical solution. SAP IV gives a 1.1% difference from the analytical solution.

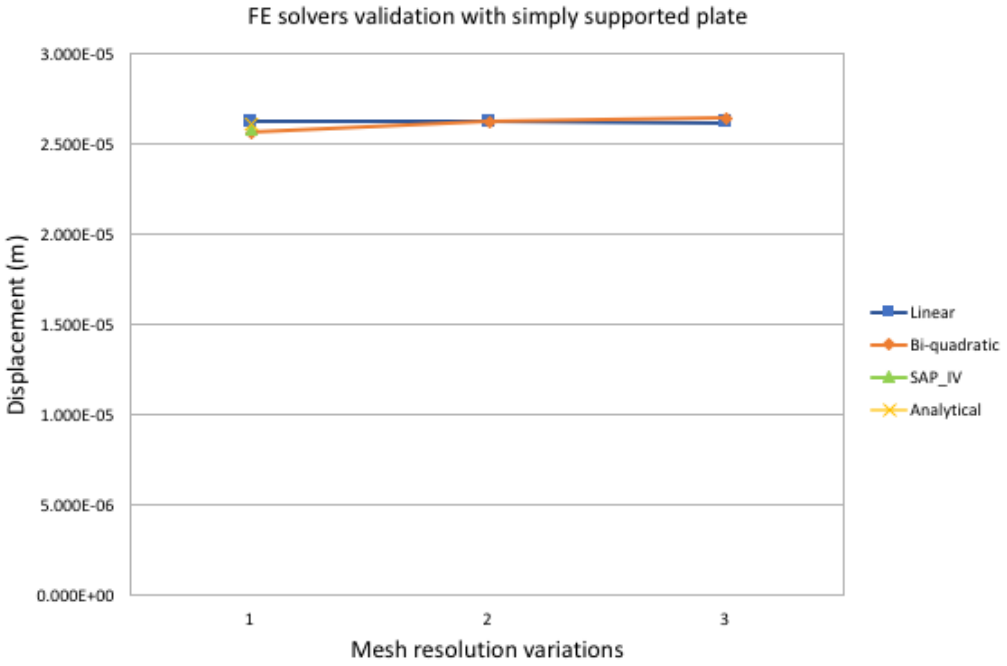

Fig. 6-4: Convergence of displacement of simply supported square plate. For the x axis, 1 stands for original model, and 2 and 3 stand for 1st and 2nd iterations of mesh refinement using Homard. The blue and red lines are for the models using bi-quadratic and linear elements, respectively, in Code_Aster. The yellow point is the result from SAP IV, and the green point is the analytical solution.

For both the FC and SS plate tests, the displacement of the linear-mesh model was larger than that of the corresponding bi-quadratic model, and for the SS case the linear Code_Aster model actually performs as well as or better than the refined bi-quadratic models. These observations are somewhat unexpected but the differences were small, and tests on the complete middle-ear model showed the expected behaviour.

Based on these tests, the bi-quadratic elements were adopted for use in the rest of this study. Both SAP IV and Code_Aster are found to be reliable FE solvers when simulating with shell structures.

Chapter 7
Results

7.1 Introduction

In this chapter, the simulation results for both the static (low-frequency) and dynamic simulations of the middle ear are presented. We established estimates of parameters based on a previously validated linear model (Mikhael et al., 2004). We then simulated the middle ear in response to various loading conditions and compared the results with the Doppler OCT experimental measurements. With these initial material properties, however, our model was too stiff, with the maximal displacement in the experimental data being about 7 times as high as the simulation result. Therefore, we then adopted the material properties from DeGreef et al. (2017), and the results with those parameters are presented in the following sections.

Sensitivity analysis is presented in Section 7.2. Displacement maps of low-frequency results are shown in Section 7.3. The dynamic results with step pressure and sinusoidal pressure are presented in Sections 7.4 and 7.5, respectively. The results are compared with our Doppler-mode OCT experimental data and with results from previous models in Section 7.6. A comparison between the 3-D model segmented from the micro-CT images and the model segmented from the Doppler OCT images is presented in Section 7.7.

7.2 Sensitivity analysis

A sensitivity analysis is essential to understand the relative influences of some factors on middle-ear mechanisms due to the wide range of possible choices made when defining the model. The sensitivity analysis is also valuable, for example, in guiding the modification of the model if necessary to bring the

simulated responses into better agreement with the experimental data. The sensitivity analysis here only considers the effects of the material properties and not those of the geometry. The effects of changing geometries have occasionally been studied in the previous literature. For example, substantial effects of changing TM shape were reported by Funnell and Decraemer (1996).

The FE model is composed of seven structures, including PT, PF, TMMC, malleus, incus, ISJ and stapes; eight springs representing the stapes annular ligament (four parallel and four perpendicular to the footplate) and another six springs representing the ligaments connecting the malleus and incus to the temporal bone. The sensitivity of the model to various parameters (Young's modulus (E) of PT, PF, TMMC, ossicles and ISJ; Poisson ratio (PR) of PT, PF, TMMC, ISJ and ossicles; thickness of PT and PF; and the stiffness of the stapes annular ligament parallel and perpendicular to the footplate) were tested. In this study, the baseline values of parameters were varied by +10% and −10% from their baseline values. The results were evaluated by comparing the displacement changes at the umbo and at a node in the posterior region of the PT, where the largest displacement of the TM is expected. The results are presented in Figs. 7-1 and 7-2, respectively.

The responses of the posterior region of the TM change by 14% to 19% when the thickness of the PT is increased or decreased by 10%, and by 9% to 11% when the Young's modulus of the PT is increased or decreased. The responses at the umbo change by 9% to 10% when the thickness of PT is increased or decreased by 10%, and by 6% to 7% when the Young's modulus of the PF is increased or decreased.

In summary, the two most influential parameters are the thickness and Young's modulus of the PT. The next most influential parameters are the Young's modulus of the TMMC and the thickness of the PF, which have noticeable effects on the displacement of the umbo but almost no effect on that of the PT. The effects from the rest parameters are negligible, all being less than 1%.

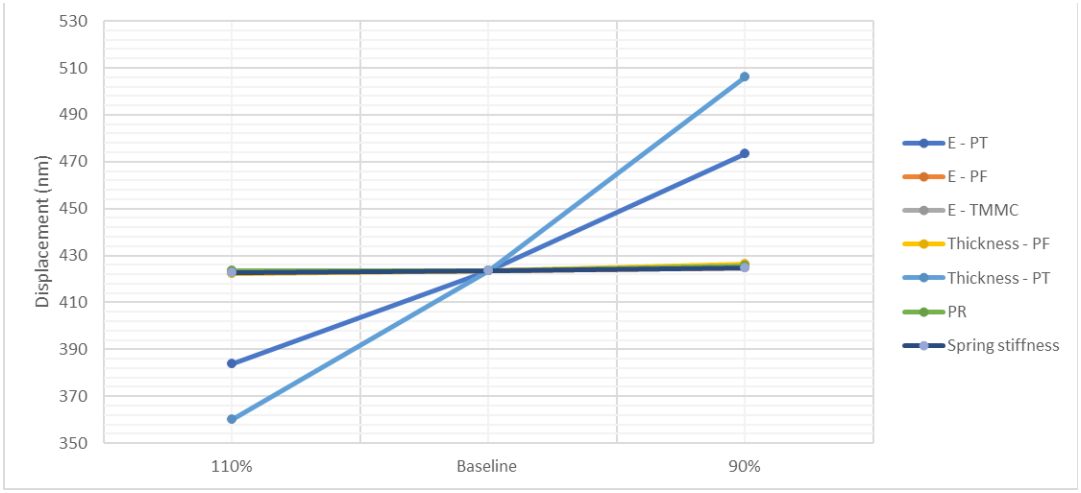

Fig. 7-1: Sensitivity analysis by taking +110%, 100% and 90% of the baseline values. The lines with different colours represent the displacement changes of the posterior region of the PT (in nm) corresponding to the changes of a certain material property (Young's modulus of PT, PF, TMMC; thickness of PT and PF; Poisson ratio; and spring stiffness representing the footplate annular ligament).

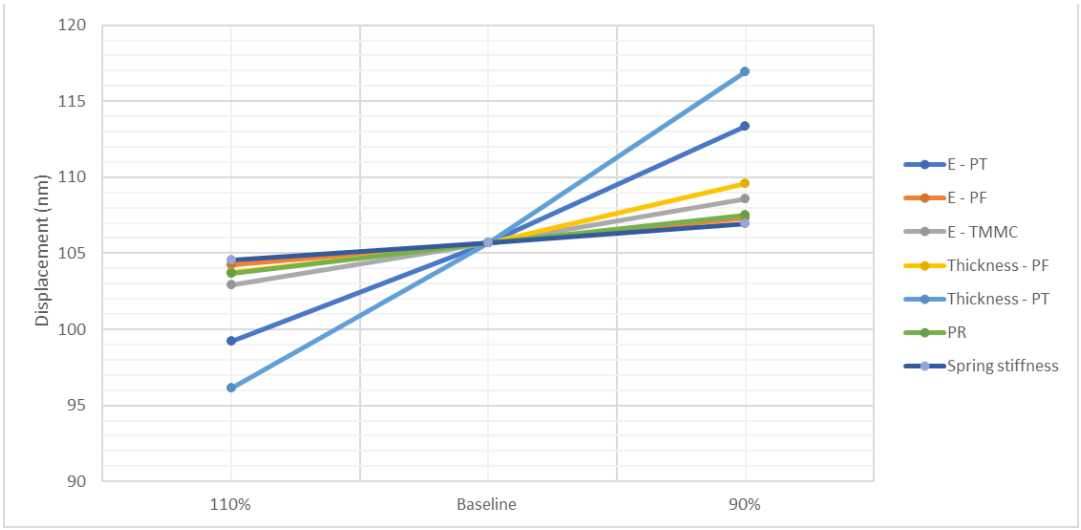

Fig.7-2: Sensitivity analysis by taking +110%,−100% and 90% of the baseline values. The lines with different colours represent the displacement changes of the umbo (in nm) corresponding to the changes of a certain material property (Young's modulus of PT, PF, TMMC; thickness of PT and PF; Poisson ratio; and spring stiffness representing the footplate annular ligament).

7.3 Low-frequency results

In this section, a static model of the middle ear was used to simulate the response to a low-frequency probe-tone input. The simplification is that the damping and inertia are not included in the model. This is a reasonable approximation for comparison with the 500-Hz OCT data. Two FE solvers (Code_Aster and SAP IV) were used for the simulation.

Once the proper boundary conditions and material properties had been put in place, Code_Aster was used to perform the simulations with a middle-ear model having a mesh resolution chosen based on the convergence test (Section 6.7). Sample displacement results can be seen in Fig. 7-3. As expected, the displacements are maximal in the posterior region of the TM (169 μm/Pa). The other, smaller displacement maximum on the TM is in the anterior region. The maximum manubrial displacement, which is 36 μm/Pa, is at the umbo as expected. Smaller displacement are seen on the rest of the malleus and on the incus, the ISJ and the stapes. The maximal displacement on the stapes footplate is 26 μm/Pa.

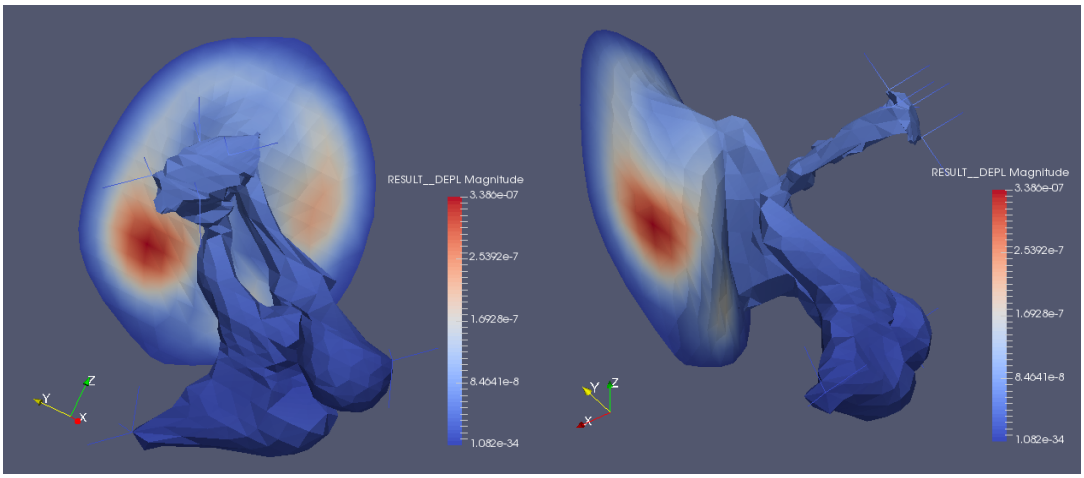

Fig. 7-3: Middle-ear static simulation results from Code_Aster. Left: Medial view. Right: Posteromedial view. The displacements are greatest in the posterior region of the TM.

SAP IV was also used to perform simulations with the model. Fig. 7-4 shows two different anatomical views of the magnitudes of the middle-ear displacements. The simulated displacement pattern of the TM here matches well with the result from Code_Aster. The maximal displacement again appears in the posterior region, with a magnitude of 151.3 μm/Pa, 10.6% less than with Code_Aster. The displacement at the umbo is 33.8 μm/Pa and the maximal displacement at the stapes is 29.5 μm/Pa, 6% less and 11.8% more than with Code_Aster, respectively.

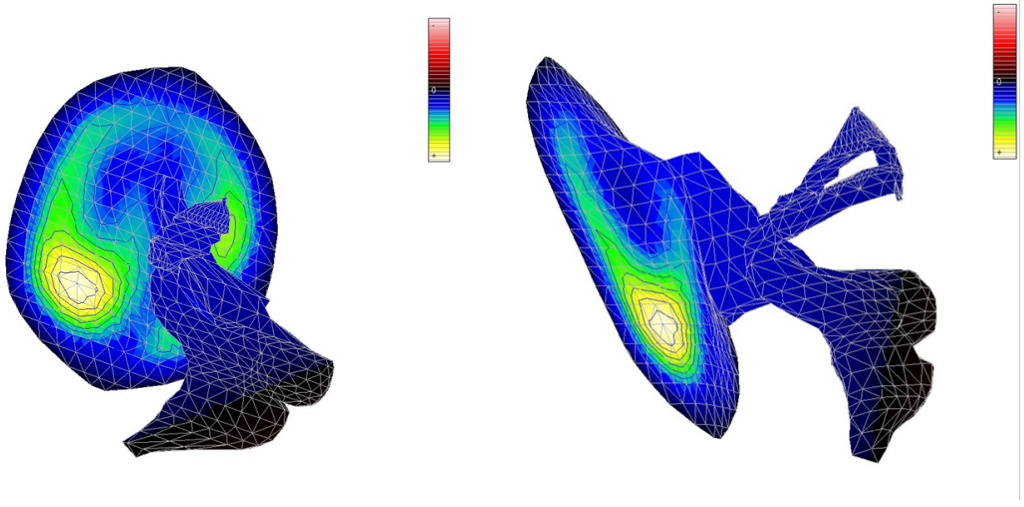

Fig. 7-4: Middle-ear static simulation results from SAP IV. Left: Medial view. Right: Posteromedial view. The displacements are again greatest in the posterior region of the TM.

Fig. 7-5 shows displacement vectors for a posteromedial view of the middle ear. The malleus and incus can be seen to rotate about the axis of rotation that extends from the location of the posterior incudal ligament to the anterior portion of the mallear head. The displacement vectors at the footplate are approximately normal to the surface, implying a predominantly piston-like motion of the stapes. Also, the angles of the displacement vectors change between the incus and the stapes, indicating relative motion of the bones due to the ISJ.

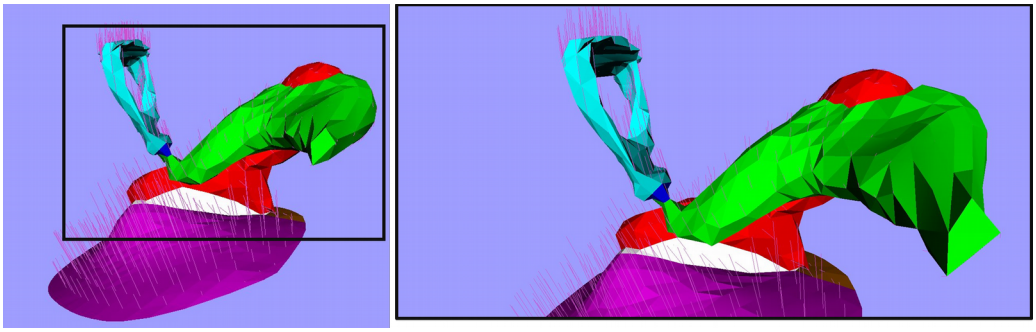

Fig. 7-5: A model of the middle ear (posteromedial view) with displacement vectors showing malleus and incus rotation about a fixed classical axis. Left: Complete view; Right: Zoomed-in section focusing on the changes in the displacement vectors on the ossicles. Predominantly piston-like displacements at the footplate can also be seen.

7.4 Dynamic results

7.4.1 Loading conditions and time-step analysis

To compute the frequency response of our middle-ear model, we applied a step sound pressure of 2 Pa on the TM surface and performed a transient FE analysis. The derivative of the system's step response is its impulse response, and the Fourier transform of the impulse response results in the frequency response. Therefore, the step function allows for the responses to be calculated at each of the frequencies of interest using the result of a single simulation. All the displacements in the following figures are plotted as the component parallel to the *y* axis (i.e., perpendicular to the plane of the annulus of the TM), which shows the largest displacements among the three axes, the displacements parallel to the *x* and *z* axes being very small. The response of our model was compared to the model of DeGreef et al. (2017).

A doubling of the time span of the simulation (from 10 to 20 ms) changed the responses by less than 0.3 dB. The time span of 20 ms was used in order to get a higher frequency resolution, 25 Hz instead of the 50 Hz that 10 ms would give.

The choice of the time step is crucial and controls the highest frequency content that can be obtained. Fig. 7-6 shows the effect of the size of the time step in Code_Aster on the frequency response of a point in the posterior region, with time steps of 50, 25 and 10 μs. For frequencies below the resonance at 1.5 kHz, an increase of less than 1 μm/Pa in magnitude was observed as the time step increased. Above 5 kHz, however, compared with the results for the smallest time step (10 μs), the curves for the two larger time steps display discrepancies of up to 6 dB at 7 kHz. As a trade-off between accuracy and length of computation time, we chose a time step of 25 μs for our simulations for this loading condition. The difference is negligible for the frequency of immediate interest, 500Hz, and is small even for the frequencies of 1 and 2 kHz at which our more recent OCT measurements were made.

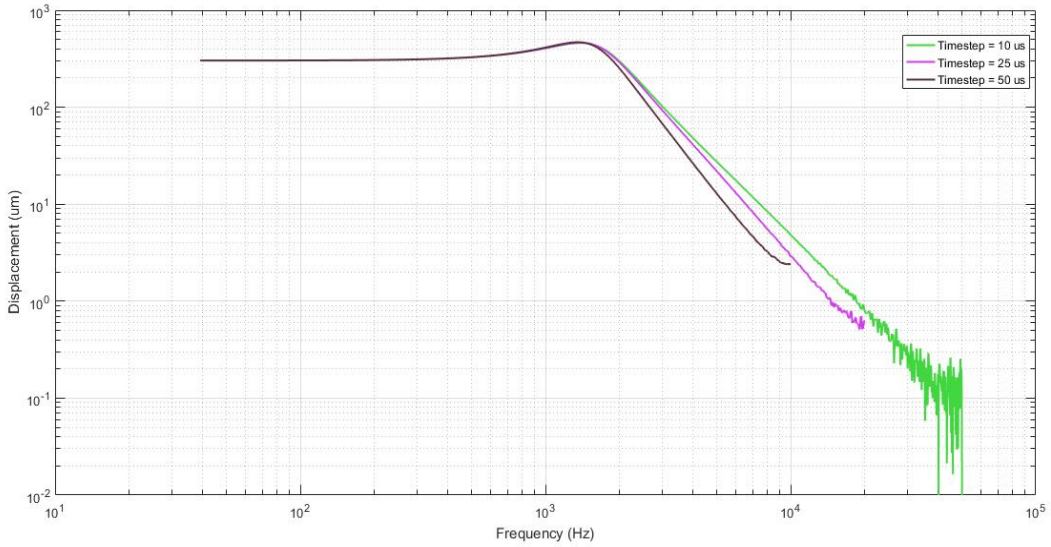

Fig. 7-6: Simulations with constant time span (20ms) but different time steps (10, 25 and 50 μs).

Figure 7-7 shows the *y* components of the model displacement responses in the time domain for the same point in the posterior region in both SAP IV and Code_Aster in response to a step of sound pressure. In terms of computational cost, both solvers completed in less than 1 minute. The two FE

solvers produce very similar responses in the *y* direction and also in total magnitude. The maximum changes in displacement magnitude between the two solvers are less than 10%.

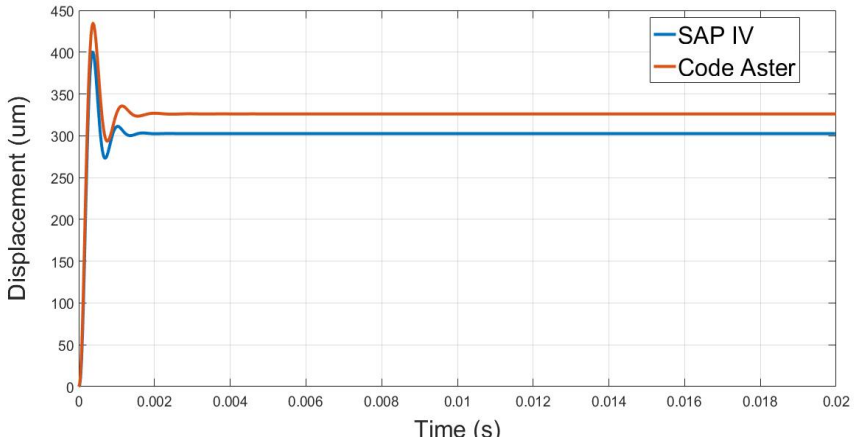

Fig. 7-7: Comparison of displacement magnitude in the y direction for a point in the posterior region of the PT, using SAP IV and Code_Aster. The overall differences between the two solvers are less than 10%.

Fig. 7-8 shows model responses in the frequency domain, and it can be seen that the two solvers match well. Changes of less than 8% (~0.7 dB) in magnitude were found for all frequencies between 0.1 and 10 kHz. The resonance frequencies are at 1200 Hz for Code_Aster and 1500 Hz for SAP IV. The main reason for the differences could be the different element types used in the models for these two solvers. SAP IV used linear elements and Code_Aster used bi-quadratic elements. The differences between the linear-element model and the bi-quadratic-element model is consistent with the convergence tests in Chapter 6. Since Code_Aster is able to use higher-order elements and also allows the definition of a cochlear load, subsequent simulations were conducted in Code_Aster unless stated otherwise.

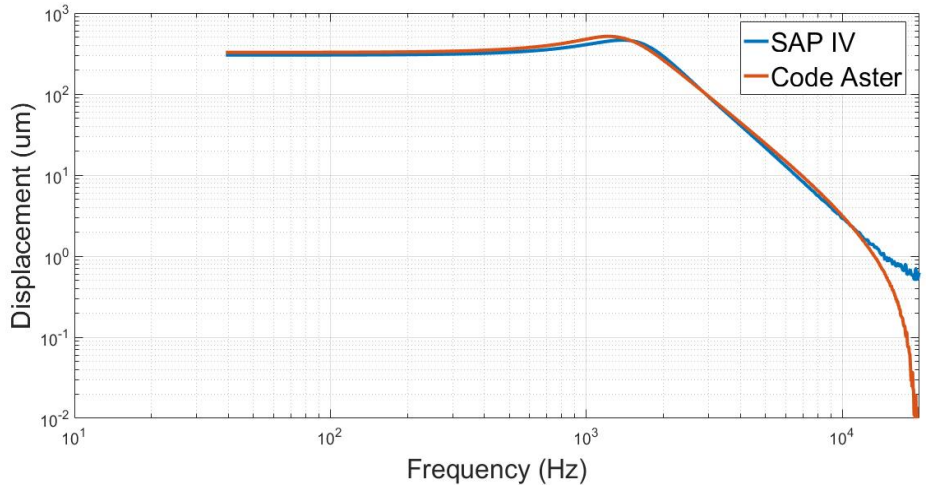

Fig. 7-8: Comparison of posterior PT displacement magnitude in y direction for SAP IV and Code_Aster. The overall differences between the two solvers are less than 8% up to 10 kHz.

7.4.2 Damping parameters and the cochlear load

Different damping parameters were tested to examine their effects on the responses of the posterior region. Many published middle-ear models employ Rayleigh damping. The baseline parameters for Rayleigh damping were chosen here to be the damping parameters of Gan et al. (2004) (α = 0 s^{-1}, β = 75 μs). We kept α = 0 s^{-1}, and took values of 5, 10, 25, 50 and 75 μs for β. Fig. 7-9 shows the model responses with the different damping parameters. The two lowest damping parameters result in sharp peaks and troughs in the model responses above the resonance frequency, while the two largest damping parameters result in very smooth curves.

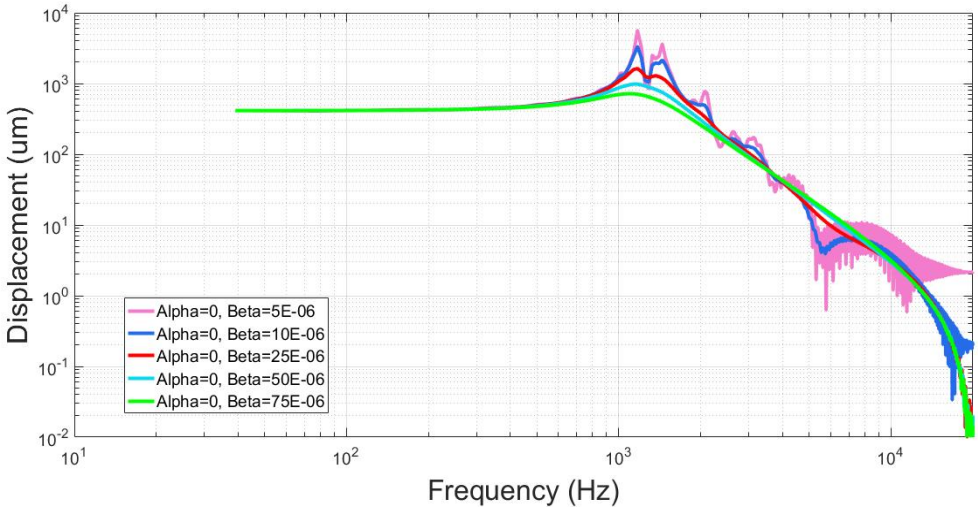

Fig. 7-9: Influence of damping variation. The curves represent the frequency domain responses of a node in the posterior region of the PT. As alpha is kept at 0, increasing beta smooths out the curves.

Additional testing of the damping parameters and cochlear load was performed to determine the appropriate settings for the model. The values were taken from the previous research of Gan et al. (2004), Gariepy (2011) and Maftoon et al. (2015). Gan et al. (2004) used the same Rayleigh damping parameters α and β for all materials of the human middle-ear system, namely $\alpha = 0\ s^{-1}$ *and* $\beta = 75\ \mu s$. The cochlear load was added to the stapes footplate with 10 dashpots attached between the stapes footplate and the fixed bony wall, which represented a damping impedance. The damping coefficient of each dashpot was 0.02 Ns/m^3. For our study, we have four dashpots to represent the cochlear load, so each dashpot was set to 0.05 Ns/m^3.

Typical human-body damping ratios lie in the range from 0.15 to 0.4, as cited by Gariepy (2011). The damping ratio is a function of α and β as introduced in Section 4.3. For his newborn human model, Gariepy used a constant damping ratio of 0.25, which is near the geometrical mean of 0.15 and 0.4, for his single-frequency sine-wave input pressures (500 to 2000 Hz). His values of α and β were therefore

different for different input sound frequencies. In this test, we kept α constant at 150 s^{-1}, as done by Gariepy (2011), and we set β to 3.7 μs to hold the damping ratio (within the frequency range from 0.05 to 2 kHz) at around 0.25.

For the gerbil model of Maftoon et al. (2015), they set $\alpha = 0$ s^{-1} and used different values of β for different structures: 2 μs for the structures with highly organized collagen fibres, 30 μs for the structures with abundant elastic fibres, and 0.2 μs for the ossicles. They tested models with and without the cochlear load to determine its effects. The cochlear load was modelled as four dashpots perpendicularly connected to the footplate and the value for each dashpot was taken as 0.00384 Ns/m^3. Code_Aster was used as the FE solver in this test. The models were tested with sound stimulus frequencies up to 10 kHz. One node was taken from the posterior region of the TM where the maximal displacement was expected. The magnitude of the displacements of this node from different simulations were compared and the results are presented in Fig. 7-10.

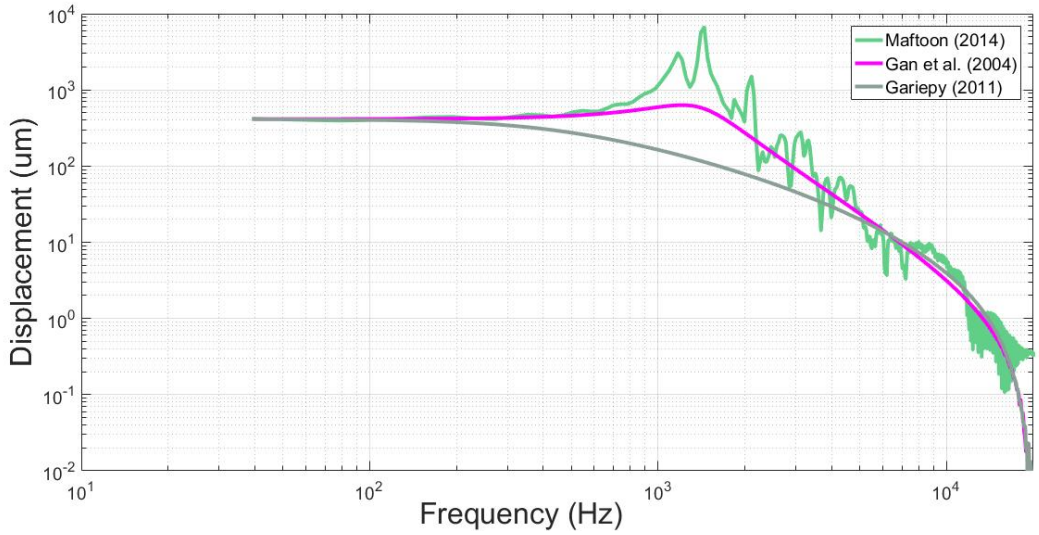

Fig. 7-10: Comparison of PT response with Rayleigh parameters and cochlear damping from Gan's model, Maftoon's model and Gariepy's model.

It is clear from Fig. 7-10 that the damping plays a major role in flattening the resonance of the TM. The damping has negligible effects at frequencies up to about 100 Hz. Our model using Maftoon's gerbil parameters is under-damped with two sharp resonances appearing between 1 kHz and 1.5 kHz. This is not consistent with experimental observations. Our model with Gariepy's parameters is over-damped, with no resonance peak appearing. The resonance frequency with Gan's parameters is around 1.4 kHz. Gan's Rayleigh parameters are also used in the model of De Greef et al. (2017). For Gan's Rayleigh values, the resulting damping ratio is 0.047 at 100 Hz, 0.47 at 1 kHz and 4.7 at 10 kHz. At the higher frequencies, the high damping ratio will "result in unrealistic TM vibration patterns that are over-damped and exhibit too few local maxima" (De Greef et al., 2017). However, for comparison with the OCT measurements we are not concerned with such high frequencies. In the following results, the Rayleigh parameters of Gan's model will be used unless otherwise stated.

The incorporated cochlear impedance has a strong influence on the motion of the stapes footplate, and it will affect the TM vibration as well. Fig. 7-11 shows the effects of the incorporation of a cochlear impedance on the vibrations of a point in the posterior region of the PT. The model incorporating the

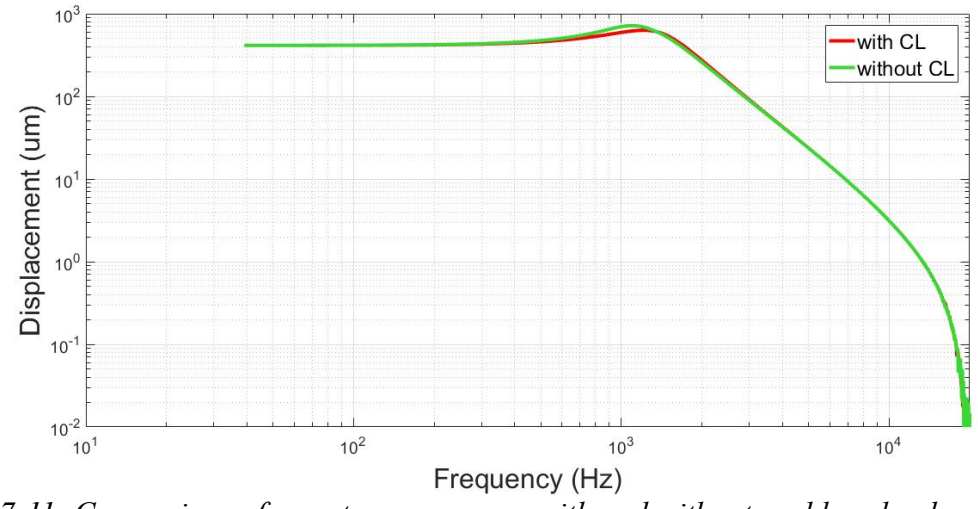

Fig. 7-11: Comparison of pars-tensa response with and without cochlear load.

cochlear impedance from Gan et al. (2004) is our base model and produces a peak at about 1.2 kHz. The other model, without the cochlear impedance, shows the resonance peak shifted to a slightly lower frequency (~1.1 kHz) and about 0.67 dB higher. The differences between the model responses appear from about 700 Hz to about 1.1 kHz. Dirckx and Decraemer (2001) showed that quasi-static eardrum displacement remained the same before and after moving the cochlea. For quasi-static displacements, the presence of the cochlear fluid does not impede the motion of the TM since the damping is velocity-dependent and there is no velocity of the round window.

7.4.3 Boundary conditions

Our base model assumes that both ends of the anatomical rotation axis of the malleus and incus are fixed. In this case, the connection of the ligaments on both the anterior mallear process and the posterior incudal process were considered as rigid with only three rotational DOFs allowed. However, it is clear that the ligaments, if present, would introduce more flexibility to the ossicles, and the rotation axis would change with increasing frequency. Fig. 7-12 shows the responses of a point on the PT with two different boundary conditions: (1) with fixed nodes on each side of the anatomical rotational axis; and (2) with three orthogonal springs on each side of the imaginary rotational axis which mimic the effect of suspensory ligaments in three-dimensional space. In the absence of good *a priori* estimates, the value of the spring stiffness was taken to be the same as what has been used in defining the stiffness of the springs representing the footplate ligament (30 N/m).

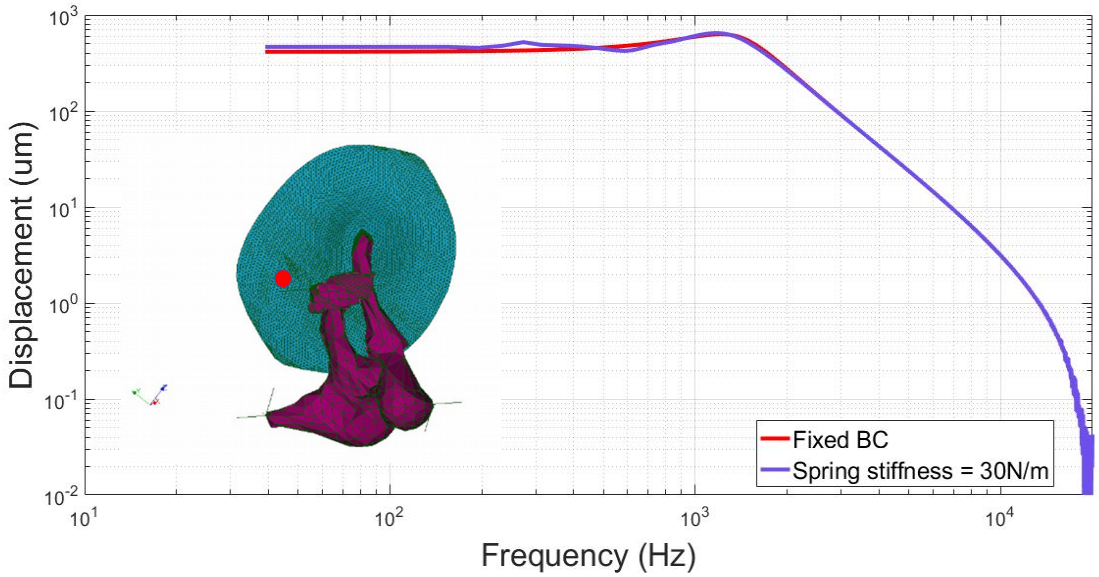

Fig. 7-12: Comparison of pars tensa responses with fixed nodes on each side of rotational axis (black line); and with 3 orthogonal springs on each side of rotational axis (blue line). The red point is the location where the displacement was measured.

7.4.4 Umbo, pars-tensa and footplate frequency responses

Fig. 7- 13 shows the displacement frequency responses of nodes selected on the umbo, in the posterior

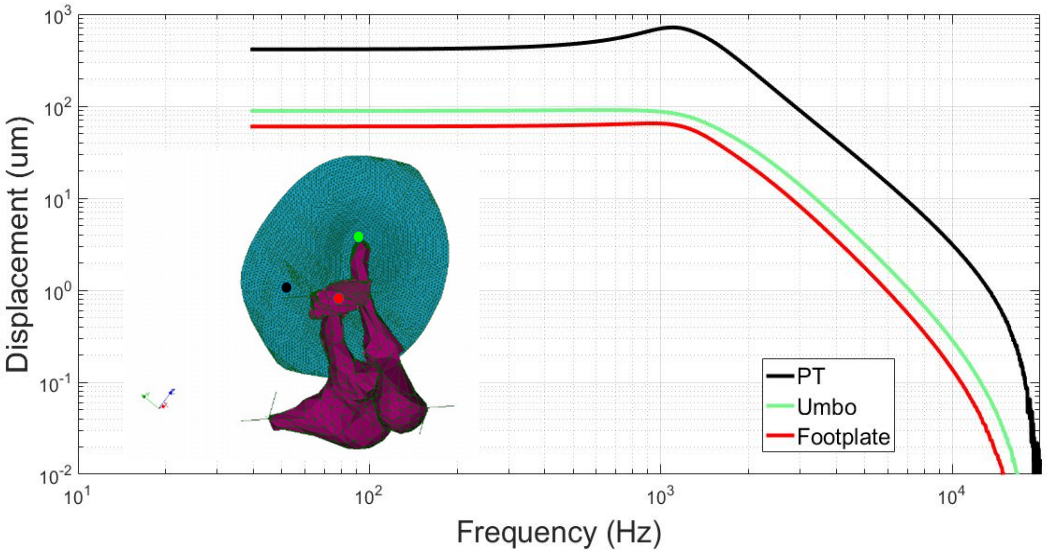

Fig. 7-13: Simulated displacements on the pars tensa (PT, black point), umbo (green point) and footplate (red point).

region of the PT, and on the footplate. The ratios among the curves are approximately constant up to about 400 Hz. A shallow resonance peak on the TM, at around 1200 Hz, has a magnitude of 200 μm/Pa (for the input pressure of 2 Pa). At the umbo, there is no apparent resonance peak; the displacement at the umbo is ~ 45 μm/Pa at low frequencies. At the footplate, there is a very shallow resonance peak at about 1.1 kHz, with a magnitude of displacement of around 30 μm/Pa. The magnitude ratios among the points, and the slopes of the corresponding curves, are again approximately constant between 2 and 10 kHz.

Fig. 7-14 shows a comparison of model responses at points in the PT posterior and anterior regions (at the level of the umbo) and at the umbo. The maximum displacement appears in the anterior region before 1 kHz. After 1 kHz, the displacement in the anterior region starts decreasing to a lower value than that in the posterior region. This indicates that the spatial vibration pattern changes with frequency above the resonance frequency.

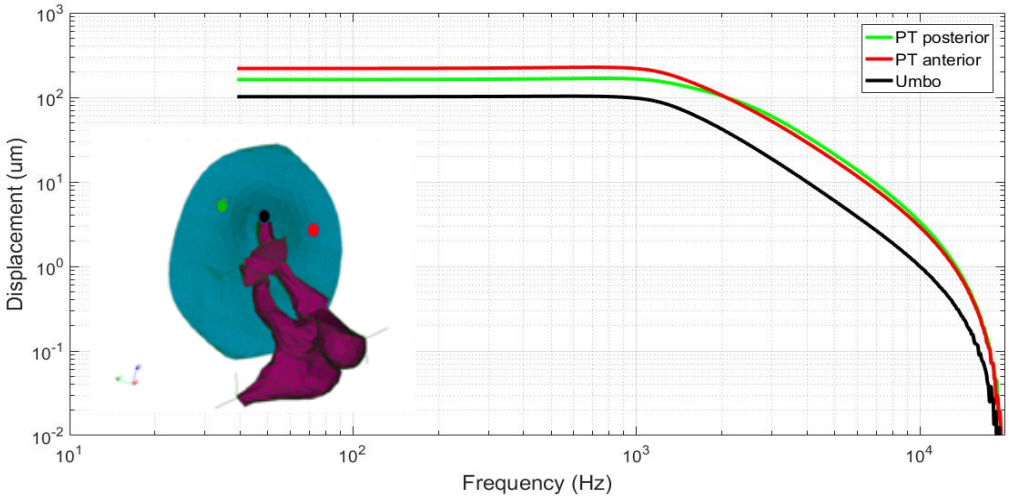

Fig. 7-14: Comparison of model responses in the PT posterior (green) and anterior (red) regions and at the umbo (black).

Fig. 7-15 shows a comparison of model responses at the umbo, at 1/3 of the way up the manubrium, at mid-manubrium, at 2/3 of the way up the manubrium, and at the level of the short process (the superior end of the manubrium). The magnitude increases toward the umbo, and the magnitude ratios among the points along the manubrium are constant up to ~ 2 kHz. The ratios of the magnitudes along the manubrium do not stay constant at higher frequencies, suggesting that the manubrium may be bending or that the rotational axis is shifting slightly.

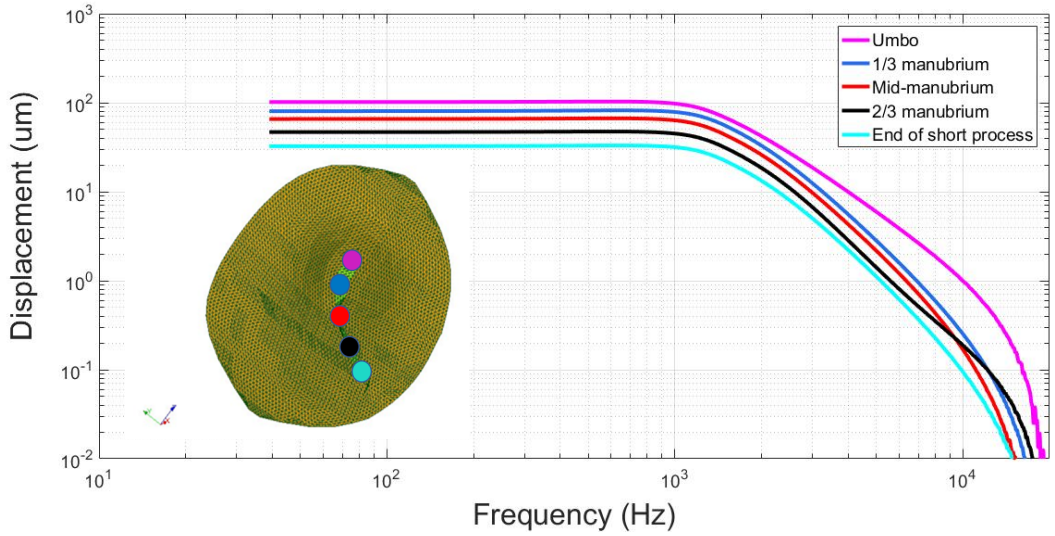

Fig. 7-15: Comparison of model responses at the umbo (purple), at 1/3 of the way up the manubrium (blue), at mid-manubrium (red), at 2/3 of the way up the manubrium (black) and at the level of the short process (cyan).

7.5 Sinusoidal pressure signals

We also studied the response of the middle-ear model to sinusoidal pressure stimuli with peak-to-peak magnitudes of ±2 Pa. The frequencies simulated were 500 Hz, 1 kHz and 2kHz, corresponding to the Doppler OCT experimental measurements made in human temporal bones in February 2016 (500 Hz) and in June 2017 (all three frequencies) at Dalhousie University. The results for the 500-Hz stimulus are compared with the displacements measured experimentally in February 2016 in the ear on which the model was based. The sinusoidal pressure stimulus is used as a verification of our frequency-response simulation results. In addition, this kind of stimulus allows the specification of a constant damping ratio with Rayleigh damping, by using different Rayleigh parameters for each frequency, instead of having the damping ratio change with frequency as discussed in Section 4.3.

The displacement amplitudes at five points along the manubrium are presented in Fig. 7-16. The magnitudes increase toward the umbo for all three frequencies. From Fig. 7-15, with the step responses,

we know that the magnitude ratios of those points are almost constant up to about 2 kHz. The displacements of the umbo seen here at 0.5, 1 and 2 kHz are in the same ratios as seen in Fig. 7-15. This pattern in the responses in consistent with the fact that in our model the malleus is assumed to rotate around a fixed axis of rotation. Therefore, the displacement along the manubrium is proportional to its distance from the axis of rotation. As discussed in Section 3.3.2, Koike et al. (2002) reported that the manubrium rotates as a rigid body around a fixed axis at frequencies up to about 2 kHz, beyond which the position of the rotational axis started to shift and to move out of phase. In the model here, however, we modelled very stiff springs on each side of the malleus and incus, to mimic a fixed anatomical rotation axis, so the ratios are independent of frequency.

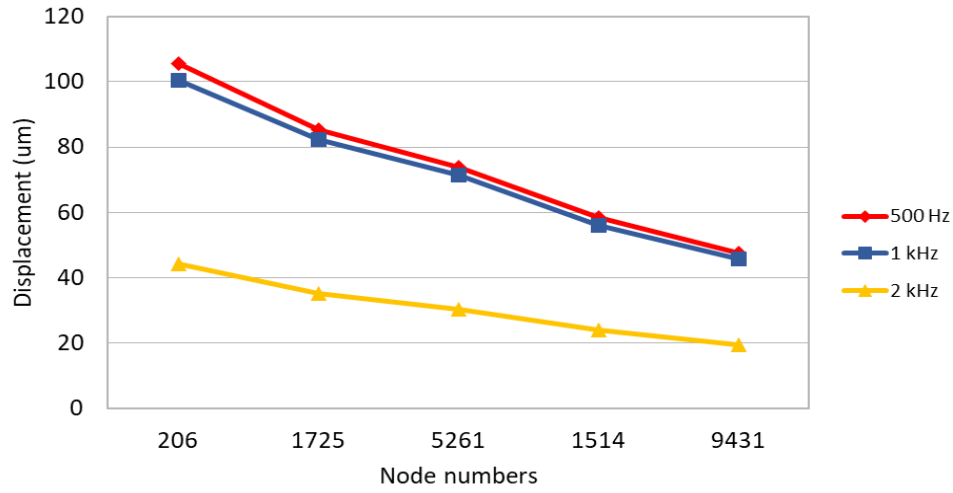

Fig. 7-16:Comparison of model responses at different frequencies: 500 Hz (red line), 1000 Hz (blue line) and 2000 Hz (yellow line). The 5 points composing each line are the displacements of nodes at the umbo (node number 206), at 1/3 of the way up manubrium (node number 1725), at mid-manubrium (node number 5261), at 2/3 of the way up manubrium (node number 1514) and at the short process (node number 9431).

Fig. 7-17 shows our model responses for the umbo and for two points on the PT at the level of the umbo (as in Fig. 7-14). The ratios of the PT amplitudes to the umbo amplitude are the same for both PT

points up to 2 kHz. As observed in the Doppler OCT measurements experimentally, at all three frequencies the point at the posterior location shows larger displacements than the one at the anterior location, and both displacements are larger than at the umbo.

As seen in Figs. 7-16 and 7-17, the displacements resulting from the 500-Hz and 1-kHz sinusoidal acoustical stimuli are very similar, with maximum differences of 2% at corresponding points. The displacements at 2 kHz, on the other hand, are much smaller than those at the lower frequencies. This discrepancy becomes smaller along the manubrium from the umbo to the short process, especially between 1 kHz and 2 kHz, but the ratios of the magnitudes are constant, which implies that the manubrium is not bending, at least at frequencies up to 2 kHz.

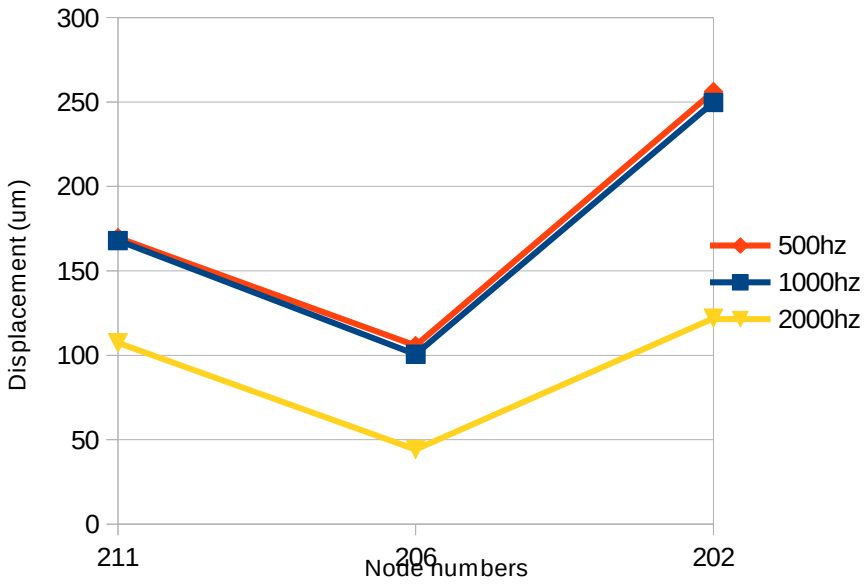

Fig. 7-17: Comparison of model responses at different frequencies: 500 Hz (red line), 1000 Hz (blue line) and 2000 Hz (yellow line). The three points composing each line are the displacements of nodes in the PT posterior region (node number 211), at the umbo (node number 206) and in the PT anterior region (node number 202).

7.6 Doppler optical coherence tomography measurements

Correlation of our model's response with the Doppler OCT measurements in the same middle ear is essential since one of the goals of our work is to avoid the effects of ear-to-ear variability. Fig. 7-18

shows the displacement pattern of the TM and manubrium in a Doppler OCT image. Both the simulation results and the experimental measurements show the maximal displacement appearing in the posterior region and a smaller maximum in the anterior region, with smaller displacements on the malleus, incus and stapes. Experimentally the cochlear promontory appears immobile. Our model's TM displacement at 500 Hz is similar to that of the actual ear, with the maximum displacements being approximately 24% larger than the simulation result. The 500-Hz displacement amplitude of our model umbo is approximately 10% smaller than the corresponding experimentally measured value. The experimental measurement did not capture the displacement of the footplate due to the limited OCT penetration depth, so it cannot be compared with the simulated displacement.

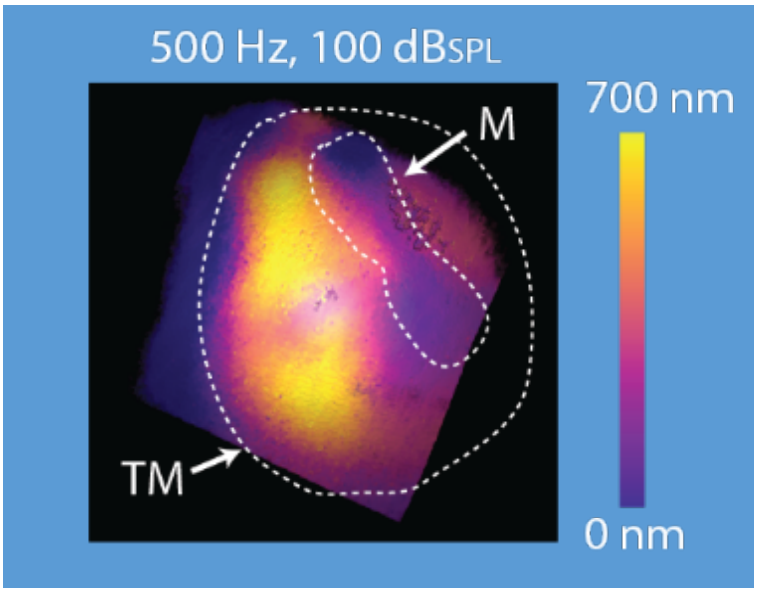

Fig. 7-18: Displacement pattern of TM and manubrium (M) in Doppler OCT image.

The maximal experimental TM measurement of De Greef et al. (2017) was reported to be 173 μm/Pa at 1 kHz. The Doppler OCT measurement as shown in Fig. 7-18 is the peak-to-peak displacement of the structure. The maximum displacement in the posterior region of the TM, as measured by OCT for a 500-Hz, 100-dB SPL sound stimulus, was 700 μm. The normalized zero-to-peak displacement is thus

175 μm/Pa, which is very similar to what was reported by De Greef et al. (2017). (The displacements at 500 Hz and 1 kHz are expected to be very similar, based on both experimental and simulation results.)

7.7 Comparison of 3-D model shapes

The TM shape matching between the microCT-based and OCT-based segmented models was performed in Fad (Funnell, 2018b) and subsequently reviewed in Unity 3D (Unity Technologies http://unity3D.com) to validate the comparison. Fig. 7-17 is a medial view of the shape registration between the microCT-based model and the OCT-based model. The general sizes are comparable between the models but the curvature of the TM segmented from the Doppler OCT data is relatively flat compared to the curvature from microCT.

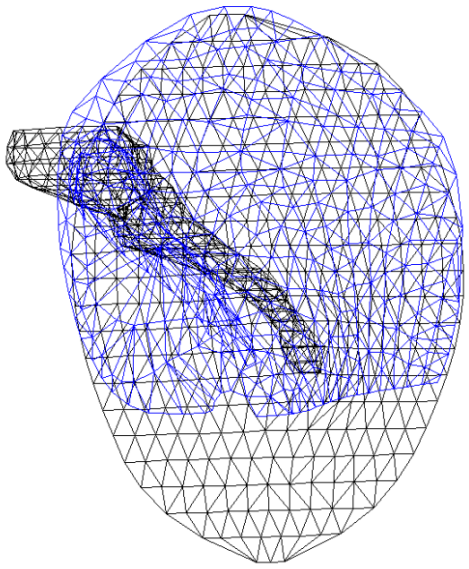

Fig. 7-19: Medial view of shape comparison between microCT-based model (black) and OCT-based model (blue).

This shape comparison was based on matching landmarks (e.g., edges of geometrical structures such as the umbo and manubrium) between images, and not on directly comparing the shapes voxel by voxel. The performance of this method depends on the reliability of detecting the matching image features,

which is challenging when the images are missing distinctive features. For example, in this study the Doppler OCT image only captured part of the TM, with three sides cropped off, which introduced uncertainties when registering the two models together. The new dataset acquired in June 2017 captured all of the TM, including the surrounding temporal bone, which can be used as the reference for the boundary of the TM. This should make it much easier in the future to register and compare the models derived from OCT and microCT.

Chapter 8
Conclusion

8.1 Introduction

In this chapter, we start with a brief summary in Section 8.2. In Section 8.3, we discuss our results. We propose future work in Section 8.4 and indicate the significance of this project in Section 8.5.

8.2 Summary

This work represents a study of the biomechanics of the human middle ear through FE modelling and result validation with experimental Doppler OCT measurements in the same ear. Relevant issues about the middle-ear anatomy, structure and available experimental data were introduced. Then an overview of FE modelling approaches was presented, followed by the imaging techniques (microCT and OCT) used in this thesis. The process of building the middle-ear model and the challenges in the model-building process were described. We created a FE model of the human middle ear that included the TM, the TMMC, the ossicular chain, and approximate boundary conditions. A linear model was used to simulate the elastic behaviour of the middle ear. The elastic properties of the model components were chosen according to *a priori* estimates. Damping and the cochlear load were also defined in the model. The static responses of the model calculated in two different solvers (SAP IV and Code_Aster) were analyzed. The results from the two solvers produced very similar results. We performed mesh-convergence and parameter-sensitivity analyses.

For comparison with experimental data, we simulated loading conditions similar to those of the Doppler OCT experiments performed by Dr. Adamson's group at Dalhousie University (500-Hz

harmonic sound pressure). We reported the simulated displacements as functions of frequency for points located at the umbo and on the TM and stapes to validate against the experimental data.

We found that our model displacements are in good agreement with the OCT experimental data in terms of the displacement pattern and of the maximal displacement, which appears in the posterior region of the TM. Similarities were also found between the model behaviours in our study and in other modelling studies, in terms of both the resonance frequencies and the maximum values of the umbo displacement. In previous work from our lab, Mikhael (2005) reported that the first resonance frequency appeared at 1100 Hz, similar to the result of our study. The model of Mikhael (2005) also shows a similarity with our model in the magnitude of displacement at the umbo: her value was reported to be 36.6 μm/Pa, compared to 36 μm/Pa in our study, even though the material properties used in her model were very different from the ones used in our model. In addition, the maximal displacements of our model matched what was reported by DeGreef et al. (2017), which was 102 to109 nm/Pa around 1 kHz. The first resonance peak was also reported to be near 1 kHz in their work.

8.3 Discussion

According to our sensitivity analysis, the Young's modulus and thickness of the PT have a very strong influence on the displacements of the TM and manubrium. This is expected and is similar to the findings of other studies, (e.g., Maftoon et al., 2015; De Greef et al., 2017). Hoffstetter et al. (2010) found that the TM's stiffness and thickness had very small effects on the middle-ear transfer function at low frequencies; the relationship of this to our findings and those of other groups should be explored.

In addition, our sensitivity analysis shows that the Young's modulus of the TMMC is another influential parameter in determining the behaviour of the system. Hoffstetter et al. (2010) found that excluding or including the TMMC will introduce a change in the middle-ear transfer function of more

than 25%. Some previous studies reported contradictory results, concluding that the effect of the TMMC is negligible. For example, Koike et al. (2002) performed a comparison of FE models with tight and loose TMMC and concluded that “the modification of the attachment between the malleus handle and the tympanic membrane did not greatly influence the vibration mode and displacement of the tympanic membrane”. De Greef et al. (2017) reported that variations in the TMMC loss factor and stiffness had a negligible influence. Their approach to modelling and varying the TMMC was different from ours and the results are therefore difficult to compare. This test is worth considering in future studies.

We also found that the influence of the ISJ on TM and manubrial displacements is small (less than 1%) in our sensitivity analysis, compared to the very large influence on the transfer function observed by Hoffstetter et al. (2010). In addtion, changing the Poisson ratio has a small effect (less than 1%) in our model. However, Maftoon et al. (2015) reported a fairly large change in displacements resulting from changing the Poisson ratio of the gerbil ISJ by 10%, which caused an increase of 20 nm/Pa (about 4%). They considered that the large effects of the Poisson ratio indicate that more sophisticated models of the joints would be beneficial. The small effect in our results may indicate an inappropriate range of material properties. Further analysis is needed to examine the discrepancy between our results and those of Maftoon et al.

We saw that the damping strongly affects the smoothness of the frequency responses at high frequencies, and boundary conditions substantially affect the resonance frequency and the magnitude of the displacement.

8.4 Future work

Future studies are recommended to further our understanding of human middle-ear mechanics and the application of OCT. First of all, the segmentation of the FE model here was mostly done manually or semi-automatically. This process was very time-consuming and it would be useful to investigate how to improve it by introducing reliable automatic image segmentation methods.

One limitation of the sensitivity study is that it involved the variation of just a single parameter at a time. In complex mechanical systems, the parameter influences can be coupled. Such coupled effects could not be detected using the current method. In the interpretation of the results, it is important to keep this methodological limitation in mind. It would also be useful to extend the sensitivity analysis to include stapes displacements and the middle-ear transfer function.

In addition, for simplicity, Rayleigh damping was used in our model. The Rayleigh damping approach has no basis in actual dissipative mechanisms. The Prony series is another popular representation of the damping in soft tissues (e.g., Motallebzadeh et al., 2013). It represents damping in separate frequency ranges to allow more control over the frequency dependence of the damping, which will be worth examining in future studies.

The present model includes a number of simplifications, and further refinements can be made by including the suspensory ligaments of the malleus and incus, the stapes footplate annular ligament and the fibrocartilaginous ring of the TM, the ossicular joints, etc. The thickness of the TM is important in determining the system vibration patterns; one should consider using the detailed thickness variations from the literature and potentially the thickness variations from OCT images. However, the in-vivo thickness from our OCT measurements was about three times thicker than the thickness in the microCT images. This can at least partially be attributed to artifacts introduced by the system. Since our

measurements were made, the in-vivo Doppler OCT system has been updated to improve the image quality, including a more realistic measurement of the thickness of the TM.

Although the computation time was not a problem for our linear models, it would be interesting to explore ways to decrease the computational cost, to enable the development of more complex models. We could speed up our computations by implementing parallel Code_Aster. We could also use graphical processing units (GPUs) for the FE solvers. For example, Taylor et al. (2009) reported a much faster processing rate for FE analysis using GPU execution compared to CPU execution.

Only one human middle ear was included in this study The rationale was to build confidence in our ability to model and explain the behaviour of the middle ear by comparing the model to experimental Doppler OCT measurements. The ultimate goal is to streamline this workflow into one that can efficiently produce a number of models created from individual human ears. In addition, more work is needed to clarify the response of the middle ear, especially the TM, to different frequencies of the acoustic stimulus.

8.5 Significance

To the best of our knowledge, this is the first time that the response of the human middle ear to sound has been validated against Doppler OCT measurement from the same ear. Similar work was done by Mikhael (2005), based on laser Doppler vibrometry, but the current approach of using a real-time Doppler OCT system, which can be used *in vivo*, promises applicability to the clinical examination.

This study also enhances our understanding of the issues involved in exploiting Doppler OCT images, including reslicing, denoising, and coordination transformation. It also showed the functionality of our tools for building 3-D biomechanical models, including Fie, Tr3 etc., as well as the validity of different

open-source FE solvers like Code_Aster. It has also provided experience with combining a FE model with *in vivo* Doppler OCT measurements, to be pursued in future work.

References

Aibara, R., Welsh, J. T., Puria, S., & Goode, R. L. (2001). Human middle-ear sound transfer function and cochlear input impedance. *Hear. Res.*, *152*(1–2), 100–109.

Bally, G. von. (1982). Otoscopic investigations by holographic interferometry: A fiber endoscopic approach using a pulsed ruby laser system. *Opt. Biomed. Sci.*, Springer Series in Optical Sciences (pp. 110–114). Springer, Berlin, Heidelberg. Retrieved from: https://link.springer.com/chapter/10.1007/978-3-540-39455-6_23

Bathe, K.-J. (2016). Finite Element Procedures, (2nd edition), 1065.

von Békésy, G. (1960). *Experiments in hearing*. McGraw-Hill New York. Retrieved from: http://asadl.org/books/01_03_11_experiments

Borg, E., & Zakrisson, J. E. (1975). The activity of the stapedius muscle in man during vocalization. *Acta Otolaryngol. (Stockh.)*, *79*(5–6), 325–333.

Carmel, P. W., & Starr, A. (1963). Acoustic and nonacoustic factors modifying middle-ear muscle activity in waking cats. *J. Neurophysiol.*, *26*, 598–616.

Cerrolaza, M., Shefelbine, S., & Garzón-Alvarado, D. (2017). *Numerical methods and advanced simulation in biomechanics and biological processes*. Academic Press.

Chang, E. W., Cheng, J. T., Röösli, C., Kobler, J. B., Rosowski, J. J., & Yun, S. H. (2013). Simultaneous 3D imaging of sound-induced motions of the tympanic membrane and middle ear ossicles. *Hear. Res.*, *304*, 49–56.

Cheng, J. T., Aarnisalo, A. A., Harrington, E., Hernandez-Montes, M. D. S., Furlong, C., Merchant, S. N., & Rosowski, J. J. (2010). Motion of the surface of the human tympanic membrane measured with stroboscopic holography. *Hear. Res.*, *263*(1–2), 66–77.

Choudhury, N., Song, G., Chen, F., Matthews, S., Tschinkel, T., Zheng, J., Jacques, S. L., et al. (2006). Low coherence interferometry of the cochlear partition. *Hear. Res.*, *220*(1–2), 1–9.

Choukir, S. (2017). Finite-element modelling of tympanic-membrane vibrations under quasi-static pressurization. Master's thesis, McGill University.

Courant, R. (1943). Variational methods for the solution of problems of equilibrium and vibrations. *Bull Amer Math Soc*., 49, 1-23.

Daniel, S. J., Funnell, W. R., Zeitouni, A. G., Schloss, M. D., & Rappaport, J. (2001). Clinical applications of a finite-element model of the human middle ear. *J. Otolaryngol.*, *30*(6), 340–346.

De Greef, D., Goyens, J., Pintelon, I., Bogers, J., Van Rompaey, V., Hamans, E., Van de Heyning, P., et al. (2016). On the connection between the tympanic membrane and the malleus. *Hear. Res.*, MEMRO 2015 – Basic Science meets Clinical Otology, *340*, 50–59.

De Greef, D., Pires, F., & Dirckx, J. J. J. (2017). Effects of model definitions and parameter values in finite element modeling of human middle ear mechanics. *Hear. Res.*, *344*, 195–206.

Decraemer, W. F., Dirckx, J. J. J., & Funnell, W. R. J. (2003). Three-dimensional modelling of the middle-ear ossicular chain using a commercial high-resolution X-ray CT scanner. *JARO – J. Assoc. Res. Otolaryngol.*, *4*(2), 250–263.

Decraemer, W. F., & Funnell, W. R. J. (2008). *Anatomical and mechanical properties of the tympanic membrane*. Pp. 51–84 in "Chronic otits media: Pathogenesis-oriented therapeutic management", B. Ars (ed.). Kugler, The Hague.

Decraemer, W. F., & Khanna, S. M. (1999). New insights into vibration of the middle ear. Pp 23–38 in "The Function and Mechanics of Normal, Diseased and Reconstructed Middle Ears", Rosowski J. J. & Merchant S. N. (eds.). Kugler, The Hague.

Decraemer, W. F., & Khanna, S. M. (2004). Measurement, visualization and quantitative analysis of complete three-dimensional kinematical data sets of human and cat middle ear. *Middle Ear Mech. Res. Otol.* (Vols. 1-0, pp. 3–10). World scientific. Retrieved from: https://www.worldscientific.com/doi/abs/10.1142/9789812703019_0001

Decraemer, W. F., Khanna, S. M., & Funnell, W. R. J. (1991). Malleus vibration mode changes with frequency. *Hear. Res. 54*(2): 305–318.

Decraemer, W. F., Khanna, S. M., & Funnell, W. R. J. (1999). Vibrations at a fine grid of points on the cat tympanic membrane measured with a heterodyne interferometer. *Int. Symp. Ind. Lasers Insp. Conf. Biomed. Laser Metrol. Appl.*, 1–4.

Decraemer, W. F., de La Rochefoucauld, O., Dong, W., Khanna, S. M., Dirckx, J. J. J., & Olson, E. S. (2007). Scala vestibuli pressure and three-dimensional stapes velocity measured in direct succession in gerbil. *J. Acoust. Soc. Am.*, *121*(5 Pt1), 2774–2791.

Decraemer, W. F., de La Rochefoucauld, O., Funnell, W. R. J., & Olson, E. S. (2014). Three-dimensional vibration of the malleus and incus in the living gerbil. *J. Assoc. Res. Otolaryngol. 15*(4), 483–510.

Decraemer, W. F., de La Rochefoucauld, O., & Olson, E. S. (2011). Measurement of the three-dimensional vibration motion of the ossicular chain in the living gerbil (Vol. 1403, pp. 528–533). Presented at the American institute of physics conference Series. Retrieved from: http://adsabs.harvard.edu/abs/2011AIPC.1403..528D

Dirckx, J. J. J., & Decraemer, W. F. (1989). Phase shift moire apparatus for automatic 3D surface measurement. *Rev. Sci. Instrum.*, *60*(12), 3698–3701.

Dirckx, J. J. J., & Decraemer, W. F. (1997). Optoelectronic moiré projector for real-time shape and deformation studies of the tympanic membrane. *J. Biomed. Opt.*, *2*(2), 176–186.

Dirckx, J. J. J., & Decraemer, W. F. (2001). Effect of middle-ear components on eardrum quasi-static deformation. *Hear. Res.157*, 124–137.

Djalilian, H. R., Ridgway, J., Tam, M., Sepehr, A., Chen, Z., & Wong, B. J. F. (2008). Imaging the human tympanic membrane using optical coherence tomography in vivo. *Otol. Neurotol.*, *29*(8), 1091–1094.

Djupesland, G. (1965). Electromyography of the tympanic muscles in man. *International Journal of Audiology 4*(1), 34–41.

Eiber, A., & Kauf, A. (1994). Bechnete verschiebungen der mittelohrknochen unter statischer belastung. *HNO*, *42*(12), 754–759.

Elkhouri, N., Liu, H., & Funnell, W. R. J. (2006). Low-frequency finite-element modeling of the gerbil middle ear. *J. Assoc. Res. Otolaryngol.*, *7*(4), 399–411.

Feeney, M. P., & Keefe, D. H. (1999). Acoustic reflex detection using wide-band acoustic reflectance, admittance, and power measurements. *J. Speech Lang. Hear. Res.*, *42*(5), 1029–1041.

Ferrazzini, M. (2003). *Virtual middle ear: a dynamic mathematical model based on the finite element method* (Doctoral Thesis). ETH Zurich. Retrieved from: https://www.research-collection.ethz.ch/handle/20.500.11850/147758

Ferreira, A., Gentil, F., & Tavares, J. M. R. S. (2012). Segmentation algorithms for ear image data towards biomechanical studies. *Comput. Methods Biomech. Biomed. Engin.*, *17*(8), 888–904.

Ferris, P., & Prendergast, P. J. (2000). Middle-ear dynamics before and after ossicular replacement. *J. Biomech.*, *33*(5), 581–590.

Foley, J. D. (1990). *Computer graphics : principles and practice*. Reading, Mass. : Addison-Wesley. Retrieved from: http://archive.org/details/computergraphics00fole

Fritze, W., Kreitlow, H., & Winter, D. (1979). On holographic-interferometric investigations of the membrana tympani (living man). *Hologr. Med. Biol.*, Springer series in optical sciences (pp. 206–211). Springer, Berlin, Heidelberg. Retrieved from: https://link.springer.com/chapter/10.1007/978-3-540-38961-3_28

Fumagalli, Z. (1949). *Morphological research on the sound-transmission apparatus*. Arch. Ital. Otol. Rinol. Laringol. 60, Suppl. 1, ix + 323 pp.

Funnell, W. R. J. (1983). On the undamped natural frequencies and mode shapes of a finite-element model of the cat eardrum. *J. Acoust. Soc. Am.*, *73*(5), 1657–1661.

Funnell, W. R. J. (1984a). On the choice of a cost function for the reconstruction of surfaces by triangulation between contours. *Comput. Struct.*, *18*(1), 23–26.

Funnell, W. R. J. (1984b). On the calculation of surface areas of objects reconstructed from serial sections. *J. Neurosci. Methods*, *11*(3), 205–210.

Funnell, W. R. J. (1996). Low-frequency coupling between eardrum and manubrium in a finite-element model. *J. Acoust. Soc. Am.*, *99*(5), 3036–3043.

Funnell, W. R. J. (2016). Fod: http://audilab.bme.mcgill.ca/~funnell/AudiLab/sw/fod.html

Funnell, W. R. J. (2018a). Fie. Retrieved from: http://audilab.bme.mcgill.ca/~funnell/AudiLab/sw/fie.html

Funnell, W. R. J. (2018b). Fad: http://audilab.bme.mcgill.ca/~funnell/AudiLab/sw/fad.html

Funnell, W. R. J., & Decraemer, W. F. (1996). On the incorporation of moiré shape measurements in finite-element models of the cat eardrum. *J. Acoust. Soc. Am.*, *100*(2), 925–932.

Funnell, W. R. J., Decraemer, W. F., & Khanna, S. M. (1987). On the damped frequency response of a finite-element model of the cat eardrum. *J. Acoust. Soc. Am.*, *81*(6), 1851–1859.

Funnell, W. R. J., Heng Siah, T., McKee, M. D., Daniel, S. J., & Decraemer, W. F. (2005). On the coupling between the incus and the stapes in the cat. *J. Assoc. Res. Otolaryngol.*, *6*(1), 9–18.

Funnell, W. R. J., Khanna, S. M., & Decraemer, W. F. (1992). On the degree of rigidity of the manubrium in a finite-element model of the cat eardrum. *J. Acoust. Soc. Am.*, *91*(4), 2082–2090.

Funnell, W. R. J., & Laszlo, C. A. (1978). Modeling of the cat eardrum as a thin shell using the finite-element method. *J. Acoust. Soc. Am.*, *63*(5), 1461–1467.

Funnell, W. R. J., & Laszlo, C. A. (1982). A critical review of experimental observations on ear-drum structure and function. *J. Oto-Rhino-Laryngol. Its Relat. Spec.*, *44*(4), 181–205.

Funnell, W. R. J., Maftoon, N., & Decraemer, W. F. (2013). Modeling of middle ear mechanics. In S. Puria, R. R. Fay, & A. N. Popper (Eds.), *Middle Ear* (pp. 171–210). Springer New York. Retrieved from: http://link.springer.com/10.1007/978-1-4614-6591-1_7

Funnell, W. R. J., Maftoon, N., & Decraemer, W. F. (2012). Mechanics and modelling for the middle ear. Retrieved from: http://audilab.bme.mcgill.ca/~funnell/AudiLab/mammie/mammie.pdf

Gan, R. Z., Feng, B., & Sun, Q. (2004). Three-dimensional finite element modeling of human ear for sound transmission. *Ann. Biomed. Eng.*, *32*(6), 847–859.

Gan, R. Z., Reeves, B. P., & Wang, X. (2007). Modeling of sound transmission from ear canal to cochlea. *Ann. Biomed. Eng.*, *35*(12), 2180–2195.

Gan, R. Z., Sun, Q., Feng, B., & Wood, M. W. (2006). Acoustic-structural coupled finite element analysis for sound transmission in human ear--pressure distributions. *Med. Eng. Phys.*, *28*(5), 395–404.

Gan, R. Z., Yang, F., Zhang, X., & Nakmali, D. (2011). Mechanical properties of stapedial annular ligament. *Med. Eng. Phys.*, *33*(3), 330–339.

Gao, S. S., Xia, A., Yuan, T., Raphael, P. D., Shelton, R. L., Applegate, B. E., & Oghalai, J. S. (2011). Quantitative imaging of cochlear soft tissues in wild-type and hearing-impaired transgenic mice by spectral domain optical coherence tomography. *Opt. Express*, *19*(16), 15415–15428.

Gariepy, B. (2011). Finite-element modelling of the newborn ear canal and middle ear. Master's thesis, McGill University.

Ghosh, S. S. (1996). On the effects of incudostapedial joint flexibility in a finite-element model of the cat middle ear. Master's thesis, McGill University.

Graham, M. D., Reams, C., & Perkins, R. (1978). Human tympanic membrane-malleus attachment. Preliminary study. *Ann. Otol. Rhinol. Laryngol.*, *87*(3 Pt 1), 426–431.

Guinan, J. J., & Peake, W. T. (1967). Middle-ear characteristics of anesthetized cats. *J. Acoust. Soc. Am.*, *41*(5), 1237–1261.

Gyo, K., Aritomo, H., & Goode, R. L. (1987). Measurement of the ossicular vibration ratio in human temporal bones by use of a video measuring system. *Acta Otolaryngol. (Stockh.)*, *103*(1–2), 87–95.

Hagr, A., Funnell, W. R. J., Zeitouni, A., & Rappaport, J. (2004). High-resolution x-ray CT scanning of the human stapes footplate. *J. Otolaryngol. 33*(4), 217–221.

Heermann, R., Hauger, C., Issing, P. R., & Lenarz, T. (2002). Application of optical coherence tomography (OCT) in middle ear surgery. *Laryngorhinootologie.*, *81*(6), 400–405.

Helmholtz, H., & Ellis, A. J. (1895). *On the sensations of tone as a physiological basis for the theory of music*. London, New York : Longmans, Green, and Co. Retrieved from: http://archive.org/details/onsensationsofto00helmrich

Hoffstetter, M., Schardt, F., Lenarz, T., Wacker, S., & Wintermantel, E. (2010). Parameter study on a finite element model of the middle ear. *Biomed. Tech. (Berl)*, *55*(1), 19–26.

Holzapfel, G. A.(2000). Nonlinear Solid Mechanics : A Continuum Approach for Engineering. Wiley, Chichester, UK.

Hong, S. S., & Freeman, D. M. (2006). Doppler optical coherence microscopy for studies of cochlear mechanics. *J. Biomed. Opt.*, *11*(5), 054014.

Hrennikoff, A. (1941). *Solution of problems of elasticity by the frame-work method*. ASME J. Appl. Mech. *8*, A619-A715.

Hudde, H., & Weistenhofer, C. (1997). A three-dimensional circuit model of the middle ear. *Acustica*, *83*, 535–49.

Irvine, D. R. (1976). Effects of reflex middle-ear muscle contractions on cochlear responses to bone-conducted sound. *Audiol. Off. Organ Int. Soc. Audiol.*, *15*(5), 433–444.

Just, T., Lankenau, E., Hüttmann, G., & Pau, H. W. (2009). Optical coherence tomography in middle ear surgery. *HNO*, *57*(5), 421–427.

Karmody, C. S., Northrop, C. C., & Levine, S. R. (2009). The incudostapedial articulation: New concepts. *Otol. Neurotol.*, *30*(7), 990–997.

Kawase, T., Shibata, S., Katori, Y., Ohtsuka, A., Murakami, G., & Fujimiya, M. (2012). Elastic fiber-mediated enthesis in the human middle ear. *J. Anat.*, *221*(4), 331–340.

Kelly, D. J., Prendergast, P. J., & Blayney, A. W. (2003). The effect of prosthesis design on vibration of the reconstructed ossicular chain: a comparative finite element analysis of four prostheses. *Otol. Neurotol. Off. Publ. Am. Otol. Soc. Am. Neurotol. Soc. Eur. Acad. Otol. Neurotol.*, *24*(1), 11–19.

Khanna, S. M., & Tonndorf, J. (1975). Tympanic membrane shape determined by moiré topography. *J. Acoust. Soc. Am.*, *57*(S1), S72–S72.

Kirikae, I. (1960). *The Structure and Function of the Middle Ear.* University of Tokyo Press.

Kishi, S. (2016). Impact of swept source optical coherence tomography on ophthalmology. *Taiwan J. Ophthalmol.*, *6*(2), 58–68.

Koike, T., Wada, H., & Kobayashi, T. (2002). Modeling of the human middle ear using the finite-element method. *J. Acoust. Soc. Am.*, *111*(3), 1306–1317.

Kojo, Y. (1954). The morphological studies of the human tympanic membrane. *Nippon Jibiinkoka Gakkai Kaiho*, *57*(2), 115-122.

Kuypers, L. C., Decraemer, W. F., & Dirckx, J. J. J. (2006). Thickness distribution of fresh and preserved human eardrums Measured with confocal microscopy. *Otol. Neurotol.*, *27*(2), 256–264.

Kuypers, L., Decraemer, W., Dirckx, J., & Timmermans, J. (2005). A procedure to determine the correct thickness of an object with confocal microscopy in case of refractive index mismatch. *J. Microsc.*, *218*(1), 68–78.

Kwacz, M., Rymuza, Z., Michałowski, M., & Wysocki, J. (2015). Elastic properties of the annular ligament of the human stapes—AFM measurement. *JARO J. Assoc. Res. Otolaryngol.*, *16*(4), 433–446.

Ladak, H. M., & Funnell, W. R. (1996). Finite-element modeling of the normal and surgically repaired cat middle ear. *J. Acoust. Soc. Am.*, *100*(2 Pt 1), 933–944.

Lee, C.-F., Chen, P.-R., Lee, W.-J., Chen, J.-H., & Liu, T.-C. (2006). Computer aided three-dimensional reconstruction and modeling of middle ear biomechanics by high-resolution computed tomography and finite element analysis. *Biomed. Eng. - Appl. Basis Commun.*, *18*(5), 214–221.

Lim, D. J. (1970). Human tympanic membrane. An ultrastructural observation. *Acta Otolaryngol. (Stockh.)*, *70*(3), 176–186.

Liu, Y., Li, S., & Sun, X. (2009). Numerical analysis of ossicular chain lesion of human ear. *Acta Mech. Sin. Xuebao*, *25*(2), 241–247.

Lobato, L., Paul, S., & Catarina, S. (2017). Influence of different boundary conditions at the tympanic annulus on finite element models of the human middle ear. Mechanics of Hearing. Retrieved from DOI: 10.13140/RG.2.2.29247.71842

Lobregt, S., & Viergever, M. A. (1995). A discrete dynamic contour model. *IEEE Trans. Med. Imaging*, *14*(1), 12–24.

Løkberg, O. J., Høgmoen, K., & Gundersen, T. (1979). Use of ESPI to measure the vibration of the human eardrum in vivo and other biological movements. *Hologr. Med. Biol.*, Springer Series in Optical Sciences (pp. 212–217). Springer, Berlin, Heidelberg. Retrieved from: https://link.springer.com/chapter/10.1007/978-3-540-38961-3_29

Løkberg, O. J., Høgmoen, K., & Gundersen, T. (1980). Vibration measurement of the human tympanic membrane-in vivo. *Acta Otolaryngol. (Stockh.)*, *89*(1–2), 37–42.

Lutman, M. E., & Martin, A. M. (1979). Development of an electroacoustic analogue model of the middle ear and acoustic reflex. *J. Sound Vib.*, *64*(1), 133–157.

MacDougall, D., Farrell, J., Brown, J., Bance, M., & Adamson, R. (2016). Long-range, wide-field swept-source optical coherence tomography with GPU accelerated digital lock-in Doppler vibrography for real-time, in vivo middle ear diagnostics. *Biomed. Opt. Express*, *7*(11), 4621–4635.

MacDougall, D., Landry, T., Bance, M., Brown, J., & Adamson, R. (2015a). Optical coherence tomography for clinical otology. *Can. Acoust.*, *43*(3). Retrieved from: https://jcaa.caa-aca.ca/index.php/jcaa/article/view/2790

MacDougall, D., Rainsbury, J., Brown, J., Bance, M., & Adamson, R. (2015b). Optical coherence tomography system requirements for clinical diagnostic middle ear imaging. *J. Biomed. Opt.*, *20*(5), 56008.

Maeta, M. (1991). Effects of the perforation of the tympanic membrane on its vibration-with special reference to an experimental study by holographic interferometry. *Nihon Jibiinkoka Gakkai Kaiho*, *94*(2), 231–240.

Maftoon, N. (2014). Experimental and modelling study of gerbil middle ear. Ph.D. thesis, McGill University.

Maftoon, N., Funnell, W. R. J., Daniel, S. J., & Decraemer, W. F. (2014). Effect of opening middle-ear cavity on vibrations of gerbil tympanic membrane. *J. Assoc. Res. Otolaryngol.*, *15*(3), 319–334.

Maftoon, N., Funnell, W. R. J., Daniel, S. J., & Decraemer, W. F. (2015). Finite-element modelling of the response of the gerbil middle ear to sound. *J. Assoc. Res. Otolaryngol.*, *16*(5), 547–567.

Magnoni, A. (1938). Migration of epithelium of tympanic membrane. *Valsalva*, (14), 234–240.

Marquet, J. (1981). The incudo-malleal joint. *The Journal of Laryngology & Otology, 95*(6): 543–565.

Merchant, S. N., Ravicz, M. E., & Rosowski, J. J. (1996). Acoustic input impedance of the stapes and cochlea in human temporal bones. *Hear. Res.*, *97*(1–2), 30–45.

Mikhael, C. S., (2005). Finite-element modelling of the human middle ear. Master's thesis, McGill University.

Mikhael, C. S., Funnell, W. R. J., & Bance, M. (2004). Middle-ear finite-element modelling with realistic geometry and a priori material-property estimates. *Proc. 28th Annual Conf. Can. Med. Biol. Eng. Soc.*, Québec City, 126-129.

Møller, A. R. (1974). The Acoustic Middle Ear Muscle Reflex. *Audit. Syst.*, Handbook of Sensory Physiology (pp. 519–548). Springer, Berlin, Heidelberg. Retrieved from: https://link.springer.com/chapter/10.1007/978-3-642-65829-7_16

Motallebzadeh, H., Gariepy, B., Maftoon, N., Funnell, W. R. J., & Daniel, S. J. (2013). Finite-element modelling of the newborn ear canal and middle ear. *Proc. Meet. Acoust.*, *19*(1), 030101.

Motallebzadeh, H., Maftoon, N., Pitaro, J., Funnell, W. R. J., & Daniel, S. J. (2017a). Fluid-structure finite-element modelling and clinical measurement of the wideband acoustic input admittance of the newborn ear canal and middle Ear. *J. Assoc. Res. Otolaryngol. JARO*, *18*(5), 671–686.

Motallebzadeh, H., Maftoon, N., Pitaro, J., Funnell, W. R. J., & Daniel, S. J. (2017b). Finite-element modelling of the acoustic input admittance of the newborn ear canal and middle ear. *J. Assoc. Res. Otolaryngol.*, *18*(1), 25–48.

Okano, K. (1990). Influence of liquid volume in the middle ear on tympanic membrane vibration (experimental study by holographic interferometry). *Nihon Jibiinkoka Gakkai Kaiho*, *93*(11), 1847–1855.

Pang, X. D., & Guinan, J. J. (1997). Effects of stapedius-muscle contractions on the masking of auditory-nerve responses. *J. Acoust. Soc. Am.*, *102*(6), 3576–3586.

Pang, X. D., & Peake, W. T. (1986). *How Do Contractions of the Stapedius Muscle Alter the Acoustic Properties of the Ear?* Peripheral audirory mechanisms. 36–43, Springer, Berlin.

Pitris, C., Saunders, K. T., Fujimoto, J. G., & Brezinski, M. E. (2001). High-resolution imaging of the middle ear with optical coherence tomography: a feasibility study. *Arch. Otolaryngol. Head Neck Surg.*, *127*(6), 637–642.

Prendergast, P. J., Ferris, P., Rice, H. J., & Blayney, A. W. (1999). Vibro-acoustic modelling of the outer and middle ear using the finite-element method. *Audiol. Neurootol.*, *4*(3–4), 185–191.

Qi, L. (2008). Non-linear finite-element modelling of newborn ear canal and middle ear. Ph.D. thesis, McGill University.

Rabbitt, R. D., & Holmes, M. H. (1986). A fibrous dynamic continuum model of the tympanic membrane. *J. Acoust. Soc. Am.*, *80*(6), 1716–1728.

Ravicz, M. E., Cooper, N. P., & Rosowski, J. J. (2008). Gerbil middle-ear sound transmission from 100 Hz to 60 kHz. *J. Acoust. Soc. Am.*, *124*(1), 363–380.

de la Rochefoucauld, O., Decraemer, W. F., Khanna, S. M., & Olson, E. S. (2008). Simultaneous measurements of ossicular velocity and intracochlear pressure leading to the cochlear input impedance in gerbil. *J. Assoc. Res. Otolaryngol. JARO*, *9*(2), 161–177.

Rosowski, J. J. (2010). External and middle ear function. *Oxf. Handb. Audit. Sci. Ear*. Retrieved from: http://www.oxfordhandbooks.com/view/10.1093/oxfordhb/9780199233397.001.0001/oxfordhb-9780199233397-e-03

Rosowski, J. J., Cheng, J. T., Ravicz, M. E., Hulli, N., Hernandez-Montes, M., Harrington, E., & Furlong, C. (2009). Computer-assisted time-averaged holograms of the motion of the surface of the mammalian tympanic membrane with sound stimuli of 0.4-25 kHz. *Hear. Res.*, *253*(1–2), 83–96.

Saunders, J. C., & Johnstone, B. M. (1972). A comparative analysis of middle-ear function in non-mammalian vertebrates. *Acta Otolaryngol. (Stockh.)*, *73*(2–6), 353–361.

Schneider, P. J. (1990). Graphics gems -an algorithm for automatically fitting digitized curves. In A. S. Glassner (Ed.), (pp. 612–626). San Diego, CA, USA: Academic Press Professional, Inc. Retrieved from: http://dl.acm.org/citation.cfm?id=90767.90941

Sepehr, A., Djalilian, H. R., Chang, J. E., Chen, Z., & Wong, B. J. F. (2008). Optical coherence tomography of the cochlea in the porcine model. *The laryngoscope*, *118*(8), 1449–1451.

Standring, S. & Gray, H. (2008). Gray's Anatomy – 40th Edition. Retrieved from: https://www.elsevier.com/books/grays-anatomy/standring/978-0-443-06684-9

Strang, G., & Fix, G. J. (1973). *An Analysis of the Finite Element Method*. (G. Forsythe, Ed.). Englewood Cliffs, N.J: Prentice-Hall.

Subhash, H. M., Nguyen-Huynh, A., Wang, R. K., Jacques, S. L., Choudhury, N., & Nuttall, A. L. (2012). Feasibility of spectral-domain phase-sensitive optical coherence tomography for middle ear vibrometry. *J. Biomed. Opt.*, *17*(6), 060505.

Suehiro, M. (1990). Effects of an increase or decrease in the middle ear pressure on tympanic membrane vibrations (experimental study by holographic interferometry). *Nihon Jibiinkoka Gakkai Kaiho*, *93*(3), 398–406.

Sun, Q., Gan, R. Z., Chang, K.-H., & Dormer, K. J. (2002). Computer-integrated finite element modeling of human middle ear. *Biomech. Model. Mechanobiol.*, *1*(2), 109–122.

Taylor, Z. A., Comas, O., Cheng, M., Passenger, J., Hawkes, D. J., Atkinson, D., & Ourselin, S. (2009). On modelling of anisotropic viscoelasticity for soft tissue simulation: numerical solution and GPU execution. *Med. Image Anal.*, *13*(2), 234–244.

Tonndorf, J., & Khanna, S. M. (1972). Tympanic-membrane vibrations in human cadaver ears studied by time-averaged holography. *J. Acoust. Soc. Am.*, *52*(4), 1221–1233.

Van der Jeught, S., Dirckx, J. J. J., Aerts, J. R. M., Bradu, A., Podoleanu, A. G., & Buytaert, J. A. N. (2013). Full-field thickness distribution of human tympanic membrane obtained with optical coherence tomography. *JARO J. Assoc. Res. Otolaryngol.*, *14*(4), 483–494.

Velten, K. (2009). Mathematical modeling and simulation: Introduction for scientists and engineers. *Wiley–VCH,* Weinheim.

Volandri, G., Di Puccio, F., Forte, P., & Carmignani, C. (2011). Biomechanics of the tympanic membrane. *J. Biomech.*, *44*(7), 1219–1236.

Wada, H., & Kobayashi, T. (1990). Dynamical behavior of middle ear: theoretical study corresponding to measurement results obtained by a newly developed measuring apparatus. *J. Acoust. Soc. Am.*, *87*(1), 237–245.

Wada, H., Metoki, T., & Kobayashi, T. (1992). Analysis of dynamic behavior of human middle ear using a finite-element method. *J. Acoust. Soc. Am.*, *92*(6), 3157–3168.

van Wijhe, R., Funnell, W. R., Henson, O., & Henson, M. (2000). Development of a finite-element model of the middle ear of the moustached bat. Master's thesis, McGill University.

Williams, K. R., & Lesser, T. H. J. (1989). A finite element analysis of the natural frequencies of vibration of the human tympanic membrane. Part II. *Proc. First Int. Conf. Interfaces Med. Mech.* (pp. 282–293). Springer, Dordrecht. Retrieved from: https://link.springer.com/chapter/10.1007/978-94-011-7477-0_29

Williams, K. R., & Lesser, T. H. J. (1990). A finite element analysis of the natural frequencies of vibration of the human tympanic membrane. Part I. *Br. J. Audiol.*, *24*(5), 319–327.

Wong, B. J., de Boer, J. F., Park, B. H., Chen, Z., & Nelson, J. S. (2000). Optical coherence tomography of the rat cochlea. *J. Biomed. Opt.*, *5*(4), 367–370.

Yost, W. A., & Nielsen, D. W. (1977). *Fundamentals of Hearing: An Introduction*. Holt, Rinehart and Winston.

Zienkiewicz, O. C., & Taylor, R. L. (1991). *The finite element method* (5th ed.). Oxford Butterworth-Heinemann. Retrieved from: https://trove.nla.gov.au/work/4904564

Zwislocki, J. (1957). Some impedance measurements on normal and pathological ears. *J. Acoust. Soc. Am.*, *29*(12), 1312–1317.